ABSTRACT

Title of dissertation: THE KINETIC STRUCTURE OF COLLISIONLESS SLOW SHOCKS AND RECONNECTION EXHAUSTS

Yi-Hsin Liu
Doctor of Philosophy, 2011

Dissertation directed by: Professor James F. Drake
Department of Physics

A 2-D Riemann problem is designed to study the development and dynamics of the slow shocks that are thought to form at the boundaries of reconnection exhausts. Simulations are carried out for various ratios of normal magnetic field to the transverse upstream magnetic field (*i.e.*, propagation angle with respect to the upstream magnetic field). When the angle is sufficiently oblique, the simulations reveal a large firehose-sense ($P_\parallel > P_\perp$) temperature anisotropy in the downstream region, accompanied by a transition from a coplanar slow shock to a non-coplanar rotational mode. In the downstream region the firehose stability parameter $\varepsilon = 1 - \mu_0(P_\parallel - P_\perp)/B^2$ tends to plateau at 0.25. This balance arises from the competition between counterstreaming ions, which drives ε down, and the scattering due to ion inertial scale waves, which are driven unstable by the downstream rotational wave. At very oblique propagating angles, 2-D turbulence also develops in the downstream region.

An explanation for the critical value 0.25 is proposed by examining anisotropic fluid theories, in particular the Anisotropic Derivative Nonlinear-Schrödinger-Burgers

equations, with an intuitive model of the energy closure for the downstream counter-streaming ions. The anisotropy value of 0.25 is significant because it is closely related to the degeneracy point of the slow and intermediate modes, and corresponds to the lower bound of the transition point in a compound slow shock(SS)/rotational discontinuity(RD) wave. This work implies that it is a pair of compound SS/RD waves that bounds the reconnection outflow, instead of a pair of switch-off slow shocks as in Petschek's model.

THE KINETIC STRUCTURE OF COLLISIONLESS SLOW SHOCKS AND RECONNECTION EXHAUSTS

by

Yi-Hsin Liu

Dissertation submitted to the Faculty of the Graduate School of the
University of Maryland, College Park in partial fulfillment
of the requirements for the degree of
Doctor of Philosophy
2011

Advisory Committee:
Professor James F. Drake, Chair/Advisor
Dr. Michael M. Swisdak
Professor Adil B. Hassam
Professor William D. Dorland
Professor Christopher S. Reynolds, Dean's Representative

Dedication

To my Dad, my Mom and my Wife.

Acknowledgments

First and foremost I thank my advisor, Professor Jim Drake for bringing me here into his group at University of Maryland and giving me an invaluable opportunity to work on challenging and interesting topics over the past six years. It is a pleasure and unforgettable experience to work with and learn from such an extraordinary individual. I also thank my co-advisor, Dr. Marc Swisdak, who always made himself available for help and advice; there has never been an occasion when I've knocked on his door and he hasn't given me time. I thank Dr. Cheng-Chin Wu, Prof. Yi Lin and Prof. Steve Spangler for helpful discussions that were relevant to this thesis work. Thanks are also due to Professor Roald Sagdeev, Professor Adil Hassam, Professor Bill Dorland and Professor Christ Reynolds for agreeing to serve on my thesis committee and for sparing their valuable time reviewing the manuscript.

My colleagues at the plasma theory group have enriched my graduate life in many ways and deserve a special mention, Dr. Parvez Guzdar, Prof. Mike Shay, Prof. Paul Cassak, Dr. Haihong Che, Kevin Schoefller, Ray Fermo, Tak Chu Li and Joe Dalin. I thank my past advisors when I was in Taiwan, Prof. Ming-Feng Shih, Prof. Jiun-Huei Wu, Prof. Shin-Nan Yang and Prof. Chi Yuan. I especially would like to express my appreciation to Prof. Chi Yuan for being my role model as a respectful scholar. I also thank Prof. Chien-Chang Yen, Dr. Chao-Chin Yang and Dr. Bau-Ching Hsieh for leading me into the field of computational physics. Finally, I deeply thank Prof. Lin-Ni Hau for encouraging me to pursue plasma physics for

my doctoral degree.

I also wish to acknowledge help and support from some of the staff members. Jane Hessing and Nancy Boone are highly appreciated, as is the computer hardware support from Edward Condon, the LaTex template from Dorothea Brosius.

I owe my deepest thanks to my family - to my my wife, Min-Chun Liao, my mother, Ching-Kuai Peng, my father, Ping-Chang Liu, and my sisters, Chen-Yu Liu and Chia-Hui Liu who have always supported me. Words cannot express the gratitude I owe them.

Table of Contents

List of Figures

List of Abbreviations

θ_{BN}	propagation angle
β	plasma beta (the ratio of thermal pressure to magnetic pressure)
ε	$1 - \mu_0(P_\parallel - P_\perp)/B^2$, firehose stability parameter
ACR	Anomalous Cosmic Ray
ADNLSB	Anisotropic Derivative Nonlinear Schrödinger Burgers Equation
AU	Astronomical Unit (distance between the Sun and Earth)
CME	coronal mass ejection
EMIIC	Electromagnetic Ion Ion Cyclotron instability
E	entropy mode
F	fast mode
FR	fast rarefaction
FS	fast shock
I	intermediate mode
IMF	interplanetary magnetic field
IS	intermediate shock
KAW	kinetic Alfvén wave
MHD	magnetohydrodynamic
nT	nano-Tesla
PIC	Particle-in-Cell simulation
RD	rotational discontinuity
R_e	Earth's radius
SL	slow mode
SLAMs	short large-amplitude magnetic structures
SR	slow rarefaction
SS	slow shock
SSS	switch-off slow shock
SS/IS	compound slow shock/intermediate shock wave
SS/RD	compound slow shock/rotational discontinuity wave

Chapter 1

Introduction

1.1 Magnetic Reconnection: General

The complex interaction of charged particles and electromagnetic fields drives a nontrivial phenomenon called magnetic reconnection. The simple cartoon in Fig. 1.1 shows the basic idea. Magnetic reconnection takes place in a thin current sheet sandwiched by oppositely directed ambient magnetic fields. Whenever the ambient magnetic fields (blue) approach each other, they reconnect inside a narrow dissipation region (the intense current region). The reconnected fields (red) act like rubber bands that release their tension force to drive high-speed hot outflows away from the reconnection site, since magnetic fields and the plasma are tied together (the frozen-in phenomenon) outside the central dissipation region. Once the reconnected hot plasma shoots out, the pressure in the central region drops, and therefore sucks in more plasma and magnetic flux from the upper and lower ambient regions to reconnect. This process is self-driven.

Magnetic reconnection is the primary mechanism for converting magnetic energy into kinetic and thermal energy in collisionless plasma. It also acts as a major transport mechanism in collisionless plasmas. In addition, by coupling small- and large-scale physics — electron-scale kinetic processes break the frozen-in condition tying the field lines to the plasma, while the overall energy release reshapes the global

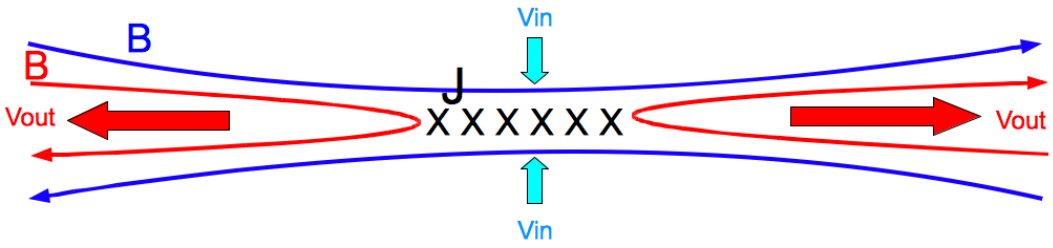

Figure 1.1: A cartoon of reconnection

environment — reconnection provides an excellent example of coupling across disparate spatial scales. Since 99% of visible matter in the universe is in the plasma state [37], magnetic reconnection is ubiquitous. It occurs in a wide variety of environments ranging from sawtooth crashes in fusion experiments [35, 49, 122, 58], geo-magnetic storms [2, 55, 90], solar flares [91, 63, 64], and the solar dynamo to various astrophysical phenomena such as Gamma Ray Bursts [76], pulsar winds [18, 73, 87] and astrophysical jets [75, 6]. We point out its active roles in the following cosmic plasma systems.

The most well established examples of astrophysical reconnection are found, as predicted by Dungy (1953, 1958) [30, 31], at the terrestrial magnetotail and magnetopause when southward interplanetary magnetic field (IMF) from the Sun smashes into Earth's magnetosphere. In Fig. 1.2 the solar wind comes from the left. The reconnection sites are marked by the symbol $\otimes$, one on the dayside and one on the night side about 20 R_e away from the Earth. Once the southward IMF encounters the Earth's northward dipole field, reconnection takes place at the magnetopause, and then the reconnected field lines are dragged by the solar wind over the poles and

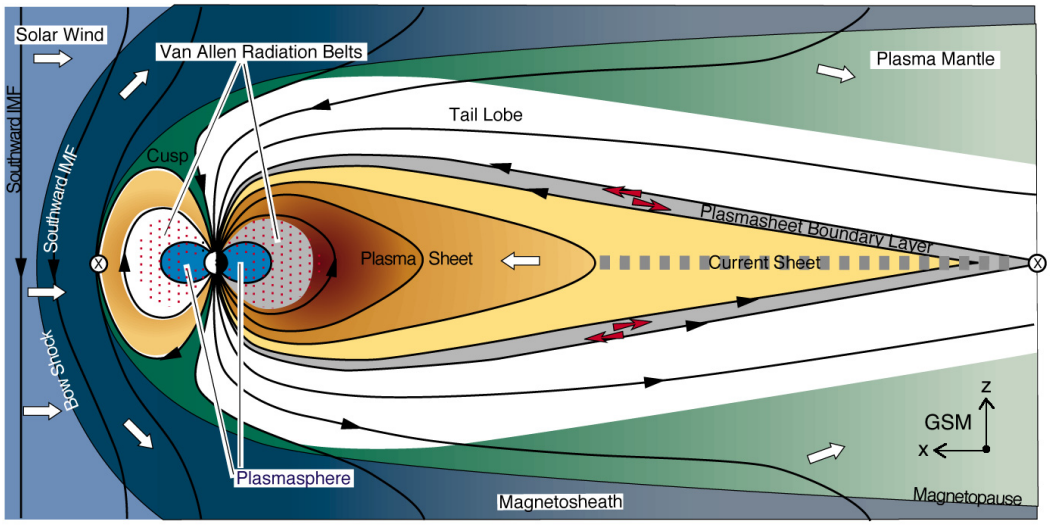

Figure 1.2: A cartoon of reconnections at Earth's magnetopause and magnetotail. Reconnection locations are denoted by the symbol $\otimes$. The distance from Earth to the tail reconnection site is around $20R_e$. (image from *http://journalinformationalmedicine.org/cr1.htm*)

stretch out on the night side of the Earth, where magnetotail reconnection then occurs. Tail reconnection is thought to trigger magnetic substorms ([2] and references therein) and also the formation of polar aurorae when reconnected plasma traces the magnetic field lines (the red arrows) back to the north and south poles of the Earth and interacts with the atmosphere. In between the Sun and Earth, gigantic reconnection current sheets in the turbulent solar wind are also observed [89, 36]. On the Sun, coronal mass ejections (CMEs) in large solar flares are driven by the topological change caused by reconnection [3, 63, 91]. Similar mechanisms apply to stellar flares and coronas of astrophysical accretion disks [25, 111].

Recently, reconnection was suggested to take place in the "sectored" field region between the termination shock of the solar wind and the heliopause, about 100

AU away from the Sun [26, 82]. If the rotational axis and magnetic dipole axis of the Sun were aligned, a heliospheric current sheet would form in the Sun's equatorial plane between the spiral-shaped magnetic fields in the northern and southern hemispheres [84]. However, these two axes are not aligned in reality, and therefore the current sheet flaps in the latitudinal (vertical) direction, creating a sectored region near the equator where the heliospheric field periodically reverses sign. As the sectored current sheet approaches the heliopause, the sectors narrow and trigger magnetic reconnection. In Fig. 1.3 Opher et al. (2011) [82] show a high resolution global magnetohydrodynamic (MHD) simulation performed to study the interaction between the interstellar medium (on the left) and the solar wind. The total strength of the magnetic field is color-coded and the flow streamlines are shown in black arrowed curves. The simulation shows that the heliosheath in between the heliopause and the termination shock is filled with a "sectored" field. The current sheets that separate the "sectored" field appear as vertical black striped structures which can be more clearly seen close to the right side (upstream) of the termination shock. Downstream of the termination shock, the striped structure is too fine scale to be resolved and so magnetic field dissipation occurs at the grid scale. As a result, the strength of the magnetic field around the downstream "sectored" region is weak (denoted by blue-black color). In order to better understand kinetic effects inside this region, the small red box displays the occurrence of reconnection and the formation of magnetic islands between reconnection sites in a Particle-in-Cell (PIC) simulation with parameters based on the global MHD run. A redder color represents a higher strength of magnetic field. This study aims to explain the source

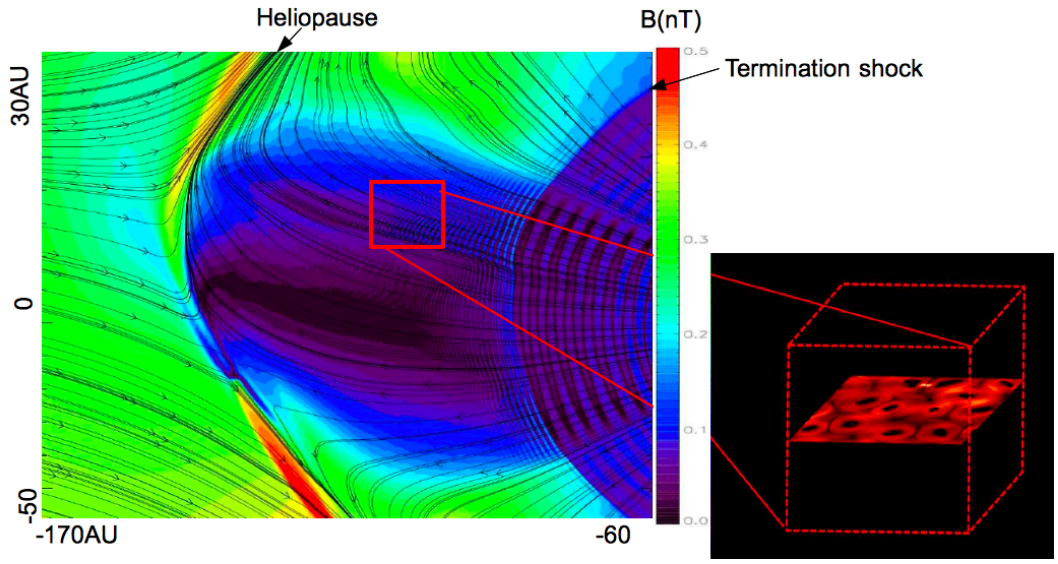

Figure 1.3: The magnetic islands formed by multiple reconnection sites in the sector fields between the Sun's termination shock and heliopause. The left panel is from a global MHD simulation, and the color represents the strength of the total magnetic field. The right panel is from a PIC simulation, and the redder color represents a larger magnetic field. (Adapted with permission from Ref. [Opher et al., 2011] ©2011 by the American Astronomical Society).

of anomalous cosmic ray (ACRs) and energetic electrons generated during reconnection and posits that they are accelerated by a first-order Fermi mechanism inside contracting magnetic islands [27, 26]. A similar "sectored" field could also form in pulsar winds driven by spinning neutron stars [18, 73, 87].

Magnetic reconnection also potentially plays an important dynamic role in the astrophysical jets from spinning black holes and the surrounding accretion disks [6, 75]. In Fig. 1.4 we show the results of a fully general relativistic MHD simulation by Beckwith et al. (2008) [6]. The left panel shows the initial state of a spinning black hole located at $(0, 0)$ with a vertical rotational axis, and the cross section of

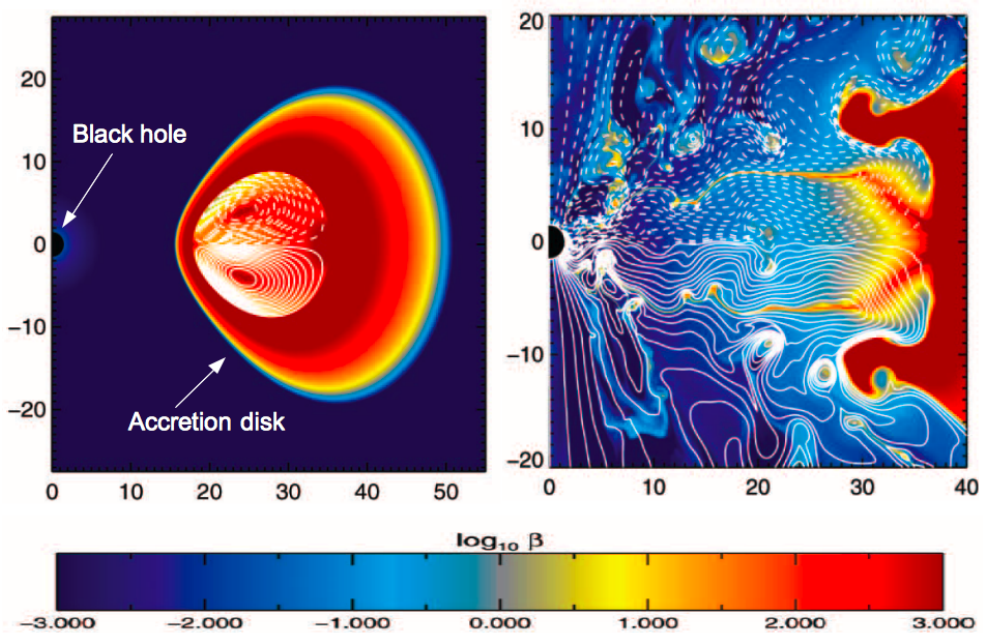

Figure 1.4: The formation of the accretion disk and jets of a spinning black hole under the influence of magnetic reconnection. The spatial unit is normalized to the black hole mass and the speed of light. The color represents plasma β. (Adapted with permission from Ref. [Beckwith et al., 2008]. ©2008 by the American Astronomical Society)

a toroidal accretion disk with seeded magnetic fields. The plasma β (the ratio of thermal pressure to magnetic pressure) is color coded and magnetic field lines are white contours where solid and dashed curves represent opposite parity. In the right panel, the magnetic field has been amplified by the magnetorotational instability and is carried by the inflowing plasma into the black hole. Once the magnetic field has been attached to the event horizon of the spinning black hole, jets are rapidly launched upward and downward from the black hole. The jets are marked by the strong vertical magnetic field (dark blue), and the jet formation mechanism presented here is a combination of models from Blandford & Znajek (1977) [11] and Blandford & Payne (1982) [10]. We notice the turbulent nature in the interface between the jet field and the accretion disk. Many magnetic islands are formed, which provides direct evidence that magnetic reconnection has occurred. Magnetic reconnection plays a role in changing the global topology of the magnetic field and hindering the formation of highly aligned jets [6]. Therefore, the reconnection rate must be considered as a critical dynamic time scale in constraining theoretical models.

1.2 Magnetic Reconnection: Theory

We write down the resistive-MHD equations here, Eqs. (1.1) to (1.7). All the theories presented throughout the rest of this thesis are sourced from these equations and its anisotropic extension. Ideal MHD uses the same equations, but neglects the resistivity in Ohm's law, Eq. (1.6).

Continuity equation:

$$\frac{\partial \rho}{\partial t} + \nabla \cdot (\rho \mathbf{V}) = 0 \tag{1.1}$$

Momentum equation:

$$\rho \frac{d\mathbf{V}}{dt} = \mathbf{J} \times \mathbf{B} - \nabla P \tag{1.2}$$

Energy equation:

$$\frac{\partial}{\partial t}\left[\frac{\rho V^2}{2} + \frac{B^2}{2\mu_0} + \frac{3}{2}P\right] + \nabla \cdot \left[\left(\frac{\rho V^2}{2} + \frac{5}{2}P\right)\mathbf{V} + \frac{\mathbf{E} \times \mathbf{B}}{\mu_0} + \mathbf{Q}\right] = 0 \tag{1.3}$$

Faraday's law:

$$\frac{\partial \mathbf{B}}{\partial t} = -\nabla \times \mathbf{E} \tag{1.4}$$

Ampére's law:

$$\nabla \times \mathbf{B} = \mu_0 \mathbf{J} \tag{1.5}$$

Ohm's law:

$$\mathbf{E} = -\mathbf{V} \times \mathbf{B} + \eta_r \mathbf{J} \tag{1.6}$$

The absence of magnetic monopoles:

$$\nabla \cdot \mathbf{B} = 0 \tag{1.7}$$

P, ρ, $\mathbf{V}$, $\mathbf{B}$, $\mathbf{E}$, $\mathbf{J}$, $\mathbf{Q}$ and η_r are the plasma pressure, mass density, velocity of the bulk flow, magnetic field, electric field, current density, heat flux, and the magnetic resistivity (assumed constant). Note that $\mathbf{J} \times \mathbf{B} = -\nabla(B^2/2\mu_0) + (\mathbf{B} \cdot \nabla)\mathbf{B}/\mu_0$. Hence the $\mathbf{J} \times \mathbf{B}$ force in the momentum equation (Eq. (1.2)) is usually expressed as the sum of a magnetic pressure gradient force and a magnetic tension force.

From Eq. (1.2), (1.4), (1.5), (1.6) and (1.7) under the assumptions of incompressibility ($\nabla \cdot \mathbf{V} = 0$) and 2-D ($\partial_y = 0$), we can write the simpler reduced-MHD equations, which are ideally compact for the purpose of explaining the basic reconnection model.

$$\frac{\partial}{\partial t}\nabla^2\phi + \mathbf{V}\cdot\nabla\nabla^2\phi = \frac{\mathbf{B}}{\mu_0\rho}\cdot\nabla\nabla^2\psi \tag{1.8}$$

$$\frac{\partial}{\partial t}\psi + \mathbf{V}\cdot\nabla\psi = \frac{\eta_r}{\mu_0}\nabla^2\psi \tag{1.9}$$

$$\mathbf{V} = \hat{\mathbf{y}}\times\nabla\phi, \qquad \mathbf{B} = \hat{\mathbf{y}}\times\nabla\psi + B_y\hat{\mathbf{y}}. \tag{1.10}$$

Here ϕ is the in-plane (x-z plane) stream function and ψ is the in-plane magnetic flux. Eq. (1.8) comes from the momentum equation with the right hand side being the $\mathbf{J}\times\mathbf{B}$ force. Eq. (1.9) comes from Faraday's law and Ohm's law with the right hand side being the resistive term. Eqs. (1.10) follow directly from the incompressibility limit and $\nabla\cdot\mathbf{B} = 0$. We keep the resistivity term since it is essential for breaking the frozen-in condition inside the dissipation region, and therefore the occurrence of reconnection. Note that $\partial\psi/\partial t = E_y$ is a spatially uniform constant in stationary 2-D solutions (according to Faraday's law), while $\partial\nabla^2\phi/\partial t = 0$.

1.2.1 Sweet-Parker Model

Sweet (1958) [106] and Parker (1957) [83] offered the first theory as to how reconnection occurs. In Fig. 1.5, we show a cartoon of the Sweet-Parker model. The dissipation region (the hatched box) has dimensions $L \times w$ where L is the system size in the z-direction and w is the width in the x-direction. Based on the symmetry

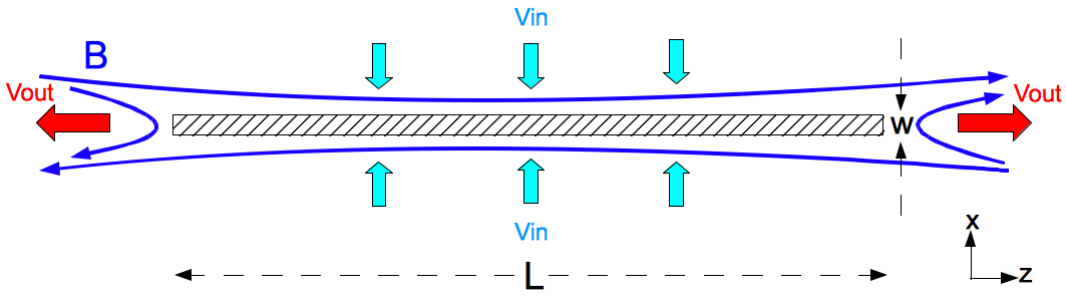

Figure 1.5: The Sweet-Parker model of reconnection.

of this 2-D model, a scaling analysis gives us $\partial_x \sim 1/w$, $\partial_z \sim 1/L$ and Eq. (1.10) becomes,

$$\mathbf{V}_u = V_{\text{in}}\hat{\mathbf{x}} \sim \frac{\Delta\phi}{L}\hat{\mathbf{x}}, \qquad \mathbf{V}_d = V_{\text{out}}\hat{\mathbf{z}} \sim \frac{\Delta\phi}{w}\hat{\mathbf{z}} \tag{1.11}$$

$$\mathbf{B}_u = B_{z,u}\hat{\mathbf{z}} \sim \frac{\Delta\psi}{w}\hat{\mathbf{z}}, \qquad \mathbf{B}_d = B_{x,d}\hat{\mathbf{x}} \sim \frac{\Delta\psi}{L}\hat{\mathbf{x}} \tag{1.12}$$

where the subscripts "u" and "d" denote upstream and downstream respectively. These also give us the relations,

$$\frac{V_{\text{in}}}{V_{\text{out}}} = \frac{B_{x,d}}{B_{z,u}} = \frac{w}{L} \tag{1.13}$$

Since we are looking for a steady state solution, from Eq. (1.8) $\mathbf{V}\cdot\nabla\nabla^2\phi = \mathbf{B}/(\mu_0\rho)\cdot\nabla\nabla^2\psi$, and hence the plasma convection term and the $\mathbf{J}\times\mathbf{B}$ force are balanced. With the relations Eq. (1.11) and (1.12), we obtain

$$V_{\text{out}} \sim \frac{B_{z,u}}{\sqrt{\mu_0\rho}} \equiv C_{Az} \tag{1.14}$$

$$V_{\text{in}} \sim \frac{B_{x,d}}{\sqrt{\mu_0\rho}} \tag{1.15}$$

From Eq. (1.9) $E_y \sim \mathbf{V}\cdot\nabla\psi$ outside the dissipation region, $E_y \sim (\eta_r/\mu_0)\nabla^2\psi$ inside the dissipation region. We equate them in the boundary of the dissipation

region, $\mathbf{V} \cdot \nabla \psi \sim (\eta_r/\mu_0)\nabla^2 \psi$, since E_y is spatially uniform in a stationary solution. Therefore the convection of magnetic flux and the dissipation of magnetic flux are balanced. With (1.13) and (1.14), we obtain the reconnection rate,

$$\frac{V_{\text{in}}}{C_{Az}} \sim \sqrt{\frac{\eta_r}{\mu_0 C_{Az} L}} \tag{1.16}$$

Note that the reconnection rate is defined as V_{in}/C_{Az}, which is also equal to $V_{\text{in}}/V_{\text{out}} = w/L$, the aspect ratio of the dissipation region. In this model, the energy of the reconnecting magnetic fields is dissipated by the magnetic resistivity and convected to Alfvénic flow. The biggest problem of this model is the predicted reconnection rate. A large system size (L) and small resistivity (η_r) will make the reconnection rate, Eq. (1.16), extremely small. Using values observed in solar flares in the formula yields predicts time scales of reconnection energy release of months, which contradicts the observed time scale of minutes.

1.2.2 Petschek Model- the Role of Slow Shocks

Following the publication of the MHD reconnection scenario of Sweet and Parker [106, 83], Petschek [88] noted that a pair of back-to-back slow shocks bounding the reconnection outflow could significantly raise the efficiency of the process by acting as a transition between the inflowing and reconnected outflowing plasma.

Petschek's primary insight is that waves from the singular dissipation region tend to propagate out in the x-direction, therefore changing the morphology of reconnection into an open outflow fan as shown in Fig. 1.6. First, we derive the properties of the external configuration (outside of the hatched box) where the

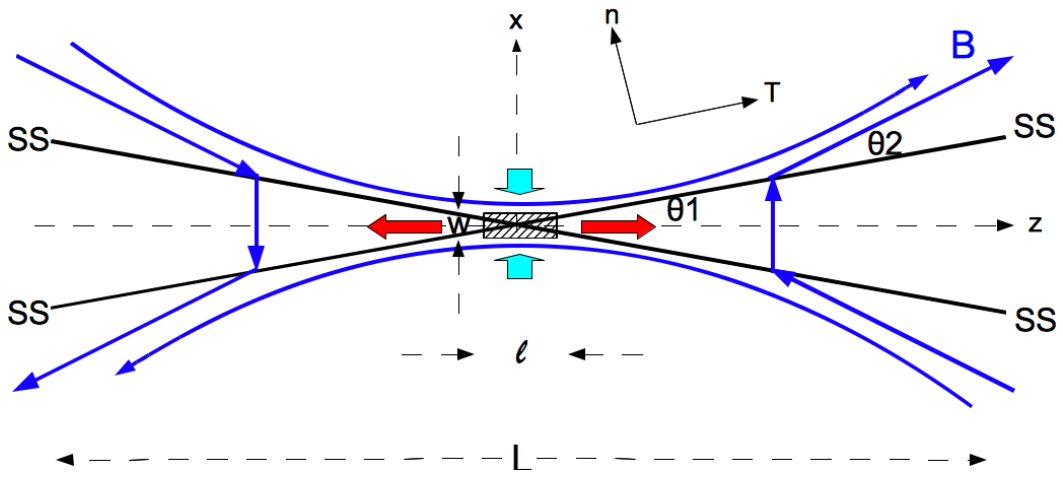

Figure 1.6: The Petschek model of reconnection.

dissipation of the magnetic field is negligible. We jump to the shock frame, denoted by the solid black line at the upper-right quadrant, with "n" and "T" being the normal and tangential direction respectively. From Eq. (1.10),

$$V_t = \partial_n \phi, \qquad V_n = -\partial_T \phi \tag{1.17}$$

$$B_t = \partial_n \psi, \qquad B_n = -\partial_T \psi \tag{1.18}$$

In the stationary shock frame, this is essentially a 1-D problem along the normal direction since the upstream and downstream are assumed to be uniform, and therefore $\partial_T(\mathbf{V} \text{ or } \mathbf{B})=0$. From Eq. (1.8), $\mathbf{V} \cdot \nabla\nabla^2\phi = \mathbf{B}/(\mu_0\rho) \cdot \nabla\nabla^2\psi$, and therefore the plasma convection term and the $\mathbf{J} \times \mathbf{B}$ force are again balanced.

$$V_n \partial_n^3 \phi = \frac{B_n}{\mu_0 \rho} \partial_n^3 \psi \tag{1.19}$$

Integrating over n twice, using Eqs. (1.17), (1.18) and the fact that V_n and B_n are

constant, we obtain a jump relation,

$$V_n[V_t]_u^d = \frac{B_n}{\mu_0\rho}[B_t]_u^d \tag{1.20}$$

where $[Q]_u^d \equiv Q_{\rm down} - Q_{\rm up}$. From Eq. (1.9) $E_y + \mathbf{V}\cdot\nabla\psi = 0$ (note that we do not need to consider the resistivity in this outer region), we use the constancy of E_y, V_n and B_n to get another relation,

$$V_n[B_t]_u^d = B_n[V_t]_u^d \tag{1.21}$$

From Eq. (1.20) and (1.21), we obtain the inflow speed in the shock frame,

$$V_n = \frac{B_n}{\sqrt{\mu_0\rho}} \tag{1.22}$$

In order to get a standing shock wave, the wave propagation speed needs to equal the velocity of the inflowing plasma. Based on this velocity constraint and the overall magnetic field configuration downstream, the only possible MHD shock wave is a switch-off slow shock (SSS). A SSS is the fastest and strongest slow shock, and has propagation speed equal to Eq. (1.22) (see Sec. 1.4.1).

In the $\theta_1 \ll 1$ limit, $\mathbf{B}_d \simeq B_n\hat{\mathbf{n}}$ and $\mathbf{V}_u \simeq V_n\hat{\mathbf{n}}$, then Eq. (1.21) becomes $V_nB_{t,u} \simeq B_nV_{t,d}$. Combined with Eq. (1.22), we obtain the tangential plasma speed in the downstream region,

$$V_{t,d} \simeq \frac{B_{t,u}}{\sqrt{\mu_0\rho}} \tag{1.23}$$

Therefore the slow shock directly converts the tangential magnetic field into plasma bulk flow velocity and, unlike the Sweet-Parker configuration, the conversion is not limited to slow dissipation by small η_r. In addition, in the $\theta_1 \ll 1$ and $\theta_2 \ll 1$ limit, $\theta_1 \simeq w/l$, and $\theta_2 \simeq B_n/B_{t,u} \sim B_{x,d}/B_{z,u} = w/l$. Therefore $\theta_1 \sim \theta_2$.

The flow speeds Eq. (1.23) and (1.22) are very similar to those inner solutions Eq. (1.14) and Eq. (1.15), and so one can smoothly match this external standing shock solution to the interior dissipation region to obtain a possible maximum reconnection rate (see Petschek (1964) for details) ,

$$\frac{V_{\rm in}}{C_{Az}} \sim \left(\ln\frac{L}{l}\right)^{-1} \sim \left(\ln\frac{L}{\eta_r}\right)^{-1} \tag{1.24}$$

The logarithmic dependence on (η_r/L) largely eliminate the reduction of the reconnection rate for small η_r and large L (which is the case for most astrophysical systems of interest). Regardless of the matching details, the reconnection rate will naturally be much higher since the dissipation region is significantly shortened in the Petschek configuration ($l \ll L$).

However, Biskamp (1986) [9] tested the Petschek solution by conducting reconnection simulations with the resistive-MHD model and a uniform resistivity. He found that reconnections sites collapse into elongated Sweet-Parker current sheets, instead of developing Petschek configurations. This calls into question the claim that Petschek's model is a valid stationary solution. The Petschek picture can be realized if the resistivity is allowed to vary with position, and in particular increase in regions of stronger current [94, 110, 96]. This locally enhanced anomalous resistivity could be generated by micro-scale instabilities [44, 29, 15], but conclusive proof of its existence has, to date, not been presented.

There is strong numerical evidence, however, that two-fluid effects, arising from the mass difference between ions and electrons in the reconnection dissipation region can open the reconnection outflow jet. This effect can be incorporated by

adding the Hall term ($\mathbf{J} \times \mathbf{B}/ne$) into Ohm's law (Eq. (1.6)). The resulting equation describes the dynamics of dispersive whistler waves that rotate the out-of-plane current into the outflow direction, and therefore open the reconnection nozzle into a Petscheck-like configuration [74, 92]. The GEM challenge [8] compared reconnection simulations performed with resistive-MHD, Hall-MHD, hybrid and Particle-in-Cell models. Only reconnection in the latter three models (all of which include two-fluid effects) spontaneously developed into Petschek-like configurations with a localized current sheet and, therefore, a fast reconnection rate. This finding supports the importance of two-fluid effects. By balancing the convection of magnetic flux with the Hall term (instead of the resistive term as in Sweet-Parker analysis) in a generalized Ohm's law, $\mathbf{V} \times \mathbf{B} \sim \mathbf{J} \times \mathbf{B}/ne$, then $V_{\rm in} \sim J_y/ne$. Using Eq. (1.15), (1.5) and (1.13) we obtain $w \sim \sqrt{m_i/\mu_0 ne^2} \equiv d_i$. The current sheet width w is determined to be the ion-inertial scale, with a nested smaller electron-inertial scale region where the frozen-in condition is broken. A fast reconnection rate $\sim \mathcal{O}(0.1)$ is observed in simulations to be insensitive to η_r and L [101, 102, 13].

No matter how complicated the real physics in the inner region however, Petschek's work showed that for fast reconnection to occur the outer, ideal MHD-dominated region must connect to the reconnection outflow via a pair of standing switch-off slow shocks.

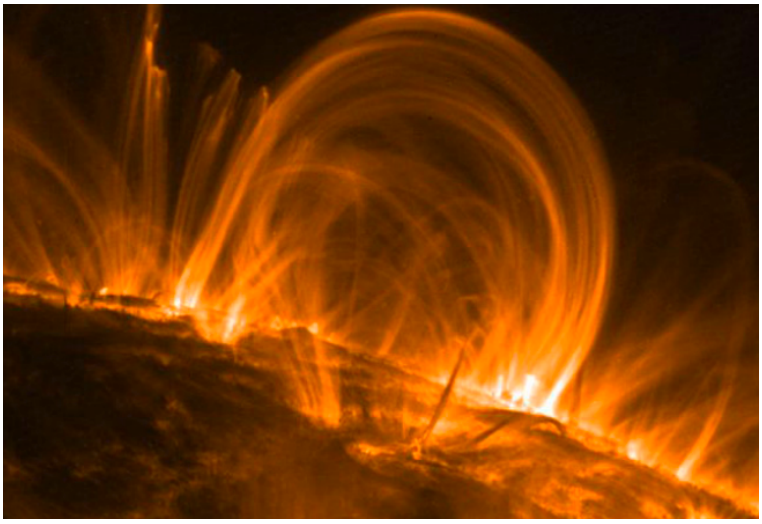

Figure 1.7: A soft X-ray image of solar corona loops on November 6, 1999. The major loop spans around $60R_e$, and are of the same type as the soft X-ray loops shown in Fig. 1.8. Courtesy of TRACE, a satellite mission of NASA.

.

1.3 The Structure of the Magnetic Reconnection Exhaust

In this section we show some examples of the kinetic structure of reconnection exhausts observed in space and in simulations, and discuss unsolved issues.

1.3.1 Solar Flare Heating by Slow Shocks

One of the important reasons for trying to understand the exhaust structure of reconnection is to study its potential heating ability. Ion heating by these Petschek-reconnection-associated slow shocks is one of the mechanisms that has been proposed for solar flares [109, 70] and the solar wind.

In Fig. 1.7, we show a soft X-ray image of solar corona loops. There is a long standing "Coronal Heating Problem", which asks why the temperature of the

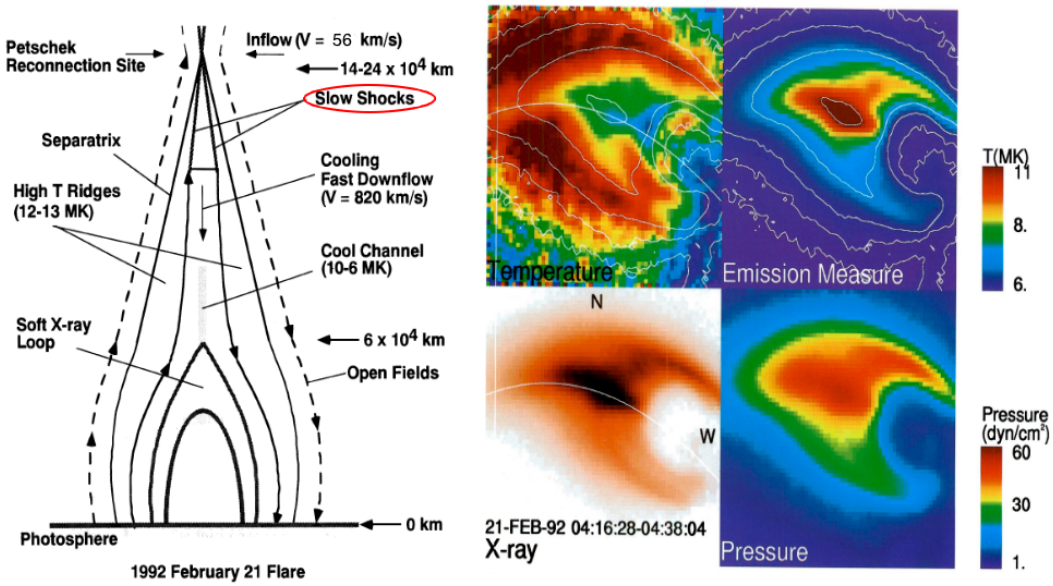

Figure 1.8: An observation of a solar flare exhibits heating by reconnection-associated slow shocks. Data from *Yohkoh* satellite on February 21, 1992. (Adapted with permission from Ref. [Tsuneta, 1996]. ©1996 by the American Astronomical Society)

corona is a thousand times hotter than the photosphere ($\sim 6000K$). As a possible solution, Parker (1983, 1988) [85, 86] suggested that the energy release from many nano-flares (which are triggered by reconnection), is adequate to heat the corona to several million degrees.

Another possible mechanism for producing a hot corona is the heating by slow shocks [109, 69]. In Fig. 1.8 Tsuneta (1996) [109] shows a large flare event that occurred on February 21, 1992. The left panel is a 2-D cartoon of solar flares where the arrowed curves represent magnetic fields, and the reconnection takes place at the top X-point where the slow shocks meet. The upper magnetic loop (not shown) becomes a coronal mass ejection (CME), and the post-flare corona loop is

snapping downward toward the photosphere. The corresponding observational data is shown on the right. The temperature along the separatrix has reached 10 million degrees, while intense X-ray emission extends along the reconnection nozzle to the top of the lower corona loop anchored on the photosphere. The emission measure measures the density of electrons. Since the observed X-rays are mainly emitted by the bremsstrahlung process associated with electrons, the high electron density region coincides with the intense X-ray region. The plasma pressure is high between the pair of separatrices. Tseuneta suggested that these high temperature ridges are heated by the standing slow shocks, while the soft-X ray loops are reconnected flux tubes filled with evaporated plasma from the photosphere.

1.3.2 In-situ Satellite Crossing

Ever since the proposal of Petschek's reconnection model, various satellite missions have tried to resolve the reconnection-associated slow shocks in Earth's magnetotail and magnetopause with in-situ observations [32, 33, 103, 99, 100, 79, 42, 112]. In Fig. 1.9 we show a slow shock structure documented in Seon et al. (1996). It is data collected from time 2145 UT to 2205 UT March 9 1993, when the Geotail satellite flew across the distant magnetotail from the plasma sheet (yellow region in Fig. 1.2) to the tail lobe (white region of Fig. 1.2) at $(-181.8, 27.2, 25.0)R_e$ in GSM coordinates (to the right of the tail $\bigotimes$ of Fig. 1.2). Profiles of the electron density, ion velocity in the x, y, z directions, ion and electron temperatures, x, y, z magnetic field components, and the total magnetic field are shown.

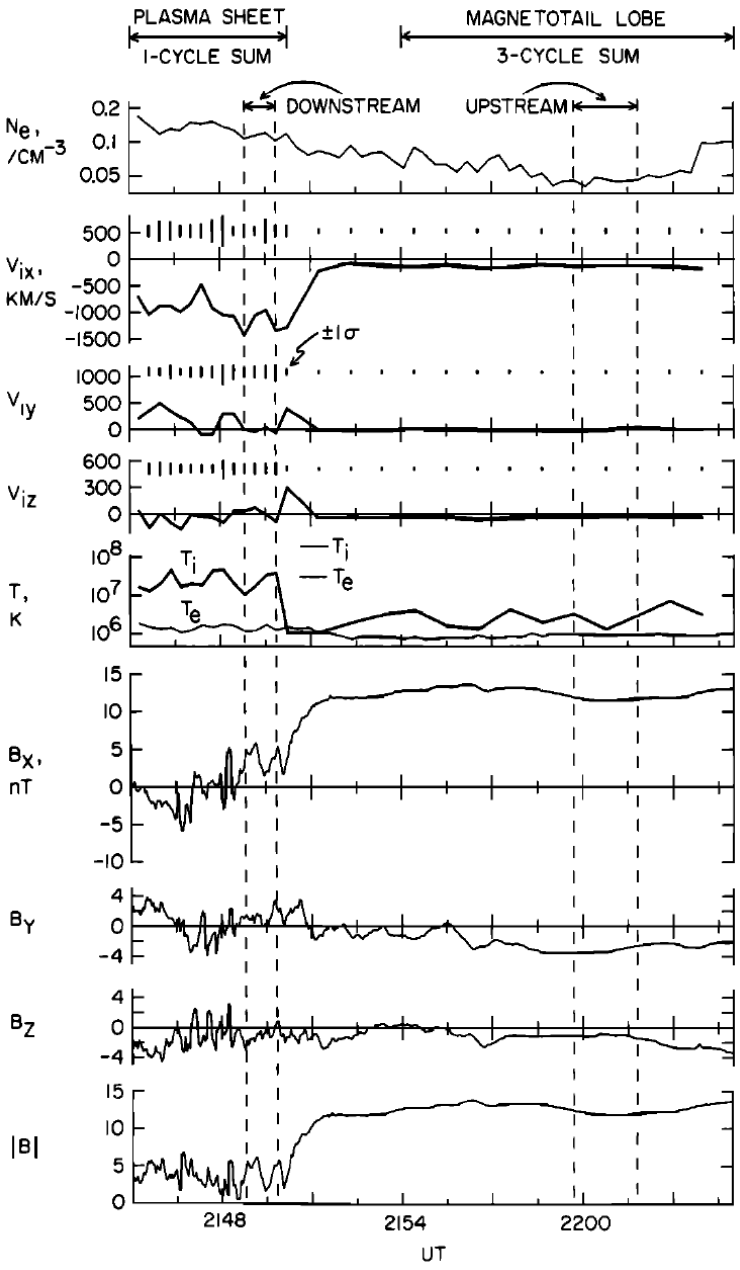

Figure 1.9: An in-situ observation of a slow shock crossing. Data from the *GEOTAIL* satellite on March 9, 1993 at GSM coordinate $(-181.8, 27.2, 25.0)R_e$ (Adapted with permission from Ref. [Seon et al., 1996]. ©1996 by the American Geophysical Union.)

The shock upstream and downstream regions are bounded by the dashed vertical lines, and the Rankine-Hugoniot jump relations were tested. The most significant features are the high $|V_{ix}|$ and T_i seen between 2145 and 2150 UT, associated with the dramatic decrease in B_x (the reconnecting field) and $|B|$. Note that this slow shock is not a switch-off slow shock, since the downstream $|B| \sim 4nT$. There is a long wavelength large-amplitude sinusoidal $B_y \sim 4nT$ component (the out-of-plane field) in the downstream region, that appears turbulent with many small-scale waves sitting on it.

However, although in-situ observations of slow shocks in the magnetotail exist, they are relatively rare and mostly non-switch-off, suggesting that the MHD picture of Petschek may not tell the complete story.

1.3.3 Large-Scale Kinetic Simulations

In-situ observations of switch-off slow shocks in space are rare when satellites traverse reconnection exhausts. The same is true in hybrid and PIC simulations of reconnection. Unlike resistive-MHD simulations (with localized resistivity), switch-off slow shocks do not appear in large-scale kinetic reconnection simulations [66, 71, 78].

In Fig. 1.10 we show results from 2-D hybrid simulations conducted by Lottermoser et al. (1998). The left panel shows the reconnection outflow structure that reaches $480\lambda_0$ away from the reconnection site, where λ_0 is the upstream ion-inertial scale. The reconnection site is at $(x/\lambda_0, y/\lambda_0) = (0, 0)$, and the contours represent

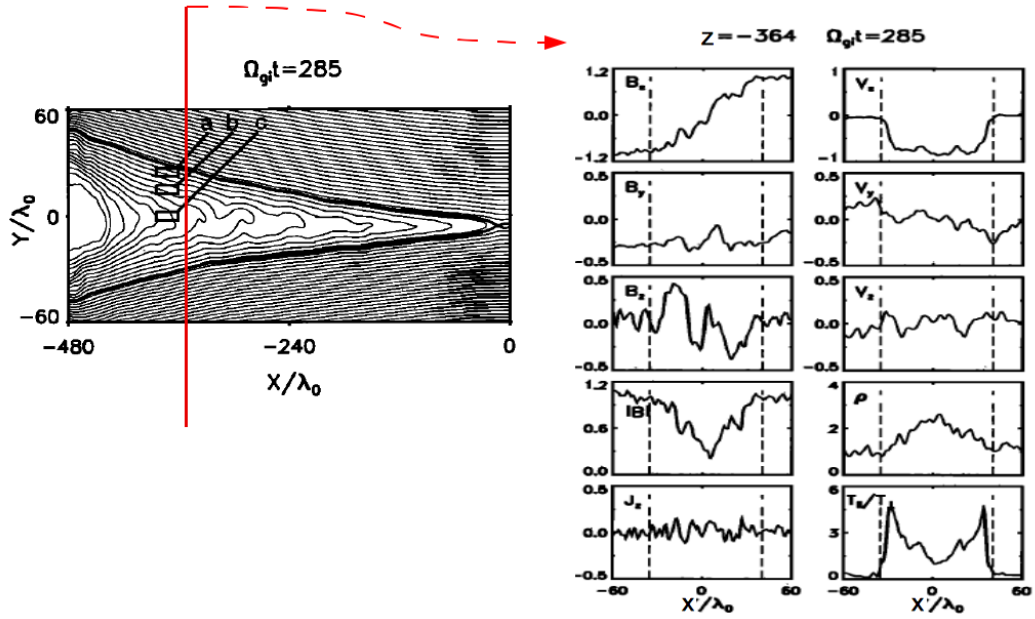

Figure 1.10: A large-scale hybrid reconnection simulation. λ_0 is the ion-inertial scale. (Adapted with permission from Ref. [Lottermoser et al., 1998] ©1998 by the American Geophysical Union.)

the in-plane magnetic field. The right panels show cuts along the red line in the 2-D picture. We see the Alfvénic reconnection outflow (V_x, top right) as expected, but several unexpected features are also prominent. There is no switch-off behavior in the reconnecting magnetic field (B_x, top left), the downstream has a large out-of-plane component (B_z, 3rd down on left), and a strong firehose-sense temperature anisotropy ($T_\parallel > T_\perp$, bottom right) exists inside the exhaust. In the 2-D picture, a clear warping behavior of the in-plane magnetic field within the exhaust is seen. These authors attribute the disappearance of switch-off slow shocks to the firehose-like or kink-like instability that causes this warping. They have also pointed out the existence of a "step-like" slow shock (non-switch-off) as seen in the B_x component from $B_x = 0.5$ to 1.0 (normalized to the upstream field).

No signature of Petscheck's switch-off slow shocks has been seen in PIC reconnection simulations as well (see Fig. 1.11) [28]. A contributing factor may be to the relatively small domain sizes in the shock normal direction ($\hat{\mathbf{x}}$), which only extends for 10 d_i in this simulation, where d_i is, again, the ion-inertial scale. In Fig. 1.11, panel (a) shows the out-of-plane electron current density, with the reconnection site at $(x/d_i, z/d_i) \sim (0, 20)$. The plasma downstream of the reconnection site exhibits large firehose-sense temperature anisotropies. In panels (b) and (c), we see turbulence in the B_x component correlated with the unstable firehose region where $\varepsilon < 0$; a cut of the firehose stability parameter $\varepsilon = 1 - \mu_0(P_\parallel - P_\perp)/B^2$ at $z = -35d_i$ is shown in (d).

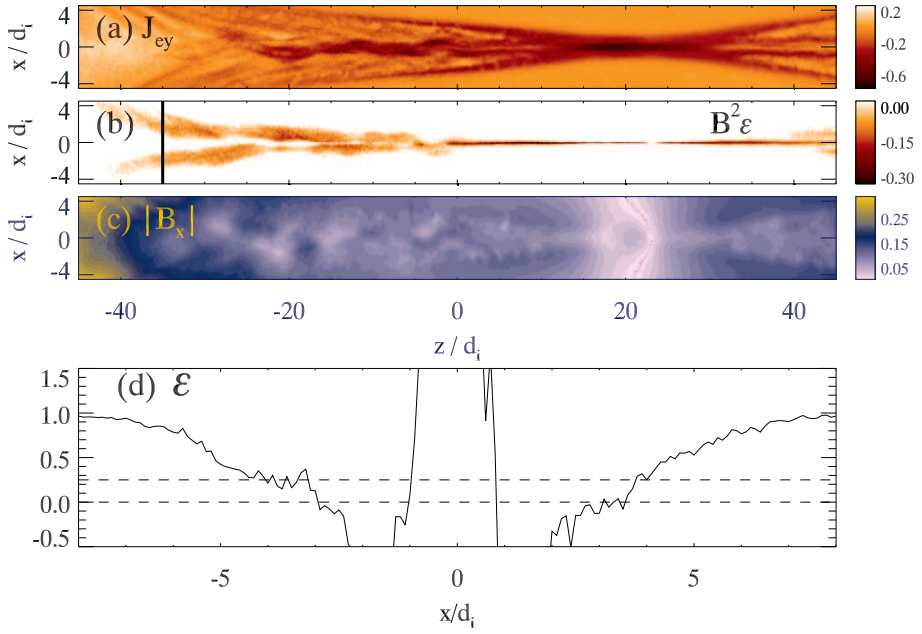

Figure 1.11: The exhaust from steady reconnection in a PIC simulation. Panel (a): The out-of-plane electron current density J_{ez}; Panel (b): $B^2\varepsilon$, where positive values have been set to 0. The colored region is firehose unstable; Panel (c): The magnitude of B_x showing the development of 2-D turbulence; Panel (d): A cut of ε at $x/d_i = -35$ (the vertical line in (b)). The horizontal lines demarcate $\varepsilon = 0.25$ and $\varepsilon = 0$.

1.3.4 Summary of Unsolved Issues and Motivation

The firehose-sense temperature anisotropy is notable since in-situ observations of the solar wind clearly show that the proton temperature anisotropy is bounded by the marginal firehose and mirror mode stability boundaries [4]. Hence, it is of interest to study the fully self-consistent generation of temperature anisotropy distributions across the reconnection exhaust more closely, and their feedback on the propagation and steepening of slow shocks. We particular wish to answer the following questions that naturally arise from the discussions of the previous sections. Why are the observations of Petschek-reconnection-associated switch-off slow shocks rare? Is the downstream 2-D turbulence in the reconnection outflow region associated with the firehose instability? Does the temperature anisotropy itself affect the formation of slow shocks? Can the reconnection exhaust boundary accelerate particles to super-thermal energies?

1.4 Our Approach: The Riemann Problem

We are interested in the exhaust structure far downstream of the x-line (reconnection site). Instead of simulating reconnection in a very large domain, we perform simulations in narrow boxes with dimensions $l_z \ll l_x$. The strategy is to use time as a proxy for space in order to reduce the computational burden. As in Fig. 1.12, and unlike the initial set-up for reconnection, we begin with oppositely directed reconnecting fields plus a uniform normal field B_x at time t_0. The existence of B_x induces a unbalanced tension force that shoots plasma downward, and also

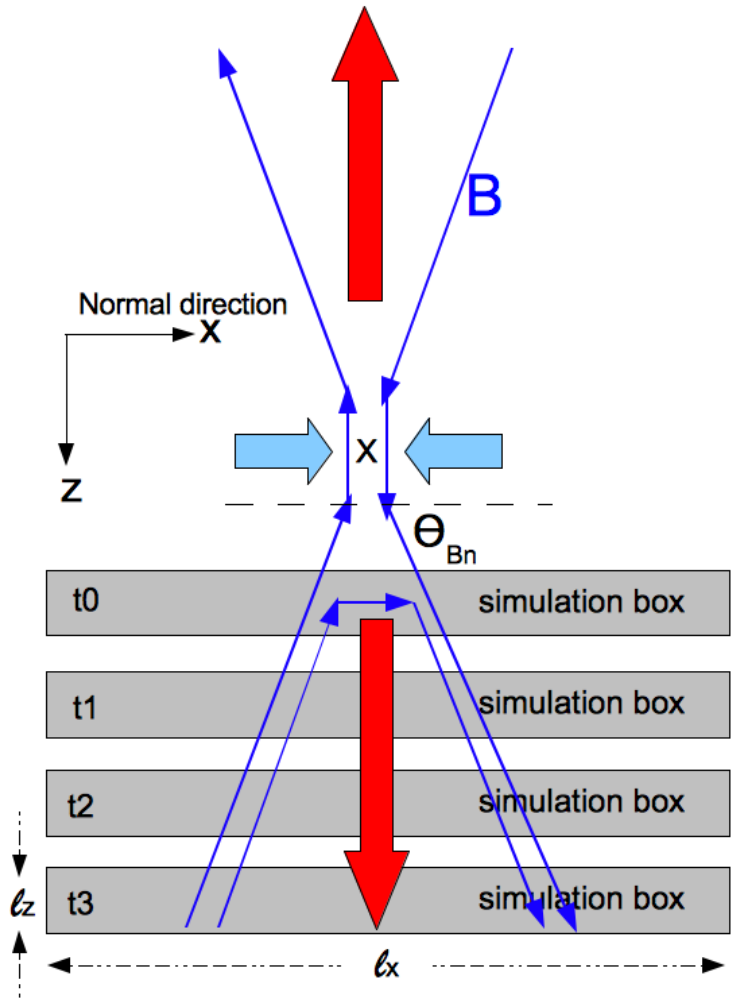

Figure 1.12: A cartoon showing the relationship between our Riemann problem simulation and the structure of an X-line.

drives waves away (via, the kinked magnetic field) from the current sheet in the x-direction. As time goes on (for instance, from t_0, t_1, t_2 to t_3 in the diagram), the simulation box will correspond to locations farther and farther away from the x-line. Therefore a stacked time sequence of plots would show the 2-D structure of the reconnection exhaust, which is similar to the idea of "Computerized Tomography" used in scanning the full structure of the human brain. When $\theta_{BN} \sim 83°$, the simulation will closely correspond to a reconnection exhaust with a normalized reconnection rate $B_x/B_{z,\mathrm{up}} \sim 0.1$ [101, 102].

When l_z is small our simulations are essentially 1-D, although we do perform runs with larger l_z to investigate the possibility of developing 2-D turbulence. In this Riemann formulation, waves (*e.g.,* fast, intermediate, and slow modes in the fluid model) will propagate away from the reconnection current sheet, at their characteristic speeds, and steepen into shocks, spread into rarefactions, or maintain their initial shapes based on their own nonlinearities.

Before we introduce the full kinetic results in the next chapter, we need to outline some background knowledge of waves and the 1-D Riemann problem in ideal MHD.

1.4.1 Linear and Nonlinear MHD Waves

There are seven equations in 1-D ideal-MHD (Eq.(1.1)-(1.7) without the η_r term and $\partial_y = \partial_z = 0$) that include partial derivatives on both time and space. Therefore there are seven waves: two fast (F) modes that propagate in the positive

and negative normal direction ($\hat{\mathbf{x}}$ here), two intermediate (I) modes, two slow (SL) modes, and a non-propagating entropy (E) mode. By linearizing the 1-D ideal-MHD equation, we obtain their speeds,

$$C_E = 0 \tag{1.25}$$

$$C_I = C_A \cos\theta \tag{1.26}$$

$$C_{F,SL} = \left\{ \frac{1}{2} \left[(C_S^2 + C_A^2) \pm \sqrt{(C_S^2 + C_A^2)^2 - 4C_S^2 C_I^2} \right] \right\}^{1/2} \tag{1.27}$$

where the sound speed $C_S = \sqrt{\gamma P/\rho}$ with γ being the adiabatic index which is 5/3 in monatomic plasmas when the heat flux $\mathbf{Q}$ vanishes, and the Alfvén speed $C_A = B/\sqrt{\mu_0 \rho}$. The plus (minus) sign of Eq. (1.27) corresponds to the fast (slow) mode. The Friedrich diagrams in Fig. 1.13 show the dependence of these phase speeds on propagation angle (θ). The magnetic field is in the vertical direction, a radial vector from the origin to a given point on a curve measures the speed and the propagation angle. It is apparent that the three propagating waves always have the speed ordering $C_F \geq C_I \geq C_{SL}$ in both the plasma $\beta < 1$ and $\beta > 1$ cases. Therefore we expect to see waves propagate out from a central discontinuity in the order shown in Fig. 1.14. Note that the structures of the Friedrich diagrams differ when β crosses unity. For $\beta < 1$, the fast mode and intermediate mode propagate at the same speed (are degenerate) in the parallel direction, while the slow mode propagates at the sound speed. When $\beta > 1$, the slow mode and intermediate mode degenerate in the parallel direction, while the fast mode propagates at the sound speed.

There are nonlinear waves related to each of these linear MHD modes. By

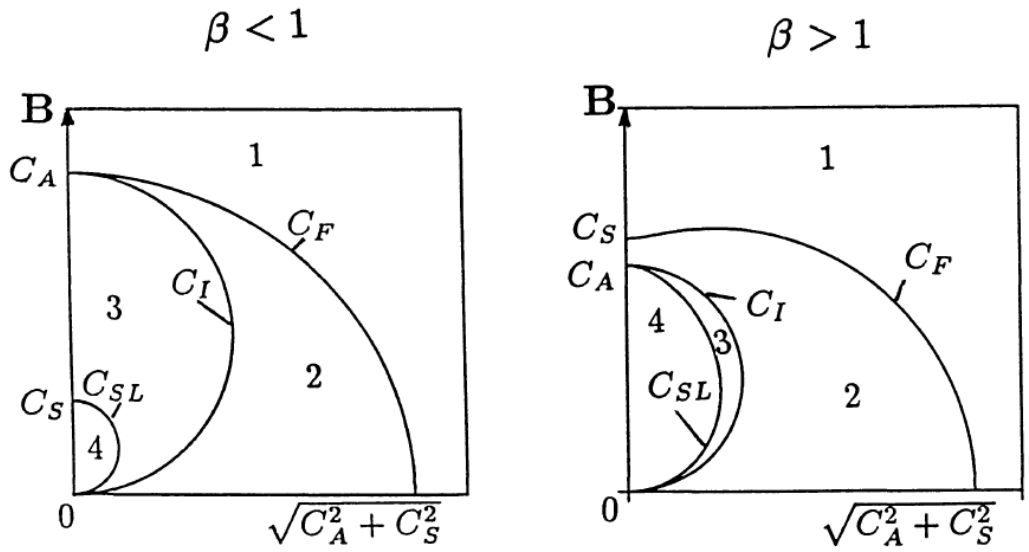

Figure 1.13: The Friedrich diagrams display the phase speeds of MHD modes as a function of propagation angle. The direction of the ambient magnetic field is upward. (Reprinted with permission from Ref. [Lin and Lee, 1993] ©1993 by the Kluwer Academic Publishers)

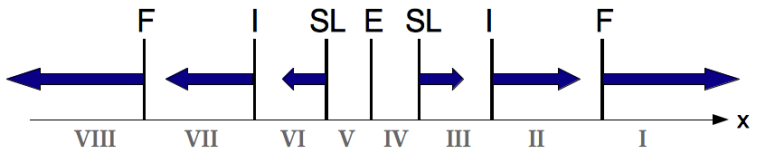

Figure 1.14: MHD waves that propagate out from a central interface.

Table 1.1: Overview of MHD nonlinear waves (Ref. [Lin and Lee, 1993]).

type	wave	properties
shock	FS:	$[V_n] < 0,\quad [\lvert\mathbf{B}_t\rvert] > 0,\quad [\rho] > 0,\quad [P] > 0$
	SS:	$[V_n] < 0,\quad [\lvert\mathbf{B}_t\rvert] < 0,\quad [\rho] > 0,\quad [P] > 0$
	IS:	$[V_n] < 0,\quad [\lvert\mathbf{B}_t\rvert] \neq 0,\quad [\rho] > 0,\quad [P] > 0$
discontinuity	RD:	$V_n = B_n/\sqrt{\mu_0\rho},\quad [\mathbf{V}_t] = [\mathbf{B}_t]/\sqrt{\mu_0\rho},\quad [\rho] = 0,\quad [P] = 0$
	CD:	$V_n = 0,\quad B_n \neq 0,\quad [\mathbf{V}_t] = 0,\quad [\mathbf{B}_t] = 0,\quad [\rho] \neq 0,\quad [P] = 0$
	TD:	$V_n = 0,\quad B_n = 0,\quad [\mathbf{B}_t] \neq 0,\quad [\rho] \neq 0,\quad [P + B^2/(2\mu_0)] = 0$
rarefaction	FR:	$[V_n] > 0,\quad [\lvert\mathbf{B}_t\rvert] < 0,\quad [\rho] < 0,\quad [P] < 0$
	SR:	$[V_n] > 0,\quad [\lvert\mathbf{B}_t\rvert] > 0,\quad [\rho] > 0,\quad [P] < 0$

Subsrcipts "n" and "t" denote the normal and tangential components with respect to the shock front.

writing the 1-D ideal MHD equations in conservative form, we can easily write down the Rankine-Hugoniot jump relations (these are the $\varepsilon = 1$ limit of Appendix A. 4). From the Rankine-Hugoniot (RH) jump conditions we can identify all possible shocks and discontinuities. These are presented in Table 1.1 (note that $[B_n] = 0$ always holds). A fast shock (FS) requires a super-fast to sub-fast transition, which means the upstream fast Mach number $M_{u,F} \equiv V_{n,u}/C_{F,u} > 1$ and the downstream fast Mach number $M_{d,F} \equiv V_{n,d}/C_{F,d} < 1$ where $V_{n,u}$ and $V_{n,d}$ are measured in the shock frame. This is a transition from region 1 to region 2 in the Friedrich diagram in Fig. 1.13, therefore the FS is also conventionally called a 1-2 FS. Similarly, the slow shock (SS) requires a super-slow to sub-slow transition and therefore is called a 3-4 SS. The intermediate shock (IS) requires a super-intermediate to sub-intermediate transition, and there are four possible solutions 1-3 IS, 1-4 IS, 2-3 IS and 2-4 IS. A rotational discontinuity (RD) is the weak limit of an IS, with both the upstream and downstream intermediate Mach number being unity. The contact discontinuity (CD) originates from the non-propagating entropy mode, with the density changing on the

two sides of the discontinuity. The tangential discontinuity (TD) is just a stationary solution where nothing occurs, since the two different states are pressure balanced and peacefully sit side by side. Note that a shock always requires a compression ratio, ρ_d/ρ_u, larger than unity. Depending on the circumstances, the fast and slow modes can also spread out as fast rarefactions (FR) and slow rarefactions (SR) in which the density decreases ($\rho_d/\rho_u < 1$). Instead of steepening into a sharp transition as in shocks, the transition regions of rarefactions become broader with time. The weak rarefaction solutions can be found by replacing the energy jump relation in the RH jump conditions with the conservation of entropy, $[P\rho^{-\gamma}] = 0$.

The basic configurations of the magnetic field for these shocks and discontinuities are shown in Fig. 1.15. In the lower right, we introduce the basic format with the magnetic field denoted as blue arrowed lines (the arrow direction can be reversed), and shock front as a black vertical line. The right (left) side is the upstream (downstream). One important property of MHD shocks and discontinuities is their coplanar behavior, which means that upstream magnetic field, downstream magnetic field and the shock normal all lie in the same plane.

Across a FS the magnetic field bends away from the normal, and therefore the strength of the magnetic field increases ($|B|$ is proportional to the magnetic field line density). In contrast, across a SS the downstream magnetic field bends toward the normal, and therefore the strength of magnetic field decreases. The tangential magnetic field across fast and show shocks never changes sign. The RD only reverses the tangential direction of the magnetic field, without changing the thermal state. The IS also changes the sign of tangential magnetic field, the magnitude of the total

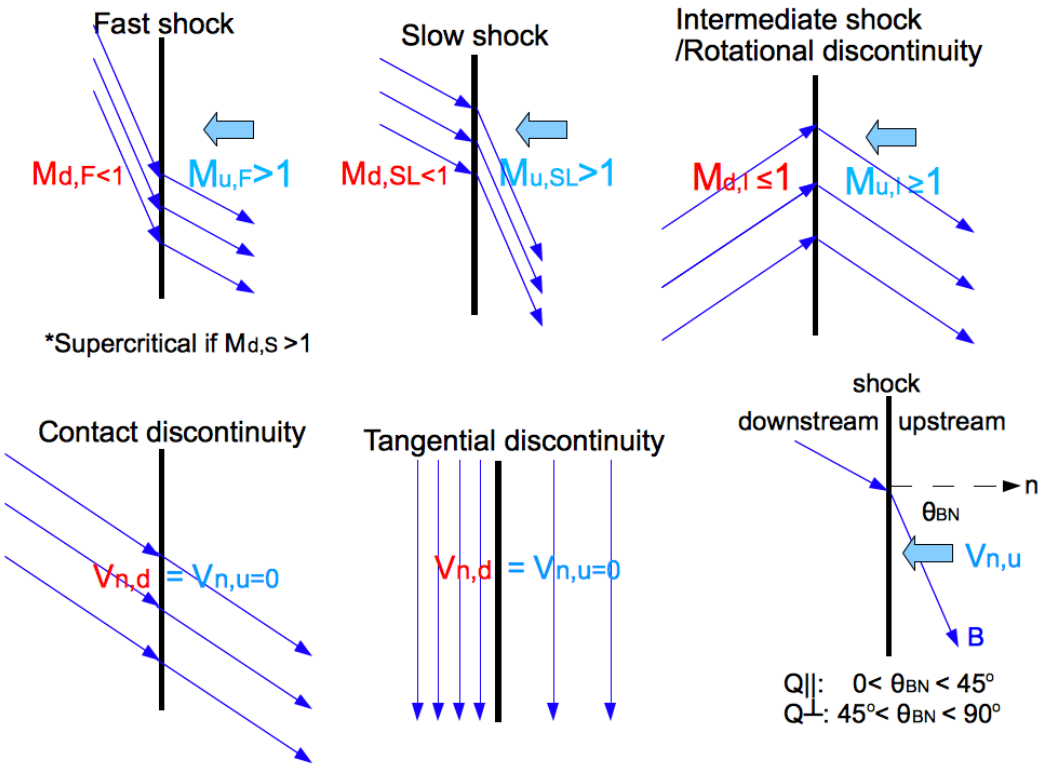

Figure 1.15: The basic magnetic field structures (thin blue arrowed lines) of MHD shocks and discontinuities. ($Q_{\parallel}$ means quasi-parallel, $Q_{\perp}$ means quasi-perpendicular. When the downstream is super-sonic, the fast shock is also termed supercritical.)

magnetic field, and the thermal state. The field does not change across a CD. The existence of a TD requires zero normal direction magnetic field.

The kinetic structure of fast shocks has been intensely studied (see the review article [108] and references therein), since, for instance, the heliospheric termination shock, the Earth's bow shock, and shocks associated with coronal mass ejections, supernova explosions, Gamma Ray Bursts and astrophysical jets are all fast shocks. Compared to fast shocks, kinetic slow and intermediate shocks are not as well understood. The downstream region of oblique slow shocks is expected to have high β, strong temperature anisotropy, kinetic streaming effects, strong damping, *etc.,* that greatly complicate the analysis. In addition, the slow propagation, and therefore slow formation, of oblique slow shocks requires substantially more computer resources to explore.

1.4.2 MHD Riemann Problems

The general Riemann problem addresses the question of how characteristic nonlinear waves connect to each other as they propagate out from an interface between two uniform states that initially adjoin. As in Fig. 1.14, a way to solve the Riemann problem is to numerically find a set of nonlinear solutions of the seven MHD waves (shocks or rarefactions) that connect regions I to VIII. The two ambient sides (regions I and VIII) of reconnection vary in different physical systems, Hence we expect to see different structures propagating out from the central narrow current sheet. We examine three different Riemann problems in 1-D ideal-MHD systems

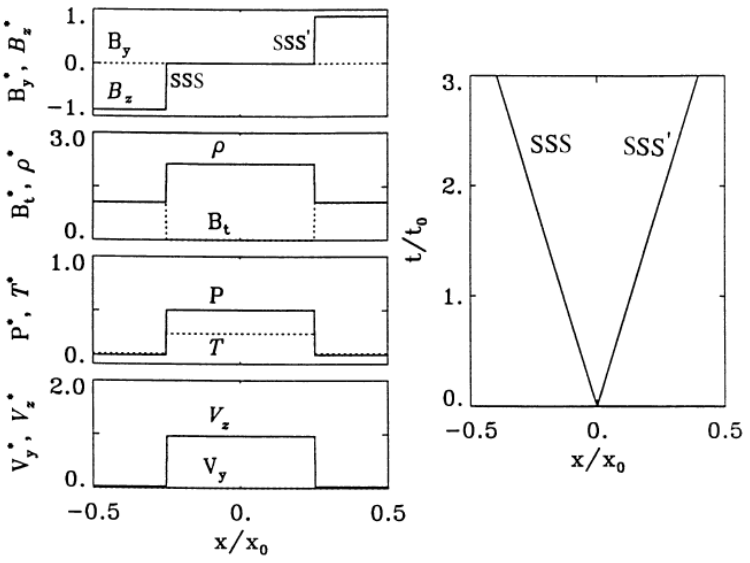

Figure 1.16: A Riemann problem with a symmetric antiparallel ambient state. (Adapted with permission from Ref. [Lin and Lee, 1993]. ©1993 by the Kluwer Academic Publishers)

that are most relevant to basic reconnection theory (all adapted from Lin and Lee's review paper (1993) [65]).

Fig. 1.16 shows a case with most of the physical parameters being equal across the interface, with the only difference being the direction of B_z. A uniform nonzero B_x is chosen. This case directly corresponds to the case of symmetric anti-parallel reconnection, which should develop into a Petschek-like structure. As time goes on, waves propagate out of the center, $x = 0$, as shown in the right panel. A pair of weak FR have already propagated out of the domain at the time shown in the left panels, and what remains is a pair of switch-off slow shocks (SSS), as expected. Jumps of various physical quantities across the SSS are documented. A switch-off slow shock is the strongest slow shock, with a maximum compression ratio, and its downstream

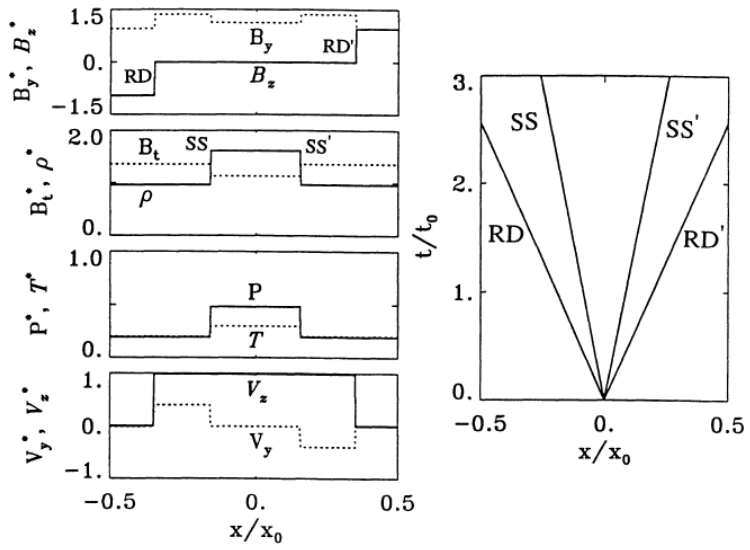

Figure 1.17: The same Riemann problem as Fig. 1.16, but with a initial uniform guide field. (Reprinted with permission from Ref. [Lin and Lee, 1993] ©1993 by the Kluwer Academic Publishers)

tangential magnetic field (B_z) vanishes. It propagates at the intermediate speed of the upstream state, and therefore the presence of a nonlinear intermediate mode in front of the SSS is unnecessary. The SSS has converted most of the upstream magnetic field energy (B_z) into Alfvénic outflows (V_z) and thermal energy (T).

Fig. 1.17 is the same as Fig. 1.16 but with an initial out-of-plane field $B_y \neq 0$. This case is directly related to the case of guide field reconnection with a constant initial out-of-plane magnetic field. We can see that the pair of SSS's in Fig. 1.16 are now replaced by a pair of RD's and SS's. The RD's rotate the B_z out to B_y while maintaining B_t constant, and are responsible for the switch-off behavior of B_z in this case. The SS's slightly decrease B_y.

Fig. 1.18 is the same as Fig. 1.16 but with an initially strong asymmetry in

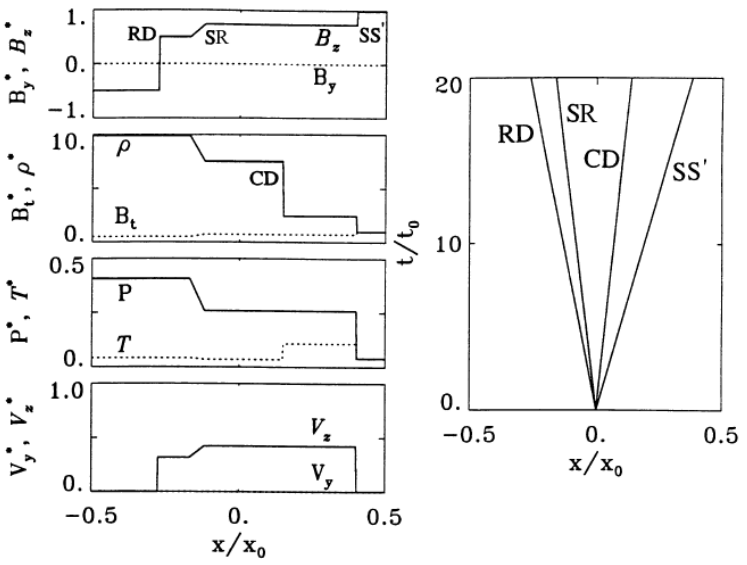

Figure 1.18: The same Riemann problem as Fig. 1.16, but with a strong asymmetry in the ambient plasma density. (Adapted with permission from Ref. [Lin and Lee, 1993] ©1993 by the Kluwer Academic Publishers)

the plasma density, where the density on the left side is higher than the density on the right side. The left SSS in Fig. 1.16 is replaced by a RD and a SR (its transition region broadens with time) now. In addition, there is a CD between the slow modes propagating to the right. This structure is closely related to Levy et al.'s (1964) [62] asymmetric reconnection model, which applies to magnetopause reconnection, with the left-hand side being solar wind plasma and the right-hand side being magnetosphere plasma.

In the next two chapters, we primarily focus on the kinetic version of the symmetric case shown in Fig. 1.16, and we will see how kinetic effects alter the picture predicted by ideal MHD. Some of the unsolved issues discussed in Sec. 1.3.4 will also be addressed.

1.5 Anisotropic MHD

Since they will be used in the following chapters, we document the anisotropic version of resistive-MHD here. The first three equations are derived from moment integrations of the Vlasov equation and the off-diagonal components of the pressure tensor are neglected [14, 45]. These equations are not closed, since an energy closure is undetermined.

$$\frac{\partial \rho}{\partial t} + \nabla \cdot (\rho \mathbf{V}) = 0 \tag{1.28}$$

$$\rho \frac{d\mathbf{V}}{dt} = -\nabla \left(P_\perp + \frac{B^2}{2\mu_0} \right) + \nabla \cdot \left\{ \left[1 - \frac{\mu_0 (P_\parallel - P_\perp)}{B^2} \right] \frac{\mathbf{BB}}{\mu_0} \right\} \tag{1.29}$$

$$\frac{\partial}{\partial t} \left(\frac{\rho V^2}{2} + \frac{B^2}{2\mu_0} + \frac{3}{2} P \right) + \nabla \cdot \left[\left(\frac{\rho V^2}{2} + \frac{3}{2} P \right) \mathbf{V} + \mathbf{P} \cdot \mathbf{V} + \frac{\mathbf{E} \times \mathbf{B}}{\mu_0} + \mathbf{Q} \right] = 0 \tag{1.30}$$

$$\frac{\partial \mathbf{B}}{\partial t} = -\nabla \times \mathbf{E} \tag{1.31}$$

$$\nabla \times \mathbf{B} = \mu_0 \mathbf{J} \tag{1.32}$$

$$\mathbf{E} = -\mathbf{V} \times \mathbf{B} + \eta_r \mathbf{J} + \frac{1}{ne} (\mathbf{J} \times \mathbf{B}) \tag{1.33}$$

$$\nabla \cdot \mathbf{B} = 0 \tag{1.34}$$

where $P_\parallel$, $P_\perp$ are the pressure parallel and perpendicular to local magnetic field, respectively. $P \equiv (P_\parallel + 2P_\perp)/3$, $\mathbf{P} \equiv P_\perp \mathbf{I} + (P_\parallel - P_\perp)\mathbf{BB}/B^2$ where $\mathbf{I}$ is the unit tensor, and $\mathbf{Q} \equiv \int d^3v (\frac{1}{2} m \delta v^2 \delta \mathbf{v}) f$ (where $\delta \mathbf{v} \equiv \mathbf{v} - \langle \mathbf{v} \rangle$) is the heat flux in the energy equation, Eq. (1.30). We have also included the Hall term $\mathbf{J} \times \mathbf{B}/ne$ in the generalized Ohm's law, Eq. (1.33). This is the same Hall term that induces whistler waves to open the reconnection nozzle. It also causes shocks to radiate rotational dispersive wavetrains in the upstream or downstream regions, which will be briefly commented on later in this work.

Chapter 2

PIC simulations of Riemann Problem

2.1 Overview

Unanswered questions remain concerning the kinetic structure of slow shocks in a collisionless plasma and the associated mechanisms leading to particle heating. In previous work, kinetic slow shocks were studied numerically in hybrid codes by initializing the system with the slow shock jumps predicted by MHD [107] or, later, by the piston [118] and flow-flow methods [81]. Some of the main focuses of these works were the backstreaming beam-driven electromagnetic ion-ion cyclotron instability (EMIIC) [118, 81], which has been suggested to as the cause of the nonsteady behavior of slow shocks, and the formation and damping of downstream large amplitude dispersive wavetrains [107, 65]. Recently, the dissipation due to electrons and kinetic Alfvén waves (KAWs) exited by the EMIIC instability was studied by the piston method in particle-in-cell (PIC) simulations [22, 125, 123].

To address this issue, we perform 2-D PIC simulations that extend the simulation size in the normal direction to $\sim 800 d_i$ by ignoring the X-line and instead examining the conceptually simpler Riemann problem. This set-up as discussed in Sec. 1.4 more closely resembles the reconnection outflow exhaust than that produced by other methods of generating shocks. Similar kinetic simulations of these Riemann problems have been carried out with a 1-D hybrid model [66]. 2-D Riemann

problems have also been carried out in hybrid simulations [98] where the 2-D downstream turbulence appeared to diminish the downstream wavetrains associated with switch-off slow shocks. Upstream perpendicular heating from the by EMIIC instability and the subsequent excitation of anisotropic (Alfvén/ion cyclotron (AIC)-like) instability and the resultant parallel AIC waves have also been studied in similar 2-D Riemann problems [19, 20].

In Sec. 2.2 we introduce our simulation model and the initial set-up of the Riemann problem. In Sec. 2.3 we discuss the general profiles of a run with $\theta_{BN} = 75^\circ$ (the angle between the upstream magnetic field and the normal direction ($\hat{\mathbf{x}}$)). Section 2.4 points out that the counterstreaming ions drive the firehose stability parameter $\varepsilon \equiv 1 - \mu_0(P_\parallel - P_\perp)/B^2$ down (increase the firehose-sense temperature anisotropy) in the downstream region. In Sec. 2.5 we show that a more oblique shock results in a lower ε in the downstream region. The structure of the magnetic field performs a transition from a coplanar decrease to a non-coplanar rotation at $\varepsilon \sim 0.25$, which differs from the traditional slow shock transition with dispersive wavetrains. In Sec. 2.6 the stability of the downstream rotational wave is studied with numerical experiments. The tendency for a spatially modulated rotational wave to radiate d_i-scale waves is identified. The resulting d_i-scale waves counterbalance the ε decrease driven by the counterstreaming ions. Finally, we summarize the results and discuss potential implications in Sec. 2.7.

2.2 Simulation Models and Details

Most of our PIC simulations use a narrow computational domain, $l_z \times l_x = 1.6d_i \times 1638.4d_i$ to capture the nonlinear wave propagation (mainly the slow shock pair in Petscheck's reconnection model) far downstream from the reconnection site. The simulations presented here are two-dimensional, *i.e.*, $\partial/\partial y = 0$, and periodic in the $z - x$ plane. The initial equilibrium consists of a double Harris-like current sheet (although we only focus on a single current sheet) superimposed on an ambient population of uniform density n_a:

$$B_z = B_{z,a} \tanh(x/w_i); \qquad n_{p,e} = n_h \mathrm{sech}^2(x/w_i) + n_a, \tag{2.1}$$

where $B_{z,a}, n_h, n_a$ are constants, the subscript "a" stands for the asymptotic (far upstream) values, "h" stands for Harris and w_i is the initial half-width of the current sheet (this is the symmetric case corresponding to Fig. 1.16). We initialize both the Harris plasma and background plasma with an isotropic Maxwellian distribution. Unlike the initial set-up for reconnection, we begin with a constant normal field B_x. Although the initial total pressure is balanced, the existence of B_x causes a tension force that drives wave propagation away from the current sheet in the x-direction. Again, the $B_{x,a}/B_{z,a} = 0.1$ case (*i.e.*, $\theta_{BN} \sim 83^\circ$ with $\cos\theta_{BN} \equiv B_{x,a}/B_a$) corresponds to a reconnection exhaust with a normalized reconnection rate of 0.1 [101, 102].

In our particle-in-cell code p3d [126], the electromagnetic fields are defined on gridpoints and advanced in time with an explicit trapezoidal-leapfrog method using second-order spatial derivatives. The Lorentz equation of motion for each particle

is evolved by a Boris algorithm where the velocity $\mathbf{v}$ is accelerated by $\mathbf{E}$ for half a timestep, rotated by $\mathbf{B}$, and accelerated by $\mathbf{E}$ for the final half timestep. To ensure that $\nabla \cdot \mathbf{E} = \rho/\epsilon_0$ a correction electric field is calculated by inverting Poisson's equation with a multigrid algorithm.

The magnetic field is normalized to the asymptotic magnetic field B_a, the density to the asymptotic density n_a, velocities to the Alfvén speed $C_A \equiv B_a/\sqrt{\mu_0 m_i n_a}$, lengths to the ion inertial length $d_i \equiv \sqrt{m_i/\mu_0 n_a e^2}$, times to the inverse ion cyclotron frequency $\Omega_{ci}^{-1} \equiv m_i/B_a e$, and temperatures to $m_i C_A^2$. Other important parameters are $m_i/m_e = 25$, $c/C_A = 15$, $n_a = 1$, $n_h = 1.5$, $B_a = 1$, and the asymptotic value of initial $T_{i,e} = 0.1$, which imply that $\beta_a = 0.4$. The initial electron temperature is uniform, while the ion temperature varies so as to ensure pressure balance in the x-direction. We take the time step $\Delta t = 0.0025$ and grid size $\Delta = 0.025$. We usually take $w_i = d_i$ since the thickness of the dissipation region during reconnection is on the d_i scale [101, 13]. There are $\sim 4 \times 10^8$ particles in a single run. Table 2.1 gives further details of the various runs.

Runs **a**, **b**, **c**, **d**, **f**, **g**, **h** and **k** (all have $l_z = 1.6 d_i$, except the $\theta_{BN} = 83°$ case) will be further discussed in this work. Even though the 75° case with a larger $l_z = 6.4 d_i$ (Run **i**) shows downstream 2-D turbulence, the evolution is quite similar to the narrow Run **f**. As can be seen in Table 2.1, 2-D turbulence tends to occur for oblique ($\theta_{BN} > 75°$) cases when l_z is large enough. Curves plotted throughout the rest of this chapter are quantities averaged in the z-direction, since most runs discussed here do not have any significant variation in the z-direction. The 2-D turbulence of $\theta_{BN} = 83°$(Run **k**) will also be discussed.

Table 2.1: Overview of runs.

Run	θ_{BN}	w_i	B_g[1]	Domain Size ($l_z \times l_x$)	Gridpoints	$\rightarrow$[2] 2-D turbulence
a	30°	1	0	1.6×1638.4	64×65536	x
b	45°	1	0	1.6×1638.4	64×65536	x
c	52°	1	0	1.6×1638.4	64×65536	x
d	60°	1	0	1.6×1638.4	64×65536	x
e	60°	1	0	6.4×819.2	256×32768	x
f	75°	1	0	1.6×1638.4	64×65536	x
g	75°	10	0	1.6×1638.4	64×65536	x
h	75°	1	0.2	1.6×1638.4	64×65536	x
i	75°	1	0	6.4×1638.4	256×65536	$\surd$
j	83°	1	0	1.6×819.2	64×32768	x
k	83°	1	0	6.4×819.2	256×32768	$\surd$

[1] B_g is an initial uniform guide field in the y-direction.
[2] "$\rightarrow$" means "resulting in".

2.3 General Features of the 75° Case

A representative case of $\theta_{BN} = 75°, w_i = 1d_i, B_g = 0$ (Run **f**; hereafter referred to as the "75° run") at time $200/\Omega_{ci}$ is documented in Fig. 2.1. As soon as the simulation begins, a pair of fast rarefaction waves propagate out from the discontinuity with speed $\sim 1.1C_A$, while the slow shocks with their downstream rotational waves have speed $\sim 0.15C_A$. As in ideal MHD with a symmetric initial condition and zero guide field, a pair of switch-off slow shocks are expected to follow the fast rarefaction waves, as shown in Fig. 2.1(b) [65]. A switch-off slow shock (*i.e.*, the strongest slow shock, whose tangential magnetic field vanishes downstream of the shock) propagates at the upstream intermediate speed, while the downstream linear slow mode speed equals the downstream linear intermediate speed. The linear slow mode and intermediate mode are known to become degenerate at parallel propa-

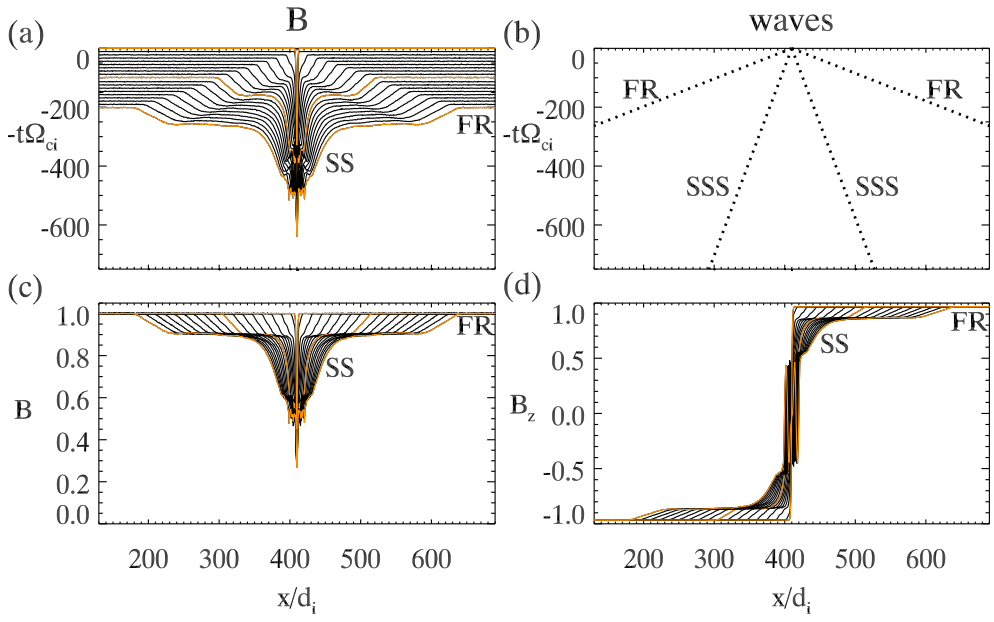

Figure 2.1: The evolution of a system with $\theta_{BN} = 75°$ (Run **f**). Panel (a): The evolution of B from time $0-200/\Omega_{ci}$. A pair of fast rarefactions (FR) propagate out from the symmetry line, followed by a pair of slow shocks (SS). Each curve has been shifted so that it intersects the vertical axis at the given time. The time between the yellow curves is $100/\Omega_{ci}$; Panel (b): The predicted FR and switch-off slow shock (SSS) from ideal MHD theory; Panel (c): The same as (a) but with the vertical axis measuring B; Panel (d): The evolution of B_z from time $0 - 200/\Omega_{ci}$.

gation when the plasma β (plasma thermal pressure/magnetic pressure) exceeds 1. The downstream rotational waves are often identified as dispersive wavetrains. The essential physics of this wavetrain can be described by a two-fluid model [17], or by Hall-MHD [40].

Further details of the slow shock pair are shown in Fig. 2.2. The most significant feature differing from the ideal MHD model is the presence of a large downstream temperature anisotropy $\varepsilon \equiv 1 - \mu_0(P_{\|} - P_{\perp})/B^2$ shown in panel (a). The corresponding magnetic field structure is shown in panel (b), where the left-hand-

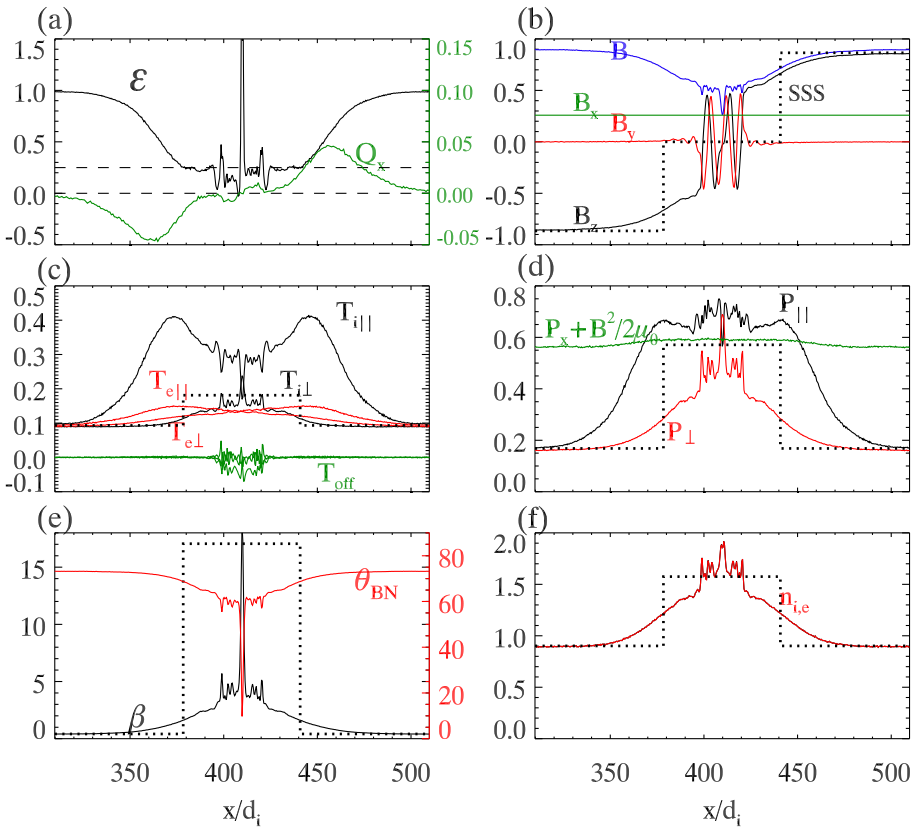

Figure 2.2: Parameters from the run with $\theta_{BN} = 75°$ (Run **f**) at time $200/\Omega_{ci}$. Panel (a): Temperature anisotropy ε and x-direction heat flux Q_x; Panel (b): Magnetic field components; Panel (c): Parallel and perpendicular temperatures (the off-diagonal components $T_{ixy}, T_{ixz}, T_{iyz}$ are plotted together in green, denoted as $T_{\rm off}$, and are small) ; Panel (d): Total plasma pressure components and $P_x + B^2/2\mu_0$. Panel (e): The plasma β and local $\theta_{BN} = \cos^{-1}(B_x/B)$; Panel (f): Plasma density. The dotted curves in each panel are the predicted magnitude and position of the switch-off slow shocks (SSS) from isotropic MHD for B_z in (b), T in (c), P in (d), β in (e), and n in (f).

polarized rotational wave is clearly seen (the polarization will be discussed further in the hodograms of Fig. 2.6). The value of ε drops from 1.0 upstream of the slow shock to ~ 0.25 around the nearly constant-magnitude rotational waves found downstream. The anisotropy factor ε affects the strength of the tension force, which in the fluid theory is proportional to $\varepsilon[(\mathbf{B}\cdot\nabla)\mathbf{B}/\mu_0]_\perp$ [95] (see the last term of Eq. (1.29)). When ε is positive, the magnetic field has a restoring tension force, while a negative value makes the tension force operate in the opposite way, driving the firehose instability. Viewed another way, the phase speed of an intermediate mode is $C_I \equiv \sqrt{\varepsilon} C_A \cos(\theta_{BN})$. Therefore, as ε drops the intermediate mode becomes slower, or even stops propagating, going firehose unstable for $\varepsilon < 0$. The x-direction heat flux $Q_x \equiv \int d^3v (\frac{1}{2} m \delta v^2 \delta v_x) f$, where $\delta\mathbf{v} \equiv \mathbf{v} - \langle\mathbf{v}\rangle$, is also documented in (a). The heat flux peaks inside the transition from upstream of the slow shock to the downstream rotational waves, and then becomes negligible. This fact is used in the next chapter. In panel (c), the parallel ion temperature increases sharply in the weak field region, while the perpendicular ion temperature is nearly constant. The electrons are nearly isotropic across the shock. In panel (d), the parallel plasma pressure and perpendicular plasma pressure are shown, and the nearly constant normal direction pressure balance $P_x + B^2/2\mu_0$ indicates the absence of fast modes in the reversal region. Panel (e) shows the associated variations in β and the local θ_{BN} and panel (f) documents the density profiles. For comparison, the black dotted curves in each panel show the predicted jumps and positions of slow shocks in the ideal MHD version of this global Riemann problem [65].

Within the MHD predicted switch-off slow shock (SSS) jump (B_z from ~ 0.9

to 0) shown in panel (b), a coplanar transition decreases the upstream B_z (black solid curve) from ~ 0.9 to ~ 0.5. After this, the magnetic field structure rotates in the non-coplanar direction and exhibits nearly constant $|B| \sim 0.5$ inside the downstream rotational waves. The tangential magnetic field eventually drops to zero in the center, as the symmetry of the initial conditions demands. We identify the coplanar transition as a slow shock transition, where the major enhancements of the temperatures, pressures, and densities and the decrease in $|B|$ occur. Note the jumps of $|B|$ and B_z from ~ 0.9 to ~ 0.5 are well maintained from the beginning to the later time in Fig. 2.1(c) and (d), which suggests that this transition is associated with one of the MHD nonlinear waves with a jump determined by the initial condition. The constancy of the total magnetic field (~ 0.5), density (~ 1.5) and β (~ 4.0) inside the downstream rotational wave and the fact that it propagates at the intermediate speed ($\sqrt{\varepsilon}B_x/\sqrt{\mu_0\rho}$) suggest an intermediate-wave-like behavior. A similar step-like decrease in $|B|$ identified as a slow shock was also reported in the downstream of a large-scale hybrid reconnection simulation [71].

2.4 The Source of Temperature Anisotropy: Alfvénic Counter-Streaming Ions

Using the Walén relation $\mathbf{V}_{t,d} - \mathbf{V}_{t,u} = \pm\sqrt{\rho_u\varepsilon_u/\mu_0}(\mathbf{B}_{t,d}/\rho_d - \mathbf{B}_{t,u}/\rho_u)$ for switch-off slow shocks or rotational discontinuities ("t" for tangential, "u" for upstream and "d" for downstream), an outflow in the z-direction with Alfvénic velocity, $B_{z,u}/\sqrt{\mu_0\rho_u} \sim C_{Az} \equiv B_{z,a}/\sqrt{\mu_0 m_i n_a}$ is predicted [104]. The energy source of the

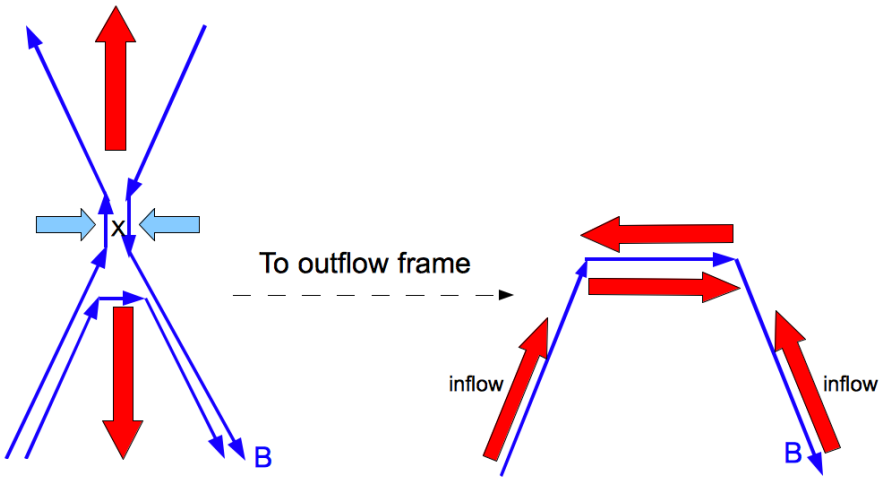

Figure 2.3: A cartoon showing the mechanism of forming counter-streaming ions

downstream outflow is the difference in the tangential component of the magnetic field across the discontinuity. If we jump to the outflow frame (the deHoffmann-Teller frame) as schematized in Fig. 2.3, there will be inflowing Alfvénic streaming ion beams from both discontinuities along the downstream magnetic field as observed by Gosling in the solar wind [36] and in kinetic reconnection simulations [56, 71, 43, 78, 28]. These counter-streaming ions cause an enhancement in the downstream parallel ion temperature ($T_{i\|} \sim O(m_i C_{Az}^2)$) and, therefore, the temperature anisotropy.

In the phase space of the 75° case at time $200/\Omega_{ci}$ (see Fig. 2.4) a signature of the counter-streaming beams is not obvious in the downstream region (since the ion distribution does not peak in the upper and lower parts of a single wave oscillation), perhaps because of the large-amplitude rotational wave. However, Alfvénic backstreaming ions in the z-direction (close to the parallel direction in the upstream

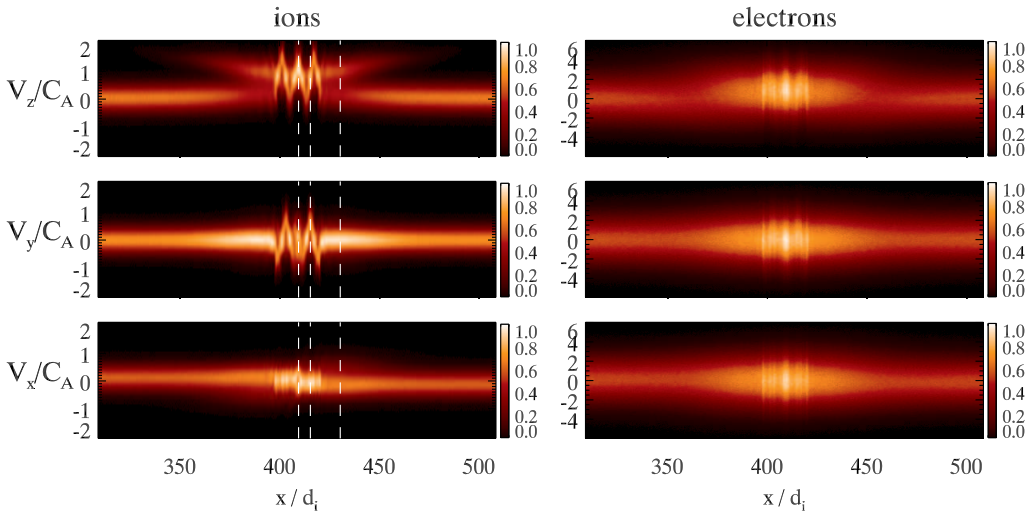

Figure 2.4: The phase space of the run with $\theta_{BN} = 75°$ (Run **f**) at time $200/\Omega_{ci}$. From top to bottom the left column shows the ion distribution in: $V_z - x$ space, where the backstreaming ions from the discontinuities are clearly seen; $V_y - x$ space; $V_x - x$ space. The right column is the electron distribution in $V_z - x$ space, $V_y - x$ space and $V_x - x$ space. The white dashed lines indicate the locations of the velocity distributions shown in Fig. 2.5. The color bar is normalized to the maximum value in each panel.

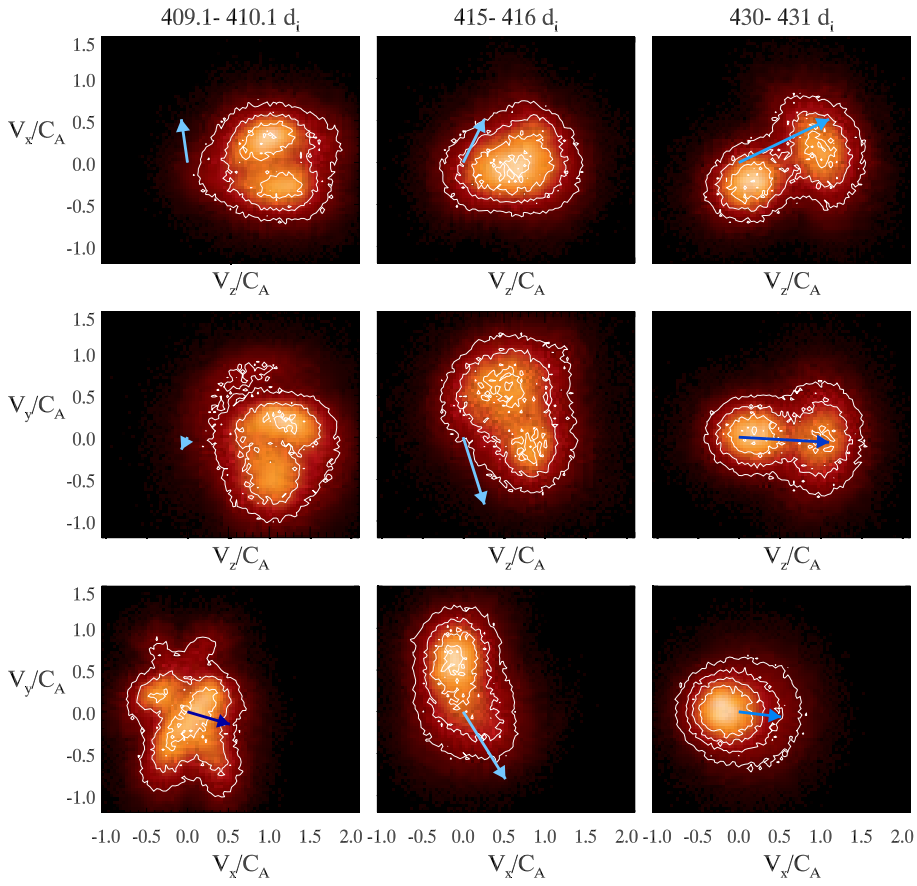

Figure 2.5: The ion velocity distributions measured at locations $409.1 - 410.1d_i$, $415 - 416d_i$ and $430 - 431d_i$ of Fig. 2.4 (the white dashed lines). From top to bottom are $V_z - V_x$, $V_z - V_y$ and $V_x - V_y$ distributions. The distributions are color coded and the white contours help identify different ion parcels. The local magnetic field is denoted by blue arrowed lines beginning at origin. The axis scales, when cut by a factor of 2, also measure the magnitude of the field. Ions that stream along the magnetic field are clearly seen at these locations.

region) are observed in Fig. 2.4. The time-of-flight effect (faster ions escape farther upstream) slowly broadens the transition region of slow shocks with time. The nearly uniform electron distribution in all directions is due to their high thermal conductivity and much lighter mass compared to the ions.

In Fig. 2.5, we show the ion distributions at the three locations demarcated by the white dashed lines in Fig. 2.4. Ions that stream along local magnetic fields (blue arrowed lines) are seen at these locations. Closer to the symmetry line, the drifting speed between these two ion parcels appears to be reduced, perhaps due to mixing by the rotational waves and some small-scale waves excited downstream. However, a complete thermalization at the symmetry line previously reported in 2-D low $\beta \lesssim 0.01$ hybrid simulations [19, 20] is not seen, a discrepancy perhaps explained by additional instabilities allowed by the lower β and their wider box ($l_z \sim 50 d_i$). The $V_x - V_y$ distribution at the symmetry line ($409.1 - 410.1 d_i$) is a complex non-Maxwellian, which indicates the ions undergo complicated meandering motions. The distributions of electrons at this time and locations appear Maxwellian without a clear signature of the backstreaming beam as reported before [22, 123], and are therefore not shown.

2.5 Temperature Anisotropy vs. Propagation Angles

In order to understand how the temperature anisotropy varies with other parameters, we perform runs with different upstream angles θ_{BN}. Fig. 2.6 documents the results of Runs **a**, **b**, **c**, **d**, **f** and **k**. From the first column, the downstream ε

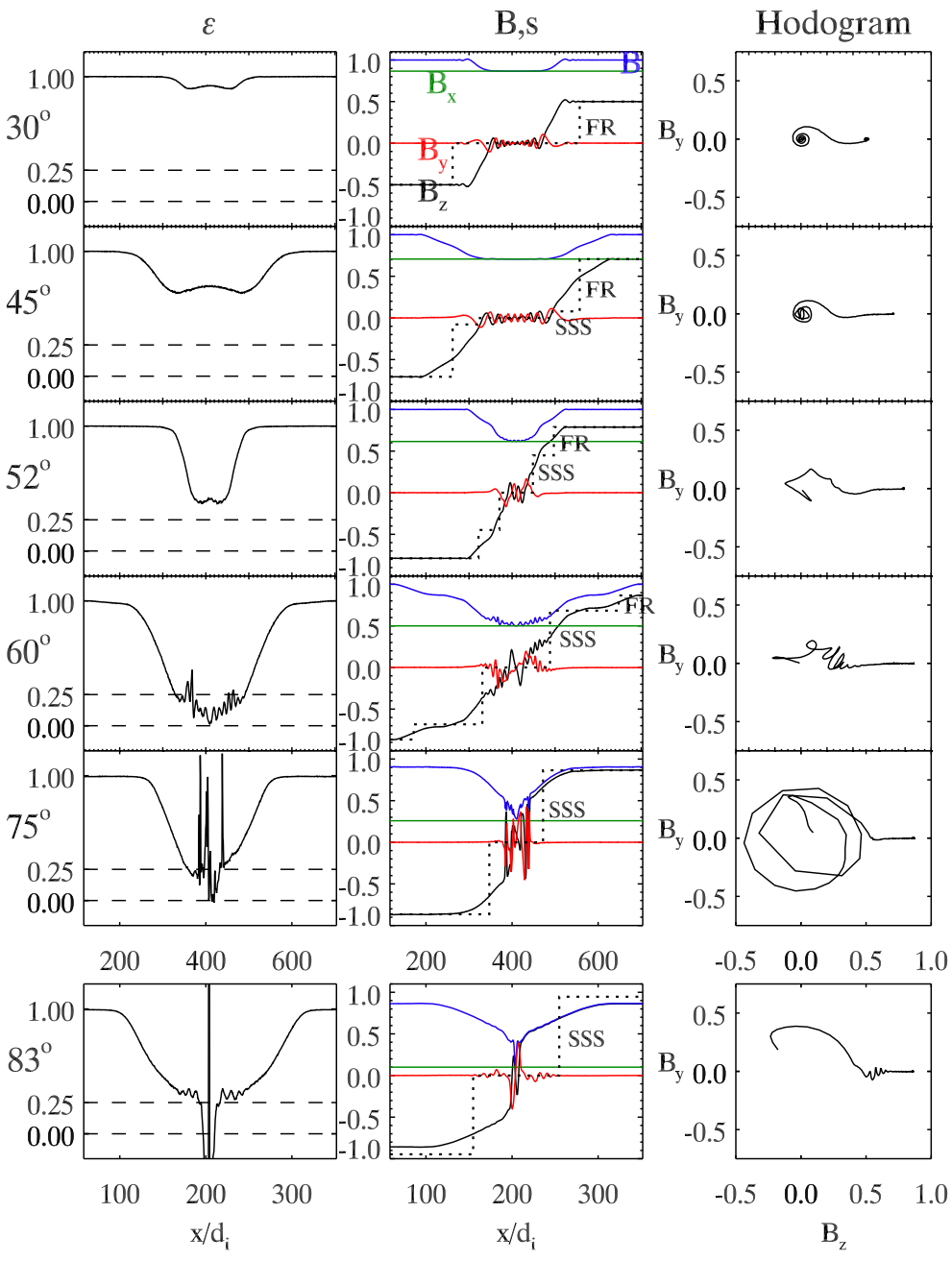

Figure 2.6: From top to bottom are runs with $\theta_{BN} = 30°$ (Run **a**) at $100/\Omega_{ci}$, 45° (Run **b**) at $200/\Omega_{ci}$, 52° (Run **c**) at $100/\Omega_{ci}$, 60° (Run **d**) at $250/\Omega_{ci}$, 75° (Run **f**) at $400/\Omega_{ci}$, and 83° (Run **k**) at $700/\Omega_{ci}$. The first column shows the temperature anisotropy, and the second column the magnetic field components as a function of x. The third column displays hodograms taken from the right half of the simulation domains. The dotted curves in the second column are the predicted magnitudes and positions of switch-off slow shocks (SSS) and fast rarefactions (FR) from isotropic MHD theory for B_z.

tends to lower values in the more oblique cases and the plasma becomes turbulent once ε is comparable to or lower than ~ 0.25. We can estimate at which θ_{BN} the downstream ε will drop below 0.25 as follows. In the cold plasma limit, the temperature anisotropy due to the Alfvénic counter-streaming ions at the symmetry line is (where $P_{\parallel} - P_{\perp} \sim n_a m_i C_{Az}^2$ and $|B| \sim B_{x,a}$),

$$\varepsilon_{down} \sim 0.25 \sim 1 - \frac{B_{z,a}^2}{B_{x,a}^2} \qquad \rightarrow \tan^2\theta_{BN,c} \sim 0.75 \qquad \rightarrow \theta_{BN,c} \sim 40^\circ \tag{2.2}$$

This argument qualitatively shows the tendency to develop stronger firehose-sense temperature anisotropies for higher obliquities. The difference between $\theta_{BN,c}$ and the observed value of 60° is probably due to the simplified assumptions, such as a cold streaming plasma.

In the second column of Fig. 2.6, the corresponding magnetic structures are shown. When the obliquity is large enough, especially when $\varepsilon < 0.25$, the downstream magnetic field rotates into the out-of-plane direction and becomes turbulent. Combined with the hodograms in the third column, we can deduce that the dominant downstream rotational waves are all left-handed (LH, counter-clockwise in our hodogram). When the wavelength of the primary LH wave is large, as in the $\theta_{BN} = 60^\circ$ case, its front part breaks into finer right-handed (RH) waves with scale $\sim 6d_i$. In the 75° case, the scale of the primary LH wave is already as small as $6d_i$, and so it is more stable than the 60° case, albeit still turbulent. (A 75° case with a wider initial current layer is discussed in the next section. It exhibits wave-generation phenomena similar to the 60° case). In the 83° case, we observe RH small-scale waves in front of the downstream primary LH wave.

For comparison, the dotted curves in the second column of Fig. 2.6 are the predicted B_z structure from MHD theory [65]. The overall predictions agree well for the oblique cases (see, for instance, the upstream B_z of the slow shocks in the 60° and 75° cases), although the reflected weak fast rarefactions from our boundary have caused a discrepancy in the slow shock upstream B_z for the 83° case. In less oblique cases, the intermediate and fast characteristic speeds approach one another just upstream of the switch-off slow shock according to MHD theory. Therefore there is no clear separation between the slow shocks upstream and the fast rarefactions, as can be seen in the simulations. We treat the place where the inflow speed V_x (not shown) starts to decrease as the upstream of the slow shocks, which corresponds to the beginning of the LH rotational wavetrains in the 30° and 45° cases. Their upstream will hence correspond to $B_z \sim 0.15$ and $B_z \sim 0.2$ respectively. Therefore the stable small amplitude rotational waves in the $\theta_{BN} = 30°$ and 45° cases are more similar to the conventional dispersive stationary downstream wavetrains, which immediately follow the slow shock upstream. (We note that the model in Lin and Lee [65] approximates the rarefactions by replacing the energy jump condition in the Rankine-Hugoniot relations by $[P\rho^{-\gamma}] = 0$, arguing that the entropy across a weak rarefaction does not change. This is only valid for weak rarefaction waves, but the overall tendency as the propagation angle becomes more parallel should be in the correct sense).

An interesting feature in the oblique cases is the coincidence between the start of the primary LH magnetic rotation and the location where the anisotropy parameter $\varepsilon \sim 0.25$. The anisotropy parameter seems to be locked to this critical

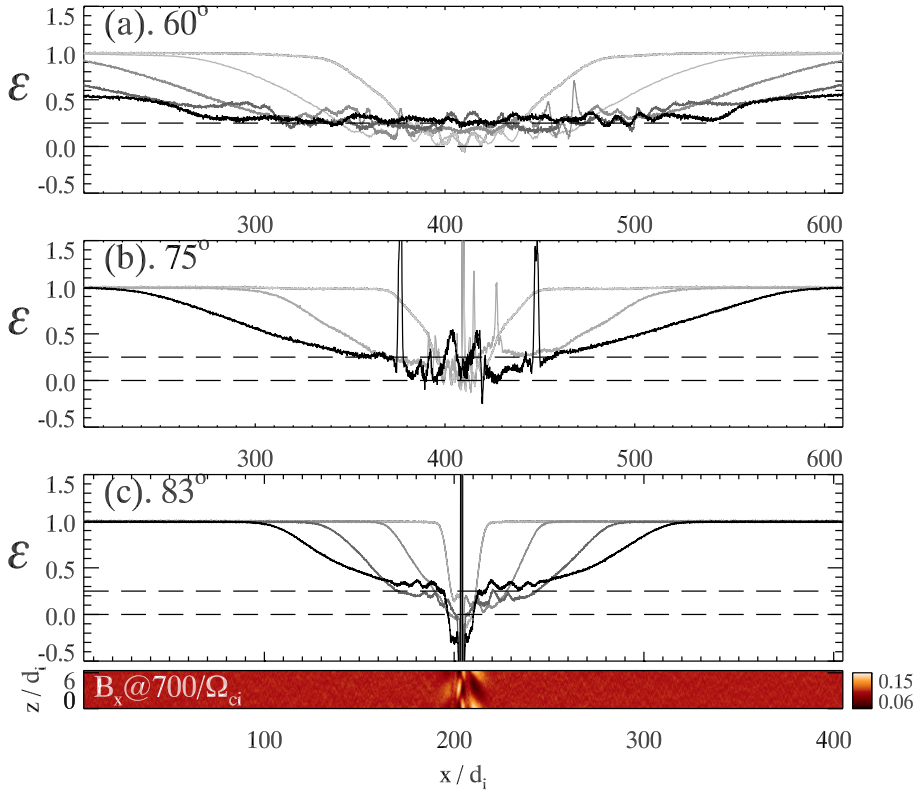

Figure 2.7: Evolution of ε for the case with $\theta_{BN} = 60°$(Run **d**) for equally spaced times between $100 - 500/\Omega_{ci}$ from lighter grey to darker grey in (a), the $\theta_{BN} = 75°$ case (Run **f**) for time $100 - 500/\Omega_{ci}$ in (b), and the $\theta_{BN} = 83°$ case (Run **k**) for time $100 - 700/\Omega_{ci}$ in (c). The bottom is a plot of B_x for the $\theta_{BN} = 83°$ case at time $700/\Omega_{ci}$ showing the 2-D turbulence that develops.

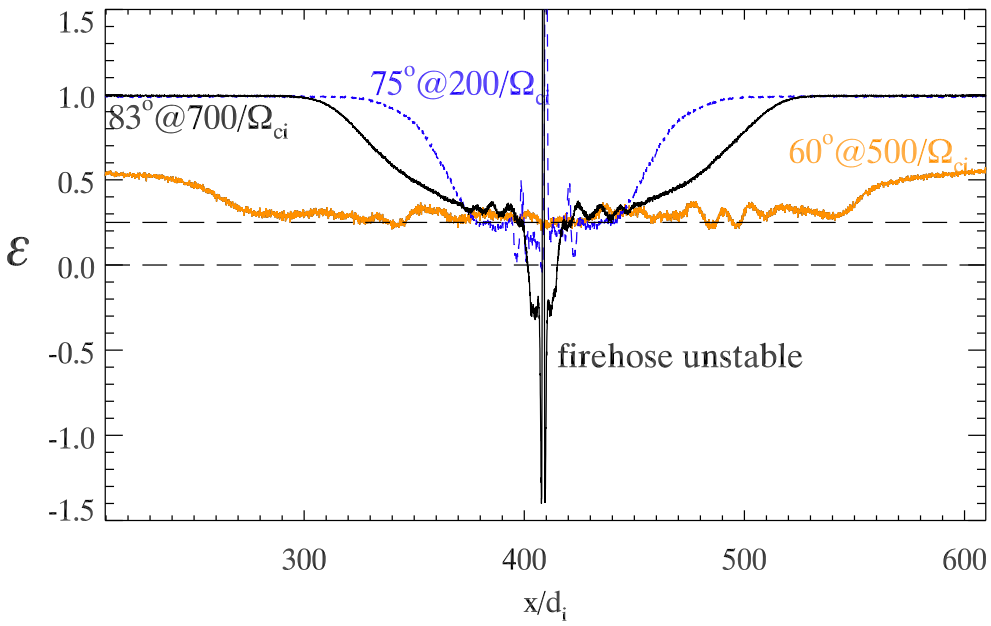

Figure 2.8: The ε distributions of runs $\theta_{BN} = 60°$ (Run **d**) at $500/\Omega_{ci}$, 75° (Run **f**) at $200/\Omega_{ci}$, 83° (Run **k**) at $700/\Omega_{ci}$. (The 83° case is shifted to the right by $204.8d_i$)

value for long periods of time, as is shown in Fig. 2.7. Moreover, this is also the location where turbulence develops. Given these coincidences the following questions naturally arise. If the rotational wave is really a normal dispersive wavetrain, why does it appear in the middle of the MHD predicted switch-off slow shocks? Why do the dispersive waves not start directly from the slow shock upstream? Is it not more similar to a new transition at $B_z \sim 0.3$ for $\theta_{BN} = 60°$, or $B_z \sim 0.5$ for $\theta_{BN} = 75°$ and 83°? What is special about $\varepsilon = 0.25$? (The importance of $\varepsilon \sim 0.25$ is shown for different obliquities in Fig. 2.8.) Are there other instabilities associated with this anisotropy value? Or is it due to the nonlinear structure of a system with a large temperature anisotropy that cannot be explained by ideal MHD?

We describe a possible theoretical explanation for why $\varepsilon \sim 0.25$ in the next

chapter. In short, $\varepsilon = 0.25$ represents a transition where the slow and intermediate mode speeds become degenerate. Unlike the conventional picture, the downstream rotational waves can not then be explained by slow dispersive waves, but instead take the form of rotational intermediate modes. The coplanar and non-coplanar part will later be identified as a single nonlinear wave, called a compound SS/RD wave.

2.6 The Downstream Turbulent Waves and Particle Scattering

The region downstream of oblique ($\theta_{BN} \geq 60°$) slow shocks is turbulent. High wavenumber waves are continually excited whenever the B_z component begins to rotate into the out-of-plane direction, as can be seen for the 60°, 75° and 83° cases in Fig. 2.6, and more clearly in the evolution of the B field for the case $75°, w_i = 10d_i$ (Run **g**) in Fig. 2.9. The downstream LH rotational parent waves break into $\lambda_x \sim 6d_i$-scale waves. The large oscillation in ε at later times is due to the small magnetic field magnitude near the symmetry line, where both B_z and B_y vanish. The particle scattering associated with these small-scale waves plays a role in counter-balancing the decrease in ε due to the streaming ions and keeping the temperature anisotropy around the value 0.25, as is seen in the time evolution of the oblique cases in Fig. 2.7.

In order to understand the downstream turbulent d_i-scale waves ($\sim 6d_i$), we tried to systematically pin down the possible drivers and energy sources via numerical experiments. We separately checked the temperature anisotropy, counterstreaming beams, and rotational parent waves (such as the larger LH wave in Fig. 2.9) to

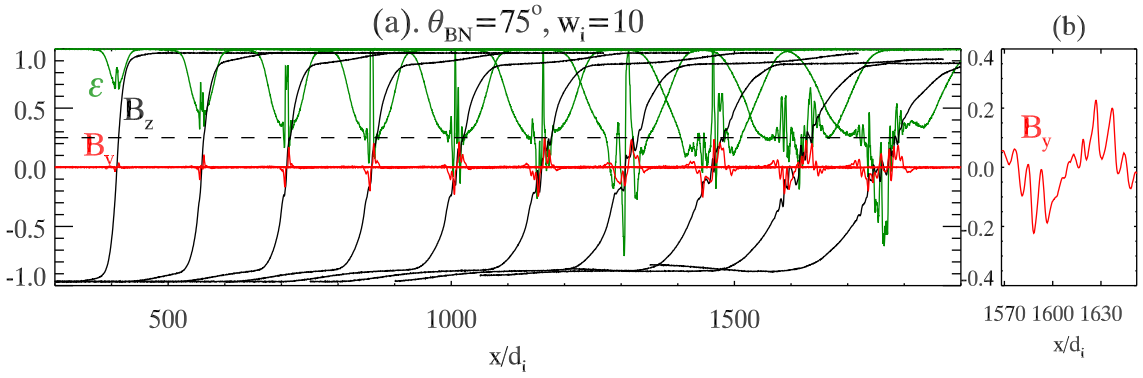

Figure 2.9: Panel (a): The evolution of ε, B_z and B_y for equally spaced times between $50 - 500/\Omega_{ci}$ (from left to right) in the $\theta_{BN} = 75°$, $w_i = 10d_i$ case (Run **g**). The downstream larger-scale rotational wave breaks into waves of wavelength $\sim 6d_i$. Panel (b): A blowup of the downstream B_y at time $450/\Omega_{ci}$.

determine which factors are responsible for generating the d_i-scale waves.

We carried out spatially homogeneous simulations with an initial wave structure of the following form:

$$B_z = B_{\rm cir}\cos(2\pi x/\lambda_p) + B_{z,\rm oblique}; \qquad B_y = P \times B_{\rm cir}\sin(2\pi x/\lambda_p) \tag{2.3}$$

When $B_{\rm cir} \neq 0$, there is a rotational field with $P = +1$ for LH, -1 for RH, and 0 for planar polarizations. The constant $B_{z,\rm oblique}$ controls the obliquity of this circularly polarized wave and provides a spatial modulation in the magnitude of the total magnetic field. The general expression for the initial ion distribution is

$$f_i \propto \exp\left(-\frac{m_i(v_\parallel - u)^2}{2T_{i\parallel}} - \frac{m_i v_\perp^2}{T_{i\perp}}\right) + \exp\left(-\frac{m_i(v_\parallel + u)^2}{2T_{i\parallel}} - \frac{m_i v_\perp^2}{T_{i\perp}}\right) \tag{2.4}$$

which has bi-Maxwellian counterstreaming beams for $u \neq 0$. Note that $T_{i\parallel,\rm eff} = T_{i\parallel} + m_i u^2$, so both $u \neq 0$ and $T_{i\parallel} \neq T_{i\perp}$ can contribute to the temperature anisotropy ε. The initial plasma density varies so as to ensure a constant value of $P_\perp + B^2/(2\mu_0)$.

Since the small-scale waves that interest us do not induce variation in the z-direction, they are intrinsically 1-D waves along the x-direction. The common parameters used here are a domain size of $1.6 \times 51.2d_i$, with grid 64×2048, $\lambda_p = 51.2d_i$, uniform $T_{i,e\perp} = T_{e\parallel} = 0.15$, $B_x = 0.25$ and $n_{i,e} = 1.5$ at $x = 0$. The resultant β in the following case is always > 1. These parameters are meant to represent those observed in the downstream of the 75° case.

Table 2.2: Overview of runs

Run	$B_{\rm cir}$	Polar. (P)	$B_{z,\rm oblique}$	$T_{i\parallel}$	Beams (u)	$\rightarrow$[1] $T_{i\parallel,\rm eff}$	$\rightarrow \varepsilon$	$\rightarrow$ 1-D waves[2]
1	0.25	+1	0.25	0.15	0.5	0.4	-0.2 $\sim$ -7	$\surd$
2	0.25	+1	0.25	0.4	0	0.4	-0.2 $\sim$ -7	$\surd$
3	0.25	+1	0	0.15	0.5	0.4	-2	x
4	0.25	+1	0	0.4	0	0.4	-2	x
5	0.25	+1	0.25	0.15	0	0.15	1	$\surd$
6	0.25	0	0.25	0.15	0	0.15	1	x

[1] "$\rightarrow$" means "resulting in".
[2] d_i-scale waves generated within time $100/\Omega_{ci}$.

Run **1** of Table 2.2 is a representative example of the downstream structure seen in the Riemann simulations. The initial obliquely propagating LH polarized waves with Alfvénic counter-streaming ions along the local magnetic field break into $\sim 6d_i$ small-scale waves, as shown in Fig. 2.10(a). In Run **2**, we replace the counter-streaming ions with a bi-Maxwellian plasma with the same effective parallel temperature, therefore the same temperature anisotropy ε, and find similar wave-generation phenomena. In Runs **3** and **4**, we remove the obliquity ($B_{z,\rm oblique}$) from Runs **1** and **2** respectively. No d_i-scale waves are excited within a time of $100/\Omega_{ci}$ in Run **3**, as is shown in Fig. 2.10(b). This indicates the importance of spatial

modulation for the development of the turbulence.

In Run **5**, we replace the beams or anisotropic plasma of Runs **1** and **2**, respectively, with a Maxwellian isotropic plasma. Waves with scale $\sim 6d_i$ are excited and are shown in Fig. 2.10(c). However, if we further remove the initial out-of-plane magnetic field of the parent wave (Run **6**), no small-scale waves appear; see Fig. 2.10(d). This indicates that a necessary condition for producing these small-scale waves is the existence of circularly polarized parent waves. From this suite of runs we conclude that the presence of a spatially modulated rotational wave is the major driver of d_i-scale coherent waves seen downstream of the shock (see Fig. 2.9(b)). Although not shown, we see similar behvior for RH ($P = -1$) parent waves.

A non-modulated, constant-amplitude, circularly polarized Alfvén wave is a known stationary solution of the MHD equations. Although it is subject to a long-wavelength modulational instability under some conditions [77], simulations show that it is also stable in a collisionless plasma. Spangler & Plapp [105] explored a similar wave-generation phenomena, as well as the formation of solitary waves with a system with initial conditions similar to our Run **5**. He cast his system in terms of the Derivative-Nonlinear-Schrödinger-Equations, which are simplified MHD equations that possess the MHD nonlinearity and dispersion terms. This suggests the importance of both the nonlinearity and the Hall dispersion term for these d_i-scale waves. We also note that the time of onset of these waves is proportional to λ_p and inversely proportional to the amplitude $B_{\rm cir}$, which are closely related to the steepening time scale of finite amplitude waves, $T_s \sim (\tau_{\rm wave}/2\pi)(B/\Delta B)$, with $\tau_{\rm wave} \propto \lambda_p$ (the gradient scale of the finite amplitude wave) [5]. Although a firehose-

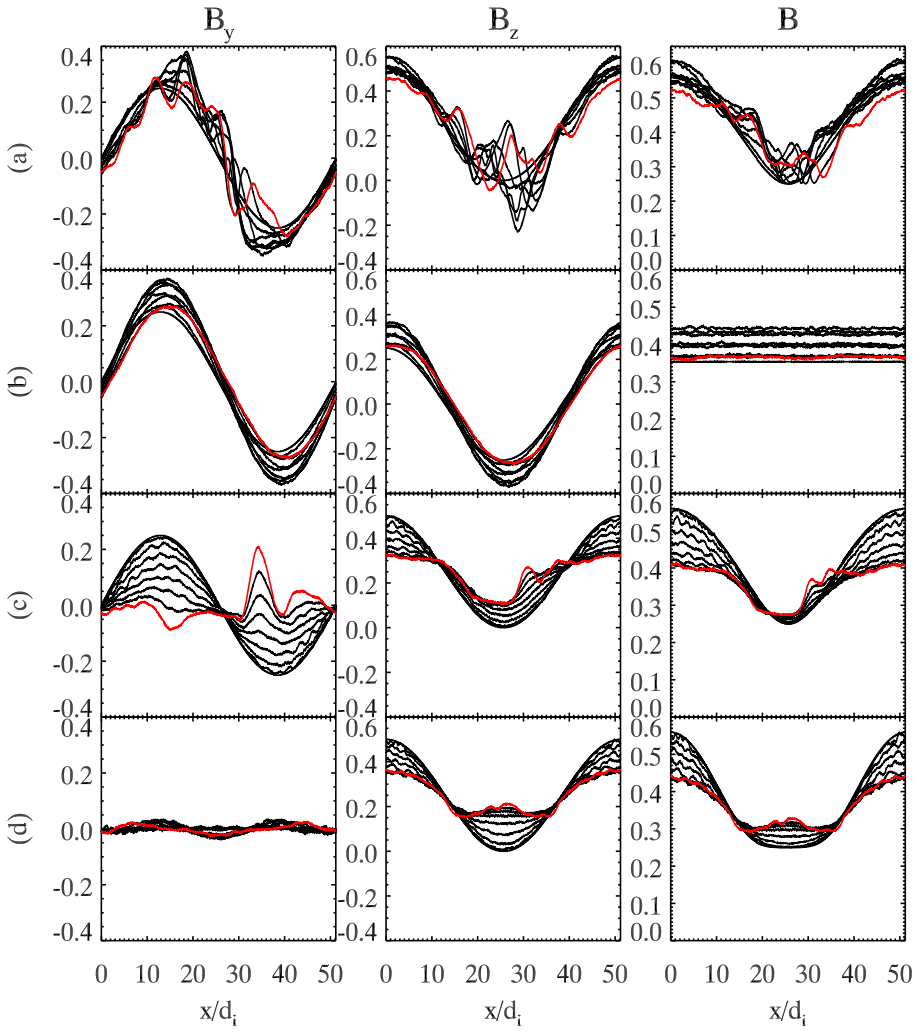

Figure 2.10: The evolution of B_y, B_z and B for equally spaced times between $0 - 100/\Omega_{ci}$. The red curve indicates the time $100/\Omega_{ci}$. Panel (a): Run **1** with both initial streaming ions and modulated rotational parent wave. Panel (b): The same as panel (a) without the initial spatial modulation (Run **3**). Panel (c): The same as panel (a) without initial beams (Run **5**). Panel (d): The same as panel (c) without initial polarization (Run **6**).

sense temperature anisotropy ($\varepsilon < 1$) would weaken the nonlinearity, the spatial variation of ε enhances the nonlinearity, as will be shown in the next chapter [68].

Runs **3** and **4** suggest that temperature anisotropy and Alfvénic beams are not, by themselves, sufficient for generating the small-scale waves seen in the downstream region. The time scale for these parent rotational waves to break into smaller-scale waves is faster than the beam driven EMIIC instability, which excites oblique AIC waves in hybrid models [117], or oblique KAWs in PIC models [124]. Perhaps the higher β in our simulations (*e.g.,* upstream $\beta_i = \beta_e = 0.2$) has slowed or suppressed the development of the EMIIC instability [21]. We also note that the KAWs in Yin et al. [123] are generated upstream of the rotational front where the beam effect is stronger ($T_\parallel$ peaks), while our small-scale waves coexist with the rotational part as clearly seen in Fig. 2.9, where the local β's of both ion parcels are higher. This further suggests a mechanism other than the EMIIC instability. In addition, we have not observed clear perpendicular heating in both ion parcels [124, 19, 20] and parallel heating in electrons [124, 123] by oblique KAWs (if present), since these heating effects could also be suppressed by higher β. As for the growth rate of the anisotropy driven firehose instability, $\gamma^2 \sim -\varepsilon k^2 C_A^2$ [23]. The unstable wavelength that interests us is $k \sim 1$, and anisotropy $\varepsilon = -2$ (in Run **3**, **4**), then a small growth rate of the firehose instability is due to a small C_A based on the local magnetic field $B_x \sim 0.25$. However, these beam/anisotropy-driven waves are still potential players in the downstream turbulence at late time. By comparing Fig. 2.10(a) to (c), we see that the interplay of the steepening process and the free-streaming beams makes the wave more turbulent. In Fig. 2.11, the ion temperature anisotropy $T_{i\parallel} - T_{i\perp}$ of

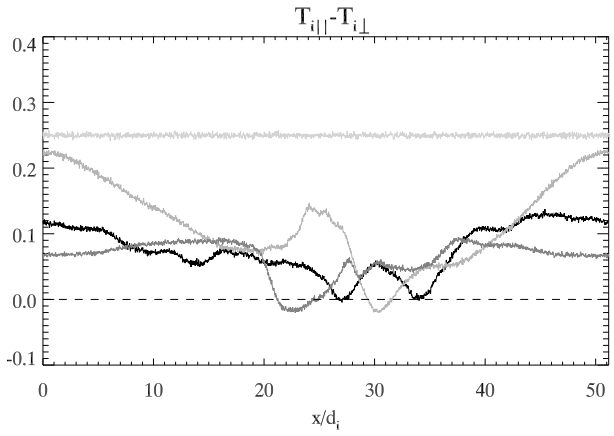

Figure 2.11: The evolution of $T_{i\|} - T_{i\perp}$ for equally spaced times between $0-100/\Omega_{ci}$(from lighter grey to darker grey) of Run **1** (Fig. 2.10(a)). The temperature anisotropy of the ions is reduced, which indicates particle scattering is taking place.

Run **1** (which corresponds to Fig. 2.10(a)) decreases. This confirms the ability of these smaller-scale dispersive waves to scatter ions.

The polarization of a linear wave can be determined by the phase between the tangential magnetic field variations δB_z and δB_y. In the fluid model $i\delta B_z/\delta B_y = (C_I^2 - (\omega/k)^2)/(\omega d_i C_A \cos(\theta_{BN}))$ [112]. A wave has a LH polarization when $(\omega/k)^2 < C_I^2$, and RH otherwise. As observed in our oblique shock simulations (discussed in Sec. 2.5), the small-scale waves at the upstream of the rotational front are mostly RH, while the downstream waves are mostly LH. This suggests that the primary rotational front propagates at the local intermediate speed (as also measured in the simulations). We do not address which modes are responsible for these fine-scale waves here, since the polarization of the linear mode in kinetic theory is very complicated. Both temperature anisotropy and high plasma β play roles in changing the linear wave properties [57]. A better understanding of the nature of these turbulent

waves could be gained by comparing the downstream spectrum to the dispersion relation calculated from linear Vlasov theory. With a larger l_z and very oblique propagation angle, as in the 83° case, 2-D turbulence with $\lambda_z \sim 6d_i$ is excited around the firehose-unstable region. Its signature is most clear in B_x, as can be seen in the bottom plot of Fig. 2.7. A similar mechanism is postulated to excite 2-D turbulence in the firehose-unstable region seen in the reconnection simulation of Fig. 1.11(c) (and, perhaps, the 2-D turbulence previously reported [98]). This 2-D turbulence could be driven by temperature anisotropy (firehose-like) or by the sharp front of the primary rotational wave. It does not appear to be similar to the parallel AIC waves driven by the AIC-like instability observed in Cremer & Scholer [19, 20], since no significant perpendicular heating in both ion parcels is seen in the simulation of Fig. 1.11.

2.7 Summary and Discussion

We have studied the temperature anisotropy distribution across slow shocks with different obliquities in PIC simulations. An abnormal transition and an anisotropy $\varepsilon = 0.25$ locking phenomena downstream of the MHD predicted switch-off slow shocks is documented. The Alfvénic counter-streaming ions serve as the driver for decreasing ε (increasing the firehose-sense temperature anisotropy) in the downstream region, while downstream d_i-scale turbulent waves scatter particles and raise ε. This dynamical balance makes the downstream ε plateau at a value of $\varepsilon = 0.25$ and not the marginal firehose criterion $\varepsilon = 0$. The theoretical significance of $\varepsilon = 0.25$

will be addressed in the next chapter. By means of PIC numerical experiments we show that the turbulent d_i-scale waves are radiated from a spatially modulated rotational parent wave .

The Riemann problem for the $\theta_{BN} = 83^\circ$ case is closely related to that of reconnection exhausts with normalized reconnection rates of 0.1. The very center is a firehose-unstable region where a B_x variation is observed, as in the reconnection simulations discussed in Fig. 1.11(c). Although we cannot confidently identify the 0.25 plateau in present PIC reconnection simulations (since the spatial extension in the normal direction ($\hat{\mathbf{x}}$), is $\sim 10d_i$; see Fig. 1.11(d)), we expect to see the signature of a $\varepsilon = 0.25$ plateau outside the firehose unstable region in very large kinetic anti-parallel reconnection simulations and in-situ satellite observations of anti-parallel magnetic reconnection outflows.

In reconnection with lower upstream β ($\lesssim 0.1$), it has been suggested that backstreaming ions drive the electromagnetic ion-ion cyclotron instability, which excites oblique kinetic-Alfvén waves (or Alfvén/ion cyclotron waves in a hybrid model) that propagate to the upstream region. Oblique propagating KAWs then heat ions in the perpendicular direction while heating electrons in the parallel direction [116, 117, 124, 123]. The resultant higher perpendicular temperature of each ion parcel (*i.e.,* the backstreaming ions and inflowing ions) can further drive an anisotropic (AIC-like) instability, which excites parallel propagating AIC waves in the upstream region [19, 20]. It could be of interest to investigate how these processes affect the ε distribution and the critical $\varepsilon = 0.25$ plateau observed here.

Chapter 3

Anisotropic Fluid Theory

3.1 Overview

The structures of shock transitions in isotropic MHD have been intensively studied, including the existence of intermediate shocks (IS) ([12, 119, 52, 120] and references therein), the occurrence of dispersive wavetrains [17, 40, 121], and the nested subshocks inside shocks predicted by the Rankine-Hugoniot jump conditions [51, 69]. In a collisionless plasma, the effects of temperature anisotropy need to be considered, which can be done for linear waves with the Chew-Goldberger-Low (CGL) framework [1, 41]. Hau and Sonnerup [41] have pointed out the abnormal properties of the linear slow mode under the influence of a firehose-sense ($P_\parallel > P_\perp$) pressure anisotropy, including a faster phase speed compared to the intermediate mode, a fast-mode-like positive correlation between magnetic field and density, and the steepening of the slow expansion wave. In kinetic theory both anisotropy and high β can greatly alter the linear mode behavior [57, 50]. The anisotropic Rankine-Hugoniot jump conditions have been explored while taking the downstream anisotropy as a free parameter [14, 45, 46, 47]. Hudson [46] calculated the possible anisotropy jumps across an anisotropic rotational discontinuity, while Karimabadi *et al.* [50] noticed the existence of a slow shock whose upstream and downstream are both super-intermediate. But, a comprehensive nonlinear theory

describing the coupling between slow and intermediate shocks under the influence of temperature anisotropy has not yet been presented.

In Petschek's description of magnetic reconnection, the reconnection exhaust is bounded by a pair of back-to-back standing switch-off slow shocks. Particle-in-cell (PIC) simulations of such shocks [67, 123] exhibit large downstream temperature anisotropies. In chapter 2 we show that when the parameter $\varepsilon = 1 - \mu_0(P_\parallel - P_\perp)/B^2 = 0.25$, the behavior of the coplanar shock undergoes a transition to non-coplanar rotation. This firehose-sense temperature anisotropy slows the linear intermediate mode and speeds up the linear slow mode enough so that, at some point, their relative velocities can be reversed [1, 41]. This reversal is reflected in the structure of the Sagdeev potential (also called the pseudo-potential) [93], which characterizes the nonlinearity of the system. In this chapter a simplified theoretical model is developed to explore the effect of temperature anisotropy on the structure of the Sagdeev potential and to provide an explanation for the extra transition inside the switch-off slow shock (SSS) predicted by isotropic MHD. The theory suggests that in PIC simulations a compound slow shock (SS)/ rotational discontinuity (RD) is formed instead of a switch-off slow shock. This work may help to explain satellite observations of compound SS/RD waves [115, 114], anomalous slow shocks [112] and the trapping of an RD by the internal temperature anisotropy of a slow shock in hybrid simulations [59].

In Sec. 3.2 of this chapter we introduce our model equations for studying the nonlinear coupling of slow and intermediate waves under the influence of a temperature anisotropy. In Sec. 3.3 we calculate the speeds and the eigenmodes of slow and

intermediate waves. Sec. 3.4 points out the existence of extra degeneracy points between slow and intermediate modes introduced by the temperature anisotropy, and comments on the consequences (in the context of the Riemann problem) of having the slow wave faster than the intermediate wave. In Sec. 3.5 we introduce a simple energy closure. In Sec. 3.6.1 we calculate the pseudo-potential of stationary solutions, and apply the equal-area rule to identify the existence of compound SS/RD waves and compound SS/IS waves. In Sec. 3.6.2 we demonstrate the significance of $\varepsilon = 0.25$ as being the lower bound of the SS to RD transition in compound SS/RD waves. In Sec. 3.7 we discuss the time-dependent dynamics that help keep $\varepsilon = 0.25$. In Sec. 3.8 we provide more evidence from PIC simulations to support the existence of compound SS/RD waves at the boundaries of reconnection exhausts. In Sec. 3.9, we summarize the results and point out the relation between compound SS/RD waves and anisotropic rotational discontinuities [46].

3.2 The Anisotropic Derivative Nonlinear Schrödinger-Burgers Equation

Instead of analyzing the anisotropic MHD equations, which have seven characteristics (waves), we simplify the system into a model equation that possesses only two characteristics. This model equation will be ideal for demonstrating the underlying coupling between the nonlinear slow and intermediate modes. Beginning with the anisotropic MHD equations [14], we follow the procedure of Kennel *et al.* [52, 53] to derive the Anisotropic Derivative Nonlinear Schrödinger-Burgers equation

(ADNLSB) (see Appendix A.1 for details),

$$\partial_\tau \mathbf{b}_t + \partial_\eta[\alpha \mathbf{b}_t(b_t^2 - b_{t0}^2) + \Omega \mathbf{b}_t(\varepsilon - \varepsilon_0)] = \partial_\eta(R\partial_\eta \mathbf{b}_t) - \frac{1}{2\sqrt{\varepsilon_0}} d_i \partial_\eta^2(\hat{\mathbf{x}} \times \mathbf{b}_t) \qquad (3.1)$$

This equation describes waves that propagate in the x-direction in the upstream intermediate speed frame. In this frame $\eta \equiv x' - \sqrt{\varepsilon_0} C_{An} t$ is the spatial coordinate with $C_{An}^2 \equiv B_x^2/(\mu_0 \rho_0)$, and $\tau \equiv \sqrt{\varepsilon_0} C_{An} t$ is the time used to measure the slow variations (such as steepening processes). $\mathbf{b}_t = \mathbf{B}_t/B_x$, where the subscript "$t$" represents the component tangential to the wave-vector and here will be in the y-z plane. The anisotropy parameter $\varepsilon = 1 - \mu_0(P_\parallel - P_\perp)/B^2$. The subscript "0" denotes the upstream parameters. The right hand side term proportional to the ion inertial length, $d_i \equiv \sqrt{m_i/(\mu_0 n e^2)}$, represents dispersion (which can be viewed as the spreading tendency of Fourier decomposed waves of different wavenumbers), while the term containing R describes dissipation from magnetic resistivity. Here R is a constant. The terms proportional to α and Ω are the nonlinearities of this wave equation, where

$$\alpha \equiv \frac{(4\varepsilon_0 - 1)C_{An}^2}{12[(\varepsilon_0 - A)C_{An}^2 - C_S^2]} \qquad (3.2)$$

$$\Omega \equiv \frac{(b_{t0}^2 - 2)C_{An}^2}{6[(\varepsilon_0 - A)C_{An}^2 - C_S^2]} + \frac{1}{2\varepsilon_0} \qquad (3.3)$$

and

$$A \equiv \frac{4}{9}(1 - \varepsilon_0)(1 + b_{t0}^2) \qquad (3.4)$$

Here $C_S^2 \equiv (5/3)P_0/\rho_0$. Since we are studying reconnection exhausts, θ_0 (the angle between the upstream magnetic field and $\hat{\mathbf{x}}$) is typically large ($\sim 80°$). Therefore $\beta_n \equiv \beta/\cos^2\theta_0 = C_S^2/C_{An}^2 \gg 1$, and $(\varepsilon_0 - A)C_{An}^2 - C_S^2 \sim -C_S^2 < 0$. Hence

this equation describes only the slow and intermediate modes [52] (this is shown explicitly in the next section). This fact relates to the degeneracy properties of ideal MHD for parallel propagating waves, namely that the fast and intermediate modes degenerate in $\beta < 1$ plasmas, while the slow and intermediate mode degenerate in $\beta > 1$ plasmas. Finally, we note that Eq. (3.1) is applicable in the weak nonlinearity limit.

3.3 The Conservative Form- Wave Propagation

In order to explore the structure of the reconnection exhaust, a comprehensive understanding of how waves connect to each other across a transition is required. This is called a Riemann problem. Neglecting the source terms on the right hand side (RHS), the left hand side (LHS) of Eq. (3.1) is a hyperbolic equation in conservative form.

Letting $\varepsilon - \varepsilon_0 \equiv \delta\varepsilon(b_z, b_y)$, and $\mathbf{b}_{t0} = b_{z0}\hat{\mathbf{z}}$, we obtain,

$$\partial_\tau \mathbf{q} + \partial_\eta \mathbf{f}(\mathbf{q}) = 0, \tag{3.5}$$

with

$$\mathbf{q} \equiv \begin{bmatrix} q_1 \\ \\ q_2 \end{bmatrix} = \begin{bmatrix} b_z \\ \\ b_y \end{bmatrix}, \qquad \mathbf{f} \equiv \begin{bmatrix} f_1 \\ \\ f_2 \end{bmatrix} = \begin{bmatrix} \alpha b_z(b_z^2 + b_y^2 - b_{z0}^2) + \Omega b_z \delta\varepsilon \\ \\ \alpha b_y(b_z^2 + b_y^2 - b_{z0}^2) + \Omega b_y \delta\varepsilon \end{bmatrix}. \tag{3.6}$$

We can obtain the characteristics (waves) of this equation by analyzing its flux function, $\mathbf{f}$. Its Jacobian is

$$\partial_q f = \begin{bmatrix} \alpha(3b_z^2 + b_y^2 - b_{z0}^2) + \Omega(\delta\varepsilon + b_z\delta\varepsilon_{b_z}) & 2\alpha b_z b_y + \Omega b_z \delta\varepsilon_{b_y} \\ \\ 2\alpha b_z b_y + \Omega b_y \delta\varepsilon_{b_z} & \alpha(3b_y^2 + b_z^2 - b_{z0}^2 + \Omega(\delta\varepsilon + b_y\delta\varepsilon_{b_y})) \end{bmatrix}, \tag{3.7}$$

where $\delta\varepsilon_{b_z} \equiv \partial(\delta\varepsilon)/\partial b_z$, $\delta\varepsilon_{b_y} \equiv \partial(\delta\varepsilon)/\partial b_y$. One eigenvalue (also called the characteristic speed) is

$$\lambda_{SL} = \alpha(3b_t^2 - b_{t0}^2) + \Omega(\delta\varepsilon + b_z\delta\varepsilon_{b_z} + b_y\delta\varepsilon_{b_y}) \tag{3.8}$$

with eigenvector

$$\mathbf{r}_{SL} = \frac{1}{b_t}\begin{bmatrix} b_z \\ \\ b_y \end{bmatrix}. \tag{3.9}$$

In isotropic ideal MHD, where the $(\varepsilon - \varepsilon_0)$ term is dropped, the eigenvalue in the infinitesimal limit ($b_t \to b_{t0}$) is $\lambda_{SL} = 2\alpha b_{t0}^2$, which is the phase speed of the linear slow mode in the intermediate mode frame [52]. The subscript "SL" means the slow mode. The eigenvector indicates that slow mode is coplanar (*i.e.,* in the radial direction in $b_z - b_y$ space).

The other mode has eigenvalue

$$\lambda_I = \alpha(b_t^2 - b_{t0}^2) + \Omega\delta\varepsilon \tag{3.10}$$

and eigenvector

$$\mathbf{r}_I \propto \begin{bmatrix} \alpha b_y + \Omega\delta\varepsilon_{b_y}/2 \\ \\ -\alpha b_z - \Omega\delta\varepsilon_{b_z}/2 \end{bmatrix}. \tag{3.11}$$

In isotropic ideal MHD, where the $(\varepsilon - \varepsilon_0)$ term is dropped, the eigenvalue in the infinitesimal limit is $\lambda_I = 0$, which is the phase speed of the linear intermediate mode in the intermediate mode frame [52]. The subscript "I" means the intermediate mode. The eigenvector indicates that this intermediate mode is non-coplanar (*i.e.,* in a non-radial direction).

It can be shown that $\nabla_{\mathbf{q}}\lambda_I(\mathbf{q}) \cdot \mathbf{r}_I(\mathbf{q}) = 0$ for all $\mathbf{q}$. This means that along the eigen-direction of the intermediate mode the characteristic speed is constant,

and thus the mode exhibits no steepening or spreading, just as is the case for its counterpart in isotropic MHD. (This behavior is also confirmed by the anisotropic MHD simple wave calculation; see Appendix A.2). Therefore the intermediate mode is termed "linearly degenerate". If we are looking for a transition in the $-\mathbf{r}_{SL}$ direction (toward $b_t = 0$), then the portion of the slow mode with $\nabla_{\mathbf{q}}\lambda_{SL}(\mathbf{q}) \cdot \mathbf{r}_{SL}(\mathbf{q}) < 0$ will steepen into a slow shock. When λ_{SL} at the downstream of a transition is larger than that at the upstream, the downstream wave will catch up with the upstream wave and thus steepen.

3.4 A New Degeneracy Point due to the Temperature Anisotropy

In the Riemann problem for our two mode system, we seek to determine the middle state $\mathbf{q}_m$ that connects the faster "2-wave" from a given state $\mathbf{q}_r$, to the slower "1-wave" from a given state $\mathbf{q}_l$ (see Fig. 3.1 (a); the subscripts "r" and "l" mean right and left respectively). In order to determine the path that connects $\mathbf{q}_r$ to $\mathbf{q}_l$ in the state space ($b_z - b_y$ space, in this case), the Hugoniot locus that connects $\mathbf{q}_l$ or $\mathbf{q}_r$ to a possible asymptotic state by shock waves needs to be calculated, as do the integral curves for possible rarefaction waves (see, for example, [61]). The Hugoniot locus in state space is a curve formed by allowing one of the parameters in the standard Rankine-Hugoniot jump condition to vary. The integral curve is formed by following the eigenvector from a given state in state space.

In order to proceed we further assume a gyrotropic energy closure, $\delta\varepsilon = \delta\varepsilon(b_t)$,

which allows us to write

$$\mathbf{r}_{SL} = \frac{1}{b_t}\begin{bmatrix} b_z \\ \\ b_y \end{bmatrix} \qquad \mathbf{r}_I = \frac{1}{b_t}\begin{bmatrix} b_y \\ \\ -b_z \end{bmatrix} \qquad \lambda_{SL} - \lambda_I = 2\alpha b_t^2 + \Omega\delta\varepsilon_{b_t} b_t \tag{3.12}$$

The Hugoniot locus and integral curves of the intermediate mode are identical in our system. This is also the case for the slow mode (we perform the calculation in Appendix A.3). For a given state, $\mathbf{q}_r = \mathbf{b}_{t0} = (b_{z0}, 0)$, the Hugoniot locus and integral curve of the slow mode are

$$b_y = 0 \tag{3.13}$$

which is in the radial direction in state space. This direction implies that the slow shock is coplanar, even in the presence of temperature anisotropy, just as is the case for its counterpart in full anisotropic MHD [14]. In the isotropic case, this curve forms a slow shock if the path is toward the origin, and a slow rarefaction if the path is away from the origin. For the intermediate mode, the Hugoniot locus and integral curve are

$$b_y^2 = b_{z0}^2 - b_z^2 \tag{3.14}$$

which is a circle in state space. Note that even though we can calculate the Hugoniot locus and integral curve for the intermediate mode, the solution is the same as for a finite amplitude intermediate mode that does not steepen into a shock or spread into a rarefaction.

The state $\mathbf{q}_r$ can connect to $\mathbf{q}_l = (0, 0)$ by following the Hugoniot locus of a slow mode that starts from $\mathbf{q}_r$, as shown in Fig. 3.1(b). In isotropic MHD this forms a switch-off slow shock. However, a strong enough temperature anisotropy introduces

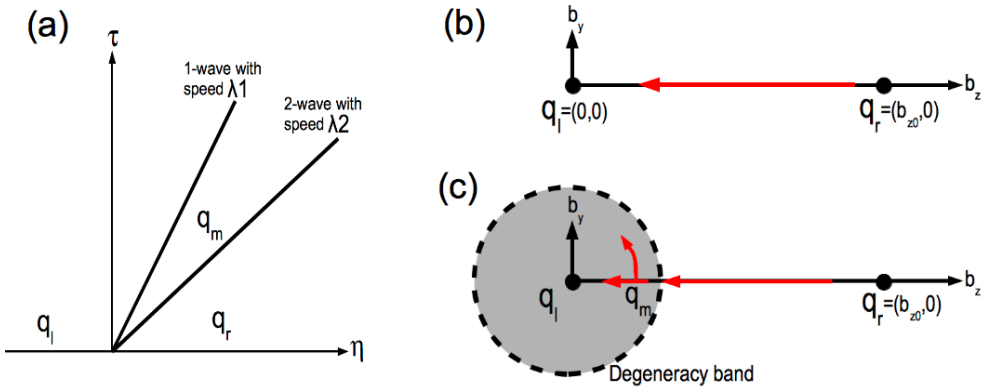

Figure 3.1: Panel (a): An initial discontinuity between $\mathbf{q}_r$ and $\mathbf{q}_l$ results in two waves, the "1-wave" and "2-wave", that propagate in the η direction along time τ. The middle state $\mathbf{q}_m$ needs to be determined; Panel (b): The state space plot in the (b_z, b_y) plane. The value $\mathbf{q}_r = (b_{z0}, 0)$ is chosen since there is no out-of-plane B_y upstream of the slow shocks in chapter 2. $\mathbf{q}_r$ straightly connects to $\mathbf{q}_l$ and forms a switch-off slow shock; Panel (c): In order to connect $\mathbf{q}_r$ to $\mathbf{q}_l$, it is necessary to cross the degeneracy band into the reversal region, which could cause the path to rotate at $\mathbf{q}_m$.

new degeneracy points (which occur where $\lambda_{SL} - \lambda_I = 0$) when $2\alpha b_t + \Omega\delta\varepsilon_{b_t} = 0$, other than the traditional degeneracy point at $b_t = 0$. These points form a band circling the origin as shown in Fig. 3.1(c). Inside the band, the intermediate mode is slower than the slow mode. Physically, this implies that a rotational intermediate mode can arise downstream of a slow mode, something which is not allowed in a Riemann problem in isotropic MHD. This effect is realized when the path along the Hugoniot locus ($-\mathbf{r}_{SL}$ direction) of the slow mode from $\mathbf{q}_r$ switches to the solution of the intermediate mode (circular direction) somewhere ($\mathbf{q}_m$) inside the degeneracy band.

This behavior can explain the morphological differences between the shock simulations in the cases $\theta_{BN} = 30°, 45°$ and those for $\theta_{BN} = 60°, 75°, 83°$ of Fig. 2.6. The latter has an extra transition to the rotational direction that is similar to the path in Fig. 3.1(c). We now look for a similar effect in state space and a way of determining $\mathbf{q}_m$ in a more detailed analytical model.

3.5 An Energy Closure based on Counter-Streaming Ions

In order to close the ADNLSB equations, we need a energy closure $\varepsilon(b_t)$. The modeling of the energy closure for a collisionless plasma has historically been difficult. The Chew-Goldberger-Low (CGL) condition [16] is one choice, but it does not work well when streaming ions are present. Since we are here just trying to qualitatively demonstrate the underlying physics, we will assume that we have a

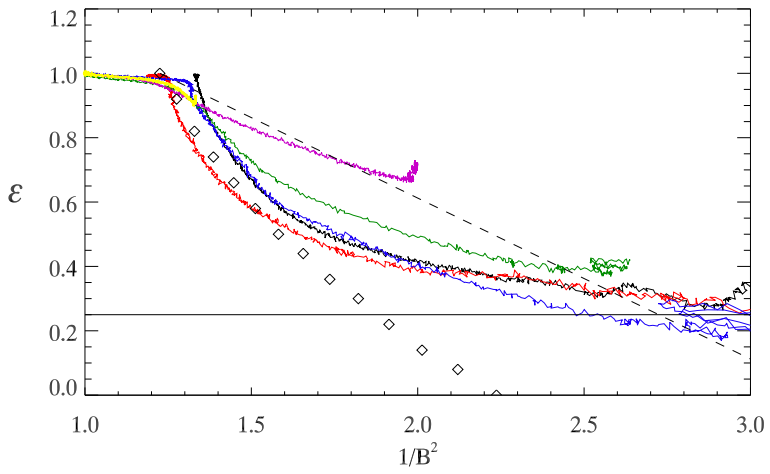

Figure 3.2: The ε distribution vs. $1/B^2$ for the cases $\theta_{BN} = 30°$(yellow), 45°(magenta), 52°(green), 60°(blue), 75°(red) and 83°(black) from Fig. 2.6. The dashed line has slope -0.5. In comparison, the diamond curve is the theoretical prediction with the CGL condition for the $\theta_{BN} = 75°$ case.

$\varepsilon(b_t)$, where ε and $|B|$ are simply related by

$$\varepsilon = c_1 - \frac{c_2}{B^2} \tag{3.15}$$

with positive constants c_1 and c_2 and the condition $c_1 - c_2/B_0^2 = \varepsilon_0$ is imposed. This functional form is motivated by the nearly constant parallel pressure maintained by free-streaming ions ($c_2 \sim P_\parallel$). Although Eq. (3.15) is strictly empirical, results from PIC simulations (see Fig. 3.2) suggest that $c_2 = 0.5$ provides a reasonable first approximation and will be used in the following calculations.

We take the variation,

$$\delta\varepsilon = \varepsilon - \varepsilon_0 \sim \frac{c_2}{B_x^2 b^4}\delta(b_t^2) = \frac{c_2}{B_x^2 b^4}(b_t^2 - b_{t0}^2) \tag{3.16}$$

where $b^2 = 1 + b_t^2$. This parameterization will be valid whenever $\delta\varepsilon(b_t) \ll \varepsilon_0$.

Therefore, an effective nonlinearity in Eq. (3.1) can be written as,

$$\alpha_{\text{eff}}(b_t) = \alpha + \Omega \frac{c_2}{B_x^2 b^4} \tag{3.17}$$

The most important conclusions in the remainder of this work do not depend on the details of the closure, but only that ε decreases as $|B|$ decreases. Note that $\Omega \sim 1/2\varepsilon_0$ is mostly positive in the limit in which we are interested. This fact will be used in the following section.

3.6 The Pseudo-Potential: Looking for a Stationary Solution

3.6.1 The Formation of Compound SS/RD Waves and SS/IS Waves

In order to determine both where the path in the state space of Fig. 3.1(c) will turn to the intermediate rotation and the nontrivial coupling of the slow and intermediate modes when temperature anisotropies are present, we construct the pseudo-potential of a stationary solution. We will look for a equation that possesses traveling stationary waves, by substituting $\mathbf{b}_t = \mathbf{b}_t[\xi(\eta - V_S\tau)]$ (where V_S is the speed of the stationary wave observed in the upstream intermediate frame) into Eq. (3.1) and integrating over ξ once. We obtain

$$R\partial_\xi \mathbf{b}_t - \frac{1}{2\sqrt{\varepsilon_0}} d_i \partial_\xi (\hat{\mathbf{x}} \times \mathbf{b}_t) = -V_S(\mathbf{b}_t - \mathbf{b}_{t0}) + \alpha_{\text{eff}}(b_t)\mathbf{b}_t(b_t^2 - b_{t0}^2) \equiv -\mathbf{F} \equiv \partial_{\mathbf{b}_t}\Psi. \tag{3.18}$$

In this formulation we can treat $\mathbf{b}_t$ as a spatial coordinate, and ξ as time. The terms on the LHS of Eq. (3.18) behave analogously to, respectively, a frictional force and a Coriolis force with rotational frequency $d_i/\sqrt{\varepsilon_0}$ and rotational axis $\hat{\mathbf{x}}$.

A pseudo-potential Ψ that characterizes the nonlinearity is uniquely defined because $\partial F_z/\partial b_y = \partial F_y/\partial b_z$. We are only interested in the small V_S limit, because the upstream values with subscript "0" are expected to be the upstream values of a switch-off slow shock in ideal isotropic MHD, which propagates at the upstream intermediate speed. The anisotropy in our PIC simulations does not seem to significantly change this behavior as shown in chapter 2.

Calculating the pseudo-work done on the pseudo-particle, $\int[\text{Eq.}(3.18)]\cdot\partial_\xi \mathbf{b}_t d\xi$, we obtain

$$\Psi|_{\text{up}}^{\text{down}} = R\int_{\text{up}}^{\text{down}} (\partial_\xi \mathbf{b}_t)^2 d\xi < 0 \tag{3.19}$$

Note that from upstream to downstream is in the negative ξ direction. The pseudo-particle will move to a lower potential, while its total energy is dissipated by the resistivity and the rate of the drop depends on the strength of the resistivity. Kennel *et al.* [52] have shown that when pseudo-particles move toward lower pseudo-potentials, the entropy increases and so the resulting shock is admissible. Note that the Coriolis-like force does not do work. It only drives rotation of the pseudo-particle on the iso-surface of the pseudo-potential and hence causes stable nodes to become stable spiral nodes and unstable nodes to become unstable spiral nodes, thus leading to the formation of dispersive wavetrains [40, 121]. We will neglect its effect in the following discussion.

The pseudo-potential is shown in Fig. 3.3(a) for the parameters $\theta_0 = 42°$, $\beta_0 = 1$, $\varepsilon_0 = 1$, $c_2 = 0.5$ and $V_S = 0$. The temperature anisotropy has turned the origin from a local minimum of the pseudo-potential in the isotropic MHD model to

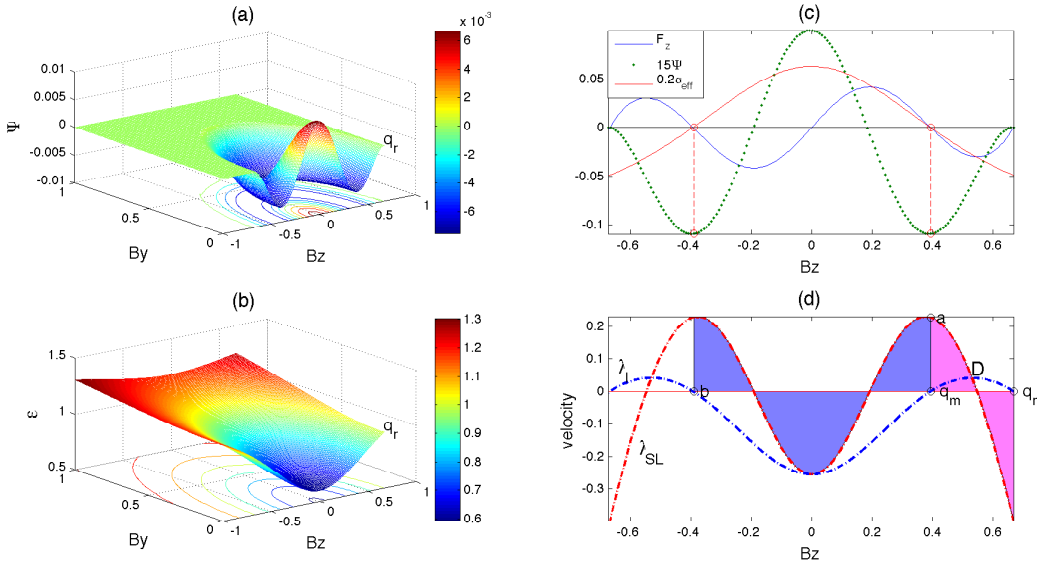

Figure 3.3: Panel (a): A pseudo-potential Ψ with $V_S = 0$. Upstream (point $\mathbf{q}_r$), $\theta_0 = 42°, \beta_0 = 1, \varepsilon_0 = 1, c_2 = 0.5$ and we choose $\Psi(\mathbf{q}_r) = 0$. Since the transition occurs within the radius $b_t = b_{z0}$, we set $\Psi = 0$ for $b_t > b_{z0}$ for a better visualization. The potential for negative B_y is mirror symmetric to the part shown here; Panel (b): $\varepsilon(b_t)$; Panel (c): Cuts of Ψ, F_z, and α_{eff} along the B_z axis with $B_y = 0$; Panel (d): λ_I and λ_{SL} along the B_z axis with $B_y = 0$. The vertical axis measures speed (normalized to C_{An}). "D" stands for degeneracy. The red area above V_S (zero here) equals the red area below V_S, and the same rule applies to the blue area.

a local maximum. We term this the "reversal behavior". A pseudo-particle initially at point $\mathbf{q}_r$ will slide down the hill in the slow mode eigen-direction, and then follow the circular valley in the intermediate eigen-direction. Without the reversal behavior (e.g., in isotropic MHD) the pseudo-particle will slide down to the origin and form a switch-off slow shock. The trajectory of the pseudo-particle can also be calculated by numerically integrating Eq. (3.18) with respect to ξ. In (b) the variation of the temperature anisotropy is shown. Similar reversal behaviors can be found in fully anisotropic MHD with the energy closure used here, or with the CGL closure (see Appendix A.4.1).

In Fig. 3.3 (c), we plot a cut of the pseudo-force, F_z, effective $\alpha_{\rm eff}$ and the pseudo-potential Ψ along the b_z axis ($b_y = 0$), which is the eigen-direction of a slow mode beginning at $\mathbf{q}_r = (b_{z0}, 0)$. Here

$$F_z = -\alpha_{\rm eff}(b_z) b_z (b_z^2 - b_{z0}^2) + V_S (b_z - b_{z0}). \tag{3.20}$$

It is clear that Ψ_{min} occurs at $F_z = 0$ in Fig. 3.3(c), since Ψ is constructed by integrating the pseudo-force $\mathbf{F}$. In Fig. 3.3 (d) we plot cuts of the characteristics of the slow and intermediate modes along the b_z axis.

$$\lambda_{SL} = \alpha(3b_z^2 - b_{z0}^2) + \Omega \frac{c_2}{B_x^2} \left[\left(\frac{1}{b^4} - 4\frac{b_z^2}{b^6} \right) (b_z^2 - b_{z0}^2) + 2\frac{b_z^2}{b^4} \right] \tag{3.21}$$

$$\lambda_I = \alpha_{\rm eff}(b_z)(b_z^2 - b_{z0}^2) \tag{3.22}$$

The temperature anisotropy has changed the structure of these characteristics. As a result, there are new degeneracy points ($\lambda_{SL} = \lambda_I$) between slow and intermediate waves such as the point "D". The slow characteristic shows extra nonconvexity

points, where no steepening and spreading occurs (*i.e.*, $\nabla_{\mathbf{q}}\lambda_{SL}(\mathbf{q}) \cdot \mathbf{r}_{SL}(\mathbf{q}) = 0$), such as the point **a** (the local maximum of λ_{SL}). This is clearer when we compare the slow characteristic here to that in the isotropic case shown in Fig. A.2, where $b_t = 0$ is the only degeneracy point and the nonconvexity point of the slow mode.

In order to identify the nonlinear waves determined by the route of the pseudo-particle, we apply the equal-area rule, which tells how shocks are steepened from characteristics. The equal-area rule (see Appendix A.5 for more details) applied to λ_{SL} shows that the sliding route (point $\mathbf{q}_r$ to $\mathbf{q}_m$) forms a slow shock. Since $\nabla_{\mathbf{q}}\lambda_{SL}(\mathbf{q}) \cdot \mathbf{r}_{SL}(\mathbf{q}) < 0$ therefore $\lambda_{SL}|_{\mathbf{q}_m} > \lambda_{SL}|_{\mathbf{q}_r}$, and thus the slow mode will steepen until the red area above the horizontal line $V_S = 0$ equals the red area below $V_S = 0$. The slow shock transition immediately connects to the intermediate mode (point $\mathbf{q}_m$ to **b**, which is also from the equal-area rule on λ_{SL}) in the valley. The fact that both the upstream (point $\mathbf{q}_m$) and downstream (point **b**) travel at the local λ_I makes the intermediate discontinuity a RD. By comparing (c) and (d), we note that the potential minimum is exactly the location of $\mathbf{q}_m$ as expected and it is below the degeneracy point ($b_z|_D > b_z|_{\mathbf{q}_m}$). This fact is consistent with the comment in section 3.4, which predicts that $\mathbf{q}_m$ will be inside the degeneracy band. The horizontal lines $\mathbf{q}_r - \mathbf{q}_m$ and $\mathbf{q}_m - \mathbf{b}$ measure the propagation speed of the SS and the RD, which in this case are both zero in the upstream intermediate frame. They therefore form a compound SS/RD wave. The downstream of the slow shock (point $\mathbf{q}_m$) is not able to connect to the slow rarefaction (SR) wave (point **a**) and thus not able to form a compound SS/SR, since the rarefaction is faster than the shock itself. This model gives an theoretical explanation for the possible satellite

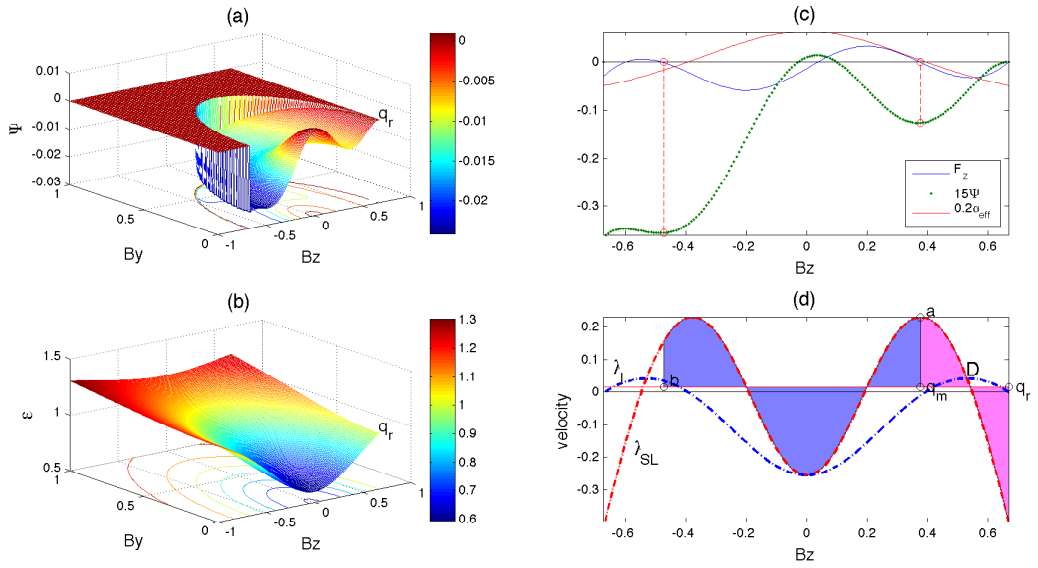

Figure 3.4: Same format as Fig. 3.3 but with $V_S = 0.015 \gtrsim 0$.

observations of compound SS/RD [115, 114], and the "compound SS/RD/SS waves" seen in hybrid simulations [59].

When $V_S \gtrsim 0$ the potential tilts down in the negative b_z direction (see Fig. 3.4). In this case, the slow shock (point $\mathbf{q}_r$ to $\mathbf{q}_m$ in Fig. 3.4(d)) with shock speed V_S is connected by an intermediate shock (IS) (point $\mathbf{q}_m$ to $\mathbf{b}$) with shock speed V_S, whose upstream is super-intermediate ($V_S > \lambda_I|_{\mathbf{q}_m}$) while the downstream is sub-intermediate ($V_S < \lambda_I|_{\mathbf{b}}$). This forms a compound SS/IS wave. Note that the intermediate shock is not steepened from the intermediate mode (which is consistent with the discussion in Sec. 3.4), but is steepened from the slow mode. The slow shock is abnormal with both upstream (point $\mathbf{q}_r$) and downstream (point $\mathbf{q}_m$) being super-intermediate. Karimabadi *et al.* [50] call a similar kind of slow shock an anomalous slow shock. When $V_S \lesssim 0$ the potential tilts up in the negative b_z direction and

there is no extra transition at the SS downstream, since $\Psi(\mathbf{b}) > \Psi(\mathbf{q}_m)$ in this case and is therefore not accessible.

These conclusions are independent of the details of $\varepsilon(b_t)$, but only require the reversal behavior somewhere downstream of the slow shock. This fact can be inferred from a simple relation: $V_S - \lambda_I(b_z) = (b_{z0}/b_z)V_S$ for $b_z = b_z|_{\mathbf{q}_m}$ or $b_z|_{\mathbf{b}}$, regardless of the detail of $\varepsilon(b_t)$ (from Eq. (3.20) and (3.22)). When $V_S = 0$, this relation ensures that the SS can always connect to a RD since $V_S - \lambda_I = 0$ at both points $\mathbf{q}_m$ and $\mathbf{b}$. When $V_S \gtrsim 0$, the SS can always connect to an IS since $V_S - \lambda_I$ is positive (super-intermediate) at $\mathbf{q}_m$ and negative (sub-intermediate) at $\mathbf{b}$. We therefore conclude that the abnormal transitions of magnetic field structures seen in the PIC simulations of chapter 2 are most likely the transitions from the SS to the RD in a compound SS/RD wave or the SS to the IS in an SS/IS wave. We can hardly distinguish between these two compound waves in our PIC simulation, since V_S is small and the time-dependent dynamics add uncertainties in measuring the exact value. We focus on further analyzing the compound SS/RD wave.

3.6.2 The Significance of $\varepsilon = 0.25$

For SS/RD waves ($V_S = 0$), the stationary points along $b_{z,s}$ are the roots of $F_z = 0$,

$$\alpha_{\text{eff}}(b_{z,s})b_{z,s}(b_{z,s}^2 - b_{z0}^2) = 0 \tag{3.23}$$

Here the subscript "s" represents "stationary". We have three traditional stationary points, $b_{z,s} = b_{z0}$ (point $\mathbf{q}_r$), $-b_{z0}$ and 0, as well as a new stationary point due to the

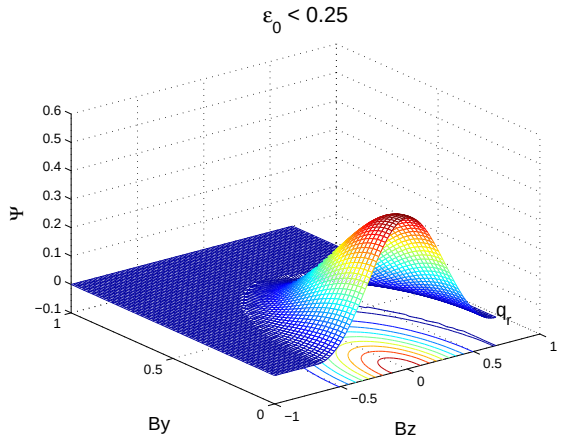

Figure 3.5: The pseudo-potential with $\varepsilon_0 = 0.24 < 0.25$, while other parameters are the same as Fig. 3.3.

temperature anisotropy, $b_{z,m}$ (the transition point $\mathbf{q}_m$) determined by $\alpha_{\text{eff}}(b_{z,m}) = 0$. The fixed-point analysis of the first three points in isotropic fluid theory can be found in the literature [52, 121, 39, 40].

As shown in Fig. 3.5, there is no slow mode transition if

$$\varepsilon_0 < \frac{1}{4} = 0.25 \tag{3.24}$$

(note that this relation is independent of θ_{BN} and β), which occurs when the nonlinearity α of Eq. (3.1) changes sign from $\alpha < 0$ to $\alpha > 0$. A positive α will result in a positive α_{eff} in Eq. (3.17), and therefore no solution for $b_{z,m}$. Only rotation of the magnetic field is thus allowed. If $\varepsilon_0 > 0.25$, we can further show that $\varepsilon_0 \geq \varepsilon_m (\equiv \varepsilon|_{\mathbf{q}_m}) \geq 0.25$ is always true for a slow shock transition from ε_0 to ε_m in this compound wave by the full jump conditions of anisotropic-MHD (Appendix A.4.2). Therefore, the nonlinear fluid theory provides a lower bound of $\varepsilon_m \geq 0.25$ at the SS to RD transition inside these compound waves, regardless of the details

of $\varepsilon(b_t)$. In other words, the downstream magnetic field cannot exhibit switch-off behavior if the firehose-sense temperature anisotropy is strong enough. This fact explains the non-switch-off slow shocks often seen in kinetic simulations discussed in Sec. 1.3.3 [71] and satellite crossings discussed in Sec. 1.3.2 [100]. Once it transitions to the intermediate mode, a gyrotropic $\varepsilon(b_t)$ will stay close to ε_m, since the intermediate-rotation nearly preserves the magnitude of the B field and therefore ε. Note the assumption of gyrotropic $\varepsilon(b_t)$ is expected to be valid only in length scale larger than local ion inertial length and ion gyro-radius.

In these demonstrations we use shocks with moderate parameters, such as $\theta_{BN} = 42^\circ$ and $\beta_0 = 1$. In general, larger θ_{BN}, β_0, and smaller ε_0 will make the ratio $|\Omega|/|\alpha|$ larger, and therefore generate a stronger reversal tendency. An analysis with full anisotropic MHD (Appendix A.4) should be used for strong slow shock transitions, due to the limits of the ADNLSB, although the underlying physical picture will be similar.

3.7 Toward the Critical $\varepsilon = 0.25$: Time-Dependent Dynamics

The initial conditions that characterize the exhaust of anti-parallel reconnection (initial $b_y = 0$) require $\mathbf{b}_t = 0$ at the symmetry line at later time. This eventually forces the pseudo-particle to climb up the potential hill to the local maximum ($b_z = 0, b_y = 0$), which implies an intrinsic time-dependent process at the symmetry line since Eq. (3.18) does not yield such a solution. Meanwhile, the fact that $\mathbf{b}_t$ needs to go to zero at the symmetry line provides a spatial modulation on

the amplitude of the rotational intermediate mode. Note that the transition point from SS to RD in compound SS/RD waves could potentially induce modulation too. As suggested in Sec. 2.6, a spatially modulated rotational wave tends to break into d_i-scale dispersive waves, which can make the rotational component of the transition very turbulent.

As pointed out in Sec. 3.6.2, the nonlinear fluid theory of the time-independent stationary solutions only provides a lower bound $\varepsilon_m > 0.25$ for the transition point inside these compound SS/RD waves. Counter-streaming ions, by raising $P_\parallel$, push ε_m lower. Once ε_m is lower than 0.25, the magnetic field rotates, generates d_i-scale waves, and scatters $P_\parallel$ into $P_\perp$. This raises ε_m, changing the functional form of $\delta\varepsilon$ and driving it toward 0, which self-consistently results in a transition at the potential minimum where $\alpha_{\text{eff}} = \alpha = 0$, and thus $\varepsilon = 0.25$. This argument explains the $\varepsilon = 0.25$ plateau observed in the PIC simulations for different shock angles (see Fig. 2.8). With $\delta\varepsilon = 0$, this point is exactly the degenerate point of the slow and intermediate modes.

3.8 The Supporting Evidence from Numerical Experiments

The evidence for a slow mode connecting to rotational waves can be seen in the PIC simulations that are discussed in detail in chapter 2. In previous kinetic simulations, the downstream rotational waves were often identified as slow dispersive wavetrains arising from, for instance, the second term in the RHS of Eq. (3.1). Here we present further evidence, in addition to the numerical evidence that $\varepsilon = 0.25$, to

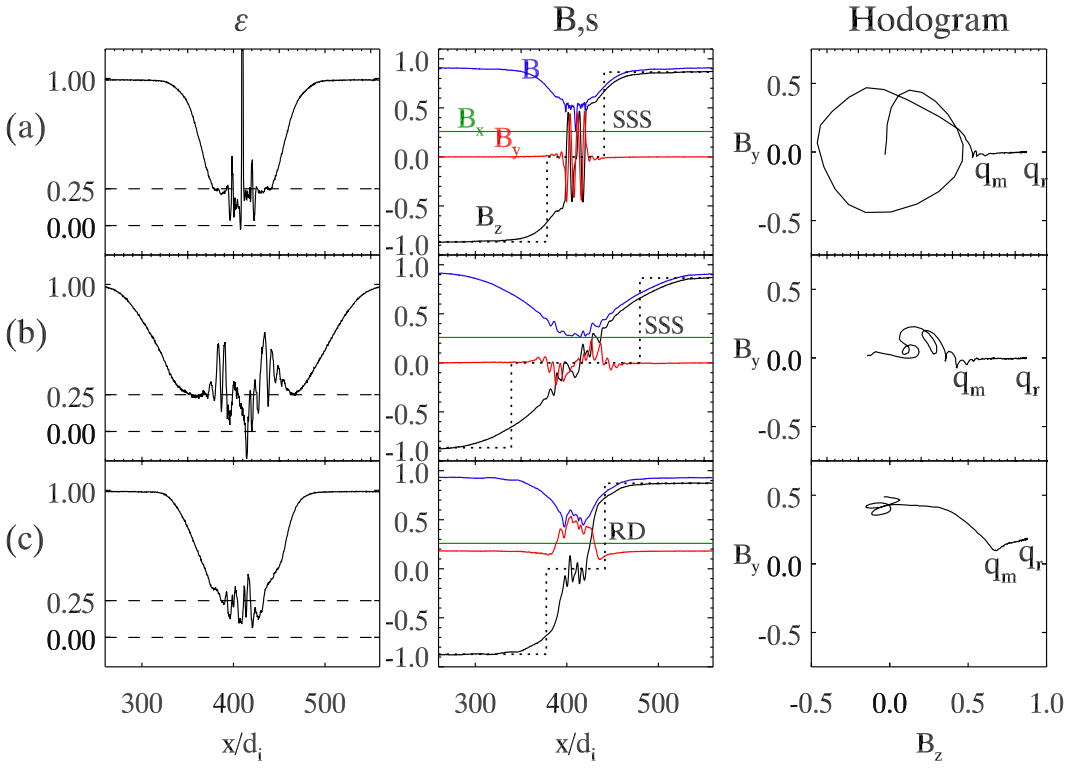

Figure 3.6: Results of PIC simulations (runs **f**, **g** and **h** of chapter 2). Row (a): A case with $\theta_{BN} = 75°, \beta_0 = 0.4$ and initial width $w_i = 1d_i$ at time $200/\Omega_{ci}$. ε is shown on the left, different magnetic components in the middle, B_z-B_y hodogram on the right; Row (b): A similar case with a wider initial width $w_i = 10d_i$ at time $450/\Omega_{ci}$; Row (c): A similar case to (a), but with a weak guide field $B_{y0} = 0.2B_0$ at time $200/\Omega_{ci}$. The dotted curves in the center column are the predicted B_z magnitudes and positions of switch-off slow shocks (SSS) or rotational discontinuities (RD) from isotropic MHD theory [65].

support the idea that the downstream rotational mode is tied to the intermediate mode. Fig. 3.6 shows the results from three PIC simulations that were designed to explore the structure of reconnection exhausts in the normal direction. The format is the same as for Fig. 2.6, with the first column showing ε, the second column the magnetic field components, and the third column a hodogram of the fields. The dashed curves in the second column (the predicted B_z by ideal isotropic MHD [65]) indicate that a pair of switch-off slow shocks or a pair of rotational discontinuities will propagate out from the center. All three cases show the correlation between $\varepsilon = 0.25$ and the transition from coplanar to non-coplanr rotation of the downstream magnetic fields. The hodograms are readily comparable to the state space plots such as Fig. 3.1 (c). In Fig. 3.6(a), the downstream region of a slow shock shows a high wavenumber ($\sim 6d_i$) left-handed (LH) polarized rotational wave, which is difficult to distinguish from the predicted downstream ion inertial scale dispersive slow mode wavetrain [17]. Fig. 3.6(b) shows results from a simulation with a larger initial current sheet width and exhibits a longer wavelength ($\sim 30d_i$) LH rotational wave which can be identified as an intermediate mode The intermediate mode breaks into smaller ion inertial scale waves, which have been identified as dispersive waves in Sec. 2.6. By comparing (a) and (b), we note that the downstream primary rotational wave tends to maintain its spatial scale as an intermediate mode with non-steepening and non-spreading properties. Another way to distinguish the dispersive behavior from the non-dispersive rotation is by including a weak guide field. In Fig. 3.6(c), the front of the rotational downstream wave turns into a well-defined RD when a weak guide field is included. Its amplitude is about the same as that of the large

amplitude rotational waves in (a). Most importantly, there is a clear slow shock ahead of the RD. Because the symmetry of the initial condition is broken by the guide field, the downstream RD does not need to end at $b_y = 0$; instead it ends inside the potential valley at $\mathbf{b}_t = (0, b_{z,m})$ (see the hodogram of (c)), as expected.

3.9 Conclusion and Discussion

The existence of compound SS/RD, SS/IS waves arising from firehose-sense and $|B|$-correlated ε (temperature anisotropies) are theoretically demonstrated by analyzing the anisotropy-caused reversal of a pseudo-potential. The pseudo-potential is known to characterize the nonlinearity of hyperbolic wave equations. Extra degeneracy points between slow and intermediate modes as well as extra non-convexity points in the slow characteristics are introduced by the temperature anisotropy. The slow shock portion of a compound SS/IS wave is an anomalous slow shock with both up and downstream being super-intermediate. The nonlinear fluid theory provides a lower bound of $\varepsilon = 0.25$ for the SS to RD transition, regardless of the details of the energy closure $\varepsilon(b_t)$. The wave generation from the rotational intermediate mode discussed here and in Sec. 2.6 helps keep $\varepsilon = 0.25$. This explains the critical anisotropy plateau observed in the oblique slow shock PIC simulations documented in chapter 2. The critical ε value 0.25 is calculated from the degree of freedom of monatomic plasmas. A general expression of this value is $(6 - D_{\text{free}})/(6 + 2D_{\text{free}})$ where the degree of freedom $D_{\text{free}} = 3$ for monatomic plasmas, and $D_{\text{free}} = 5$ for diatomic plasmas. This study also suggests that it is a pair of compound SS/RD

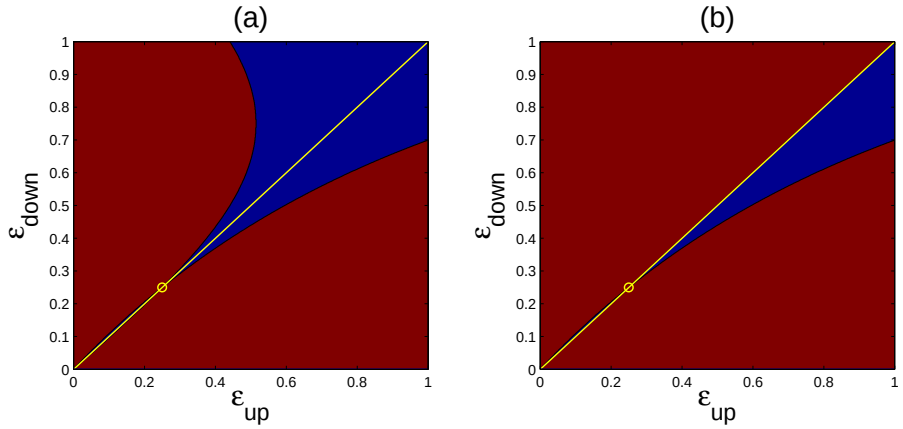

Figure 3.7: In panel (a), the possible jumps of ε of an anisotropic-RD, are constrained by requiring positive $P_{\perp d}$, $P_{\parallel d}$ and B_d^2. The red region is forbidden. In panel (b), the plot is further constrained by the requirement that entropy increases (with an entropy from the H-theorem defined as $\ln(P_\parallel^{1/3} P_\perp^{2/3}/\rho^{5/3})$ for a bi-Maxwellian distribution). The constraint of increasing entropy has eliminated the region above the diagonal line when $\varepsilon_{up} > 0.25$, and the region below the diagonal line when $\varepsilon_{up} < 0.25$. Here $\beta_0 = 1$; a higher β_0 would collapse the valid region into a narrower region along the diagonal line.

waves that bound the antiparallel reconnection outflow, instead of a pair of switch-off slow shocks as in Petschek's reconnection model. In previous hybrid and PIC simulations, the downstream sharp rotational waves were often identified as slow dispersive waves of a switch-off slow shock. Instead, we propose that they are the intermediate portion of the compound SS/RD wave. The slow shock portion becomes less steep due to the time-of-flight effect of backstreaming ions.

The singularity of $\varepsilon = 0.25$ was also noticed by P. D. Hudson (1971) [46] in his study on the anisotropic rotational discontinuity (A-RD). Unlike the RD in a compound SS/RD wave, an A-RD changes ε, magnetic field strength and thermal states. Through the constraint of the positivity of $P_\parallel$, $P_\perp$ and B^2, he derived all

of the possible jumps (independent of the energy closure used) of the temperature anisotropy across an A-RD, as shown in Fig. 3.7(a). The ADNLSB inherits most of the hyperbolic properties (such as the extra nonconvexity and degeneracy points) of anisotropic MHD and also the singular behavior, $\Delta\varepsilon = \varepsilon_{\rm up} - \varepsilon_{\rm down} \to 0$ when $\varepsilon \to 0.25$. We can tell this by searching for stationary solutions where the pseudo-force $F_z = 0$ (the general form of Eq. (3.20)). Again,

$$V_S(b_z - b_{z0}) - \alpha b_z(b_z^2 - b_{z0}^2) - \Omega b_z(\varepsilon - \varepsilon_0) = 0 \tag{3.25}$$

A stationary A-RD exists at $\varepsilon_0 = 0.25$ (*i.e.,* $V_S = 0$, $\alpha = 0$ and $b_z \neq 0$), only if we require $\varepsilon - \varepsilon_0 = 0$. An arbitrary magnetic field magnitude and rotation are then allowed, as shown by Hudson. After further constraining the possible jumps by requiring that entropy increase, the solution above the diagonal line in Fig. 3.7(b) is eliminated when $\varepsilon_{\rm up} > 0.25$ while the solution below the diagonal line is eliminated when $\varepsilon_{\rm up} < 0.25$. He also noticed that the jump behavior of an A-RD for $\varepsilon_{\rm up} > 0.25$ is slow-mode-like (*i.e.* δn and δB are anti-correlated), while it is fast-mode-like (*i.e.* δn and δB are correlated) for $\varepsilon_{\rm up} < 0.25$. This directly relates to the fact that the jump of an A-RD equals the jump of the compound SS/RD wave (see Appendix A.4.3), and a slow mode turns fast-mode-like when $\alpha > 0$ [52].

Chapter 4

Summary

4.1 Summary of Results

The physics of plasmas has played increasingly important role in modern space physics and astronomy. The topological change of magnetic fields and the plasma heating caused by reconnection and associated shocks play an important role in many macro-scale plasma systems. Therefore a better understanding of the detailed kinetic behavior of these processes can make a profound contribution to these fields. Fast magnetic reconnection takes the form of a Petschek-like configuration with opened reconnection nozzles. The well-accepted Petschek model predicts the existence of a pair of switch-of-slow shocks that bound the reconnection exhausts and help convert magnetic energy into plasma kinetic and thermal energy. However, a self-generated firehose-sense temperature anisotropy caused by kinetic streaming ions slows the propagation of intermediate modes and speeds up the propagation of slow shocks. As a consequence, a rotational intermediate mode can arise downstream of a slow shock. The nontrivial coupling of these modes forms a single nonlinear wave that is a mixture of both slow and intermediate modes. We call it a compound SS/RD wave. Under some circumstances, a compound SS/IS can also form. When the firehose stability parameter $\varepsilon \equiv 1 - \mu_0(P_\parallel - P_\perp)/B^2$ reaches the critical value of 0.25, the slow-to-intermediate transition inside these compound waves occurs, a

transition closely associated with the degenerate behavior of these two characteristic MHD modes.

4.2 Implications and Unsolved Issues

The results of this thesis provide a theoretical explanation of the observations of "Double Discontinuity" by Whang *et al.* [115, 114, 113] in GEOTAIL and WIND data. In Fig. 4.1, Whang shows the results of an in-situ observation with high temporal resolution (62.5 millisecond compared to a standard 3-12 seconds) of the boundary of the tail lobe (on the left) and the plasma sheet (on the right) on February 14, 1994. Here the "S" on the top denotes a suspected slow shock (SS) and "R" denotes a suspected rotational discontinuity (RD). A major decrease in the total magnetic field (B) and the tangential magnetic field (B_t) are seen, while the electron and ion densities (N_e and N_i) increase. These transitions fit the profiles of a SS. ϕ measures the rotation angle of the tangential magnetic field with the rotation axis pointing in the normal direction ($\hat{\mathbf{x}}$). Note the large rotation in the tangential magnetic field while the total magnetic field remains constant downstream of the SS, which is the signature of a RD. These "Double Discontinuities" strongly resemble the compound SS/RD waves theoretically identified in this thesis. The existence of these compound waves also potentially explains the in-situ observations by Seon (1996). As mentioned in Sec. 1.3.2, the non-switch-off slow shock is likely to be followed by a large-amplitude and long-wavelength intermediate rotational wave that radiates ion-inertial scale dispersive waves. We see the similarity in the structure of

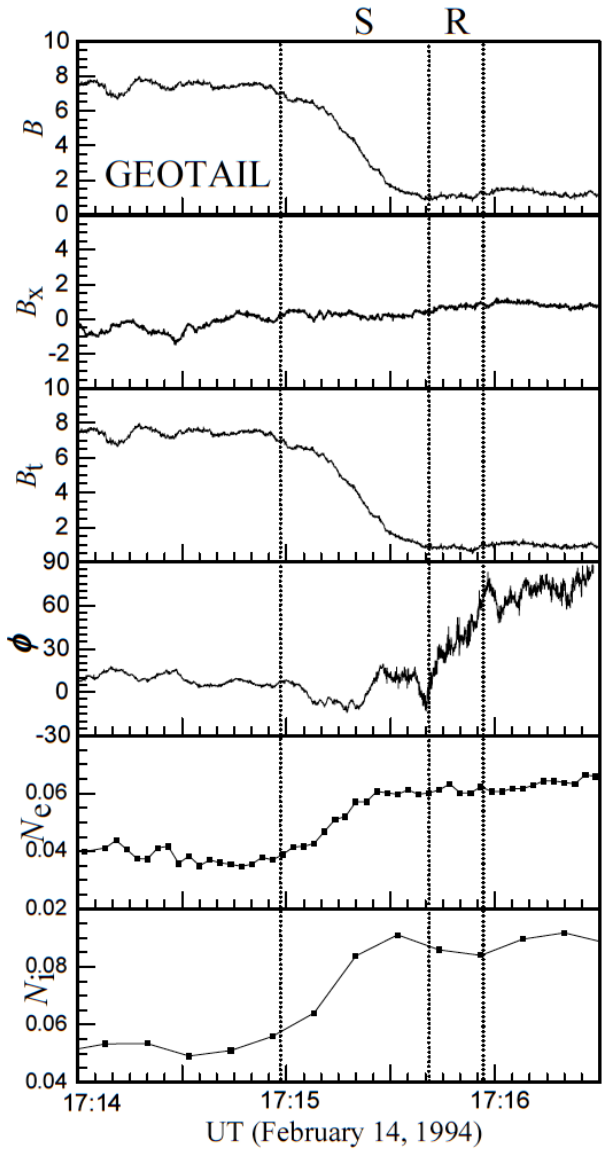

Figure 4.1: An observation of "Double Discontinuity" at Earth's magnetotail by *GEOTAIL* on February 14, 1994 at $X_{\mathrm{GSM}} = -54R_e$. (Reprinted with permission from Ref. [Whang, 2004]. ©2004 by the European Geosciences Union)

the magnetic fields when we compare Fig. 2.9 to Fig. 1.9. A satellite mission that highly resolves both ε and the magnetic fields across the tail reconnection exhaust would help judge the validity of our theory.

A larger PIC reconnection simulation with a reconnection outflow that reaches $\sim 100d_i$ downstream from the X-line is shown in Fig. 4.2. The outflow length is about twice that of the simulation shown in Fig. 1.11. Panel (a) shows the out-of-plane current density, and vertical cuts coded with different colors. The firehose stability parameter ε along each cut is plotted in panel (b). ε shows a clear tendency towards forming a plateau at $\varepsilon = 0.25$ in the farthest downstream cut. However, convincing evidence of the SS to RD transition in compound SS/RD waves requires even larger simulations. The compound wave also explains the "step-like" slow shocks seen in Lottermoser *et al.*'s large-scale hybrid reconnection simulation [71] as mentioned in Sec. 1.3.3. The smooth non-switch-off transition in the reconnecting magnetic field component of kinetic simulations is the intermediate portion of the compound wave.

Compared to slow shocks, fast shocks have been intensively studied (see, for instance, the review article [108]). The formation of shocklet and short, large-amplitude magnetic structures (SLAMs) in the upstream region of Earth's quasi-parallel bow shock has been observed [72] and simulated [80, 97]. The formation mechanism of SLAMs could be similar to that of the turbulent waves observed at our simulations. In our slow shock simulations, the downstream rotational parent waves break into SLAMs-like structures, as in Fig. 2.9(b). Since the transition of the magnetic field across the front in a fast shock is opposite to that in a slow shock, any

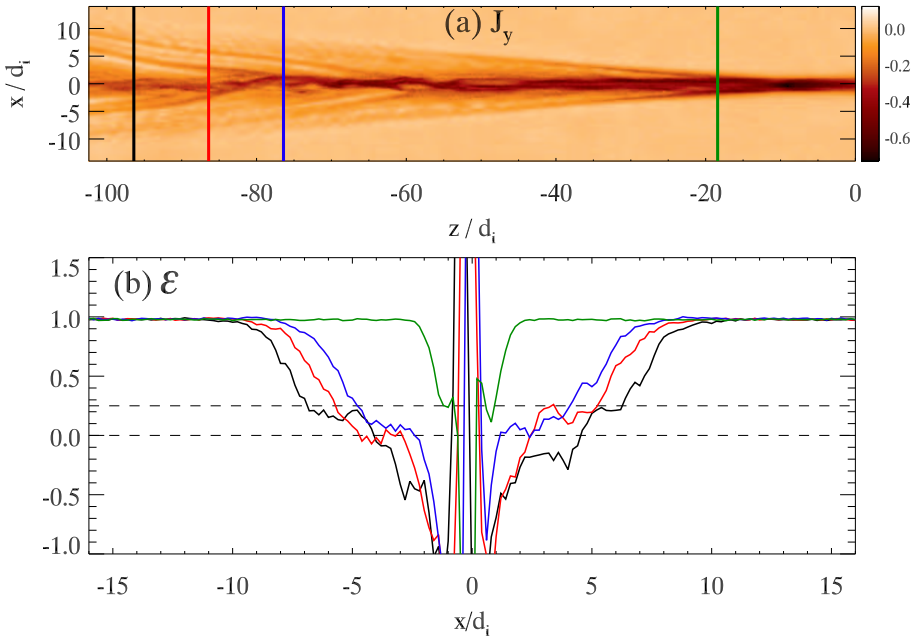

Figure 4.2: A larger PIC reconnection simulation shows a clearer $\varepsilon \sim 0.25$ plateau at farther downstream. Panel (a) is the out-of-plane current density; Panel (b) are the distributions of firehose stability parameter ε along cuts (coded by colors) in (a).

SLAMs associated with a slow shock are expected to exist in the downstream region, especially since the downstream of a switch-off slow shock is locally quasi-parallel. Other than the 1-D waves generated by the competition between the nonlinear steepening and the dispersion, we also observe 2-D turbulence that develops in the firehose unstable region of the reconnection outflow, and whose signatures are clear in the J_y component of Fig. 4.2, and the J_{ey} and B_x components of Fig. 1.11. However, we are not able to definitively identify it as the firehose instability at this stage, because in this highly inhomogeneous plasma factors such as magnetic field gradients or shear flows could also potentially act as instability drivers.

As to the question of the heating ability of these compound waves, we have not seen super-thermal particles other than Alfvénic streaming ions in our shock simulations. However, it is still an open question whether particles could be accelerated by slow shock associated reconnection exhausts in larger 2-D systems via mechanisms recognized in fast shocks such as the 1st-order Fermi mechanism [7], diffusive shock acceleration (DSA) [60, 34], and those possible injection mechanisms for DSA such as shock-drift [24], or shock surfing [93]. In addition, Drake et al. (2009) [28] studied the pick-up process by the reconnection outflow which is also relevant to accelerating particles.

This thesis work will help observers explain in-situ satellite data of anti-parallel reconnection, and help guide future satellite missions such as the Magnetospheric Multiscale Mission (MMS) and Solar Probe Plus. With a strong guide field, even though streaming ions still persist, the firehose stability parameter ε will stay close to unity. We therefore expect the Riemann solution of Fig. 1.18 in isotropic MHD to

do a better job of explaining the overall wave structures of reconnection exhausts. In this case, a pair of rotational discontinuities will be responsible for switching off the downstream reconnecting magnetic field, not a pair of switch-off slow shocks. This fact has already been observed in kinetic simulations [66], and may help explain the structure of reconnection in the solar wind, where strong guide fields usually exist.

Appendix A

Overview

A.1 From Anisotropic MHD to the Anisotropic DNLSB Equation

From moment integrations of the Vlasov equation that neglect the off-diagonal components of the pressure tensor (the empirical validity of this approximation for our system is shown in Fig. 2.2(c)), we can write down the anisotropic MHD (AMHD) equations, as documented in Sec. 1.5 [14, 45]. The energy closure is undetermined.

In Lagrangian form,

$$\frac{d}{dt}\rho + \rho\partial_x V_x = 0, \tag{A.1}$$

$$\rho\frac{d}{dt}V_x + \partial_x P + \partial_x\left[\frac{1}{3}\left(\varepsilon+\frac{1}{2}\right)\frac{B_t^2}{\mu_0}\right] - \frac{2}{3}\frac{B_x^2}{\mu_0}\partial_x\varepsilon = 0, \tag{A.2}$$

$$\rho\frac{d}{dt}\mathbf{V}_t - \frac{B_x}{\mu_0}\partial_x(\varepsilon\mathbf{B}_t) = 0, \tag{A.3}$$

$$\frac{d}{dt}\mathbf{B}_t - B_x\partial_x\mathbf{V}_t + \mathbf{B}_t\partial_x V_x = \partial_x(\eta_r\partial_x\mathbf{B}_t) - \partial_x\left(\frac{B_x}{\mu_0 ne}\hat{\mathbf{x}}\times\partial_x\mathbf{B}_t\right), \tag{A.4}$$

$$\begin{aligned}\frac{d}{dt}P - \frac{\gamma P}{\rho}\frac{d}{dt}\rho + (\gamma-1)\left[\frac{1}{3}(\varepsilon+2)\frac{B^2}{\mu_0} - \varepsilon\frac{B_x^2}{\mu_0} - \frac{B_t^2}{\mu_0}\right]\partial_x V_x \\ +(\gamma-1)(1-\varepsilon)\frac{B_x\mathbf{B}_t}{\mu_0}\cdot\partial_x\mathbf{V}_t + (\gamma-1)\partial_x Q_x = 0,\end{aligned} \tag{A.5}$$

where

$$\varepsilon \equiv 1 - \frac{P_\parallel - P_\perp}{B^2/\mu_0}, \qquad P \equiv \frac{P_\parallel + 2P_\perp}{3}. \tag{A.6}$$

$\gamma = 5/3$ or $7/5$ for monatomic or diatomic plasma, respectively [38]. ε, $P_\parallel$, $P_\perp$, ρ, V_x, $\mathbf{V}_t$, B_x, $\mathbf{B}_t$, Q_x and η_r are the temperature anisotropy factor, pressure parallel

to the local magnetic field, pressure perpendicular to the local magnetic field, mass density, velocity of the bulk flow in the normal direction ($\hat{\mathbf{e}}_x$), velocity of the bulk flow in the tangential direction (y-z plane), normal component of the magnetic field, tangential components of the magnetic field, the heat flux in the x-direction and the magnetic resistivity (assumed constant). The first and the second term on the RHS of Eq. (A.4) are from the magnetic dissipation and the Hall term respectively.

We follow the procedure of Kennel *et al.* [52]. We ignore the resistivity and dispersion terms in our derivation first; they will be added back in the end. Using Lagrangian mass spatial coordinates,

$$\frac{d}{dt} \rightarrow \partial_t, \qquad x' \equiv \int \frac{\rho}{\rho_0} dx, \tag{A.7}$$

and definitions $U \equiv \rho_0/\rho$, $\mathbf{b}_T \equiv \mathbf{B}_t/B_x$ and $C_{An}^2 \equiv B_x^2/(\mu_0\rho_0)$, then Eq.(A.1) to (A.4) (without the resistivity and dispersion) become

$$\partial_t U = \partial_{x'} V_x, \tag{A.8}$$

$$\partial_t V_x + \partial_{x'}\left[\frac{P}{\rho_0} + \frac{1}{3}\left(\varepsilon + \frac{1}{2}\right) C_{An}^2 b_T^2\right] - \frac{2}{3} C_{An}^2 \partial_{x'}\varepsilon = 0, \tag{A.9}$$

$$\partial_t \mathbf{V}_t - \varepsilon C_{An}^2 \partial_{x'} \mathbf{b}_T - C_{An}^2 \mathbf{b}_T \partial_{x'}\varepsilon = 0, \tag{A.10}$$

$$\partial_t \mathbf{b}_T + \frac{\mathbf{b}_T}{U}\partial_{x'} V_x - \frac{1}{U}\partial_{x'} \mathbf{V}_t = 0. \tag{A.11}$$

Combined with Eq.(A.8) and (A.11), Eq.(A.5) becomes

$$\begin{aligned} \frac{U}{\rho_0}\partial_t P = &- \left\{ \frac{\gamma P}{\rho_0} + (\gamma - 1)\left[\frac{2}{3}(1-\varepsilon)C_{An}^2 + \frac{1}{3}(\varepsilon - 1) C_{An}^2 b_T^2\right]\right\} \partial_t U \\ &- (\gamma - 1)(1-\varepsilon) C_{An}^2 b_T \partial_t (U b_T) - \frac{\gamma - 1}{\rho_0}\partial_{x'} Q_x. \end{aligned} \tag{A.12}$$

By $\partial_{x'}$(Eq.(A.9)), we obtain

$$\partial_t^2 U + \partial_{x'}^2\left[\frac{P}{\rho_0} + \frac{1}{3}\left(\varepsilon + \frac{1}{2}\right) C_{An}^2 b_T^2\right] - \frac{2}{3} C_{An}^2 \partial_{x'}^2 \varepsilon = 0. \tag{A.13}$$

By $\partial_{x'}$(Eq.(A.10))+∂_t(U Eq.(A.11)), we obtain

$$\partial_t^2(U\mathbf{b}_T) - C_{An}^2\partial_{x'}^2(\varepsilon\mathbf{b}_T) = 0. \tag{A.14}$$

Jumping to the upstream (subscripted by "0") intermediate frame in order to separate the slow and fast variations, we take

$$\tau \equiv \sqrt{\varepsilon_0}C_{An}t, \qquad \eta \equiv x' - \sqrt{\varepsilon_0}C_{An}t, \tag{A.15}$$

with the approximation $\partial_\tau \ll \partial_\eta$ to separate slow and fast variation. Then

$$\partial_{x'} = \partial_\eta, \qquad \partial_t = -\sqrt{\varepsilon_0}C_{An}(\partial_\eta - \partial_\tau), \qquad \partial_t^2 = \varepsilon_0 C_{An}^2(\partial_\eta^2 - 2\partial_\eta\partial_\tau). \tag{A.16}$$

By substituting Eq.(A.16) into Eq.(A.12) and assuming $\delta b_T^2 \ll b_{T0}^2$, $\delta\varepsilon \ll \varepsilon_0$, $\delta U \ll U_0$ and $\delta P \ll P_0$ (where δ means variation), $\int d\eta$ once, we obtain

$$\begin{aligned}\frac{\delta P}{\rho_0} = &-\left[\frac{\gamma P_0}{\rho_0} + (\gamma-1)\frac{2}{3}(1-\varepsilon_0)(1+b_{T0}^2)C_{An}^2\right]\delta U \\ &-\frac{1}{2}(\gamma-1)(1-\varepsilon_0)C_{An}^2\delta b_T^2 + \frac{\gamma-1}{\rho_0\sqrt{\varepsilon_0}C_{An}}\delta Q_x.\end{aligned} \tag{A.17}$$

By substituting Eq.(A.16) into Eq.(A.13), $\int d\eta$ twice, then assuming $\delta b_T^2 \ll b_{T0}^2$, we obtain

$$\varepsilon_0 C_{An}^2\delta U + \frac{\delta P}{\rho_0} + \frac{1}{3}C_{An}^2\left(\varepsilon_0 + \frac{1}{2}\right)\delta b_T^2 + \frac{1}{3}C_{An}^2 b_{T0}^2\delta\varepsilon - \frac{2}{3}C_{An}^2\delta\varepsilon = 0. \tag{A.18}$$

By substituting Eq.(A.16) into Eq.(A.14), assuming $\delta U \ll U_0$, then $\int d\eta$ once, we obtain

$$\partial_\eta(\delta U\mathbf{b}_T) - \partial_\eta\left(\frac{\delta\varepsilon}{\varepsilon_0}\mathbf{b}_T\right) - 2\partial_\tau\mathbf{b}_T = 0. \tag{A.19}$$

By combining Eq.(A.17),(A.18) and (A.19) and adding the resistivity and dispersion back, we finally arrive at,

$$\partial_\tau\mathbf{b}_t + \partial_\eta[\alpha\mathbf{b}_t(b_t^2 - b_{t0}^2) + \Omega\mathbf{b}_t(\varepsilon-\varepsilon_0) + \Lambda\mathbf{b}_t(\bar{Q}_x - \bar{Q}_{x0})] = \partial_\eta(R\partial_\eta\mathbf{b}_t) - \frac{1}{2\sqrt{\varepsilon_0}}d_i\partial_\eta^2(\hat{\mathbf{x}}\times\mathbf{b}_t) \tag{A.20}$$

with

$$\alpha \equiv \frac{[(3\gamma-1)\varepsilon_0-(3\gamma-4)]C_{An}^2}{12[(\varepsilon_0-A)C_{An}^2-C_S^2]}, \qquad \Omega \equiv \frac{(b_{t0}^2-2)C_{An}^2}{6[(\varepsilon_0-A)C_{An}^2-C_S^2]}+\frac{1}{2\varepsilon_0}, \tag{A.21}$$

$$\Lambda \equiv \frac{(\gamma-1)C_{An}^2}{2\sqrt{\varepsilon_0}[(\varepsilon_0-A)C_{An}^2-C_S^2]}, \qquad A \equiv \frac{2}{3}(\gamma-1)(1-\varepsilon_0)(1+b_{t0}^2), \tag{A.22}$$

where $C_S^2 \equiv \gamma P_0/\rho_0$, $R \equiv \eta_r/(2\sqrt{\varepsilon_0}C_{An})$, $d_i \equiv \sqrt{m_i/(\mu_0 n e^2)}$ and $\bar{Q}_x \equiv Q_x/(\rho_0 C_{An}^3)$. In summary, the approximations used are:

$$\partial_\tau \ll \partial_\eta; \qquad \delta b_t^2 \ll b_{t0}^2; \qquad \delta\varepsilon \ll \varepsilon_0; \qquad \delta\rho \ll \rho_0; \qquad \delta P \ll P_0. \tag{A.23}$$

Since the heat flux Q_x is approximately proportional to $\nabla|B|$ (as pointed out in Fig. 2.2(a)), it should enter the source term on the RHS as $-\Lambda\partial_\eta^2|b_t|$. In plasmas with $\beta_n > 1$, Λ is negative and hence the heat flux helps shocks dissipate energy. We implicitly incorporate it into the resistivity R (as, for instance, is done for the shear and longitudinal viscosities discussed in [52]). We then arrive at the anisotropic DNLSB equation, Eq. (3.1). This equation can also be derived from regular reductive perturbation methods with a proper ordering scheme. For instance, a DNLS equation with the CGL condition and more corrections, including finite ion Larmor radius effects and electron pressure, was derived using regular reductive perturbation methods [54].

A.2 Non-Steepening and Non-Spreading of the Intermediate Mode

Beginning with the anisotropic MHD equations in Lagrangian form in Appendix A.1, we neglect the dissipation and the Hall term on the RHS of Eq. (A.4). Then the simple wave solution can be obtained by substituting $d/dt \to -C\delta$,

$\partial_x \rightarrow \hat{\mathbf{x}}\delta$, where C is the wave speed and δ means variation. [48]

$$-C\delta\rho + \rho\delta V_x = 0 \tag{A.24}$$

$$-C\rho\delta V_x + \delta P_\perp - \frac{B_x^2}{\mu_0}\delta\varepsilon + \frac{B_z}{\mu_0}\delta B_z = 0 \tag{A.25}$$

$$-C\rho\delta V_z - \varepsilon\frac{B_x}{\mu_0}\delta B_z - \frac{B_x B_z}{\mu_0}\delta\varepsilon = 0 \tag{A.26}$$

$$-C\rho\delta V_y - \varepsilon\frac{B_x}{\mu_0}\delta B_y = 0 \tag{A.27}$$

$$-C\delta B_z + B_z\delta V_x - B_x\delta V_z = 0 \tag{A.28}$$

$$-C\delta B_y - B_x\delta V_y = 0 \tag{A.29}$$

Eq. (A.27) and Eq. (A.29) give us the intermediate speed $C_I = \sqrt{\varepsilon}B_x/\sqrt{\mu_0\rho}$. Combined with Eq. (A.24), the steepening tendency of an intermediate mode can then be expressed as,

$$\delta(C_I + V_x) = \frac{C_I}{2}\left(\frac{\delta\rho}{\rho} + \frac{\delta\varepsilon}{\varepsilon}\right) \tag{A.30}$$

Using Eqs. (A.24), (A.25), (A.26) and (A.28), we get $\delta(C_I + V_x) = 0$. Therefore, the intermediate mode in anisotropic MHD does not steepen or spread, no matter what energy closure is used. It is linearly degenerate, as is its counterpart in isotropic MHD.

A.3 The Integral Curves and Hugoniot Locus

To find the integral curves, we follow the eigenvector of the slow mode to form a curve,

$$\frac{db_z}{d\zeta} = b_z, \qquad \frac{db_y}{d\zeta} = b_y, \tag{A.31}$$

where ζ is a dummy variable. The integral curve is $b_y = (b_{y0}/b_{z0})b_z$.

For the intermediate mode,

$$\frac{db_z}{d\zeta} = b_y, \qquad \frac{db_y}{d\zeta} = -b_z. \tag{A.32}$$

Therefore, the integral curve is $b_t^2 = b_{t0}^2$.

As to the Hugoniot locus, we need to compute the shock speed $S = (f_i(\mathbf{q}) - f_i(\mathbf{q}_0))/(q_i - q_{0i})$ where f_i is the flux of Eq. (3.6) and $i = 1$ or 2.

$$\begin{aligned} S(b_z - b_{z0}) &= \alpha b_z(b_t^2 - b_{t0}^2) + \Omega b_z \delta\varepsilon \\ S(b_y - b_{y0}) &= \alpha b_y(b_t^2 - b_{t0}^2) + \Omega b_y \delta\varepsilon \end{aligned} \tag{A.33}$$

These can be combined to give,

$$(b_{z0}b_y - b_{y0}b_z)[\alpha(b_t^2 - b_{t0}^2) + \Omega\delta\varepsilon] = 0. \tag{A.34}$$

The first root is the Hugoniot locus of the slow mode: $b_y = (b_{y0}/b_{z0})b_z$. For $\varepsilon(b_t)$, so that $\delta\varepsilon \simeq [\partial(\delta\varepsilon)/\partial(b_t^2)](b_t^2 - b_{t0}^2)$, the second root gives us the Hugoniot locus of the intermediate mode: $b_t^2 = b_{t0}^2$. Although these results are the same as derived from the integral curves, this is not generally the case.

A.4 The Pseudo-Potential of Anisotropic MHD (AMHD)

In the de Hoffmann-Teller frame, the jump conditions can be written as (following Hau and Sonnerup's procedure [39, 40]),

$$[\rho V_x]^0 = 0 \tag{A.35}$$

$$\left[\rho V_x^2 + P + \frac{1}{3}\left(\varepsilon + \frac{1}{2}\right)\frac{B^2}{\mu_0} - \varepsilon\frac{B_x^2}{\mu_0}\right]^0 = 0 \tag{A.36}$$

$$\left[\rho V_x \mathbf{V}_t - \varepsilon \frac{B_x \mathbf{B}_t}{\mu_0}\right]^0 = 0 \tag{A.37}$$

$$\left[\left(\frac{1}{2}\rho V^2 + \frac{\gamma}{\gamma-1}P + \frac{1}{3}(\varepsilon-1)\frac{B^2}{\mu_0}\right)V_x - (\varepsilon-1)\frac{B_x \mathbf{B}_t}{\mu_0}\cdot\mathbf{V}_t - (\varepsilon-1)\frac{B_x^2}{\mu_0}V_x\right]^0 = 0 \tag{A.38}$$

where we define a jump relation $[Q]^0 \equiv Q_0 - Q$, with Q_0 the upstream value and Q the value inside the transition region. $\gamma = 5/3$ or $7/5$ for monatomic or diatomic plasma, respectively. From Eq. (A.35)-(A.38), we can derive

$$A_x^2 \equiv \frac{V_x^2}{B_x^2/(\mu_0\rho)} = \frac{-b \pm \sqrt{b^2-4ac}}{2a} \tag{A.39}$$

where

$$a = 1 - \frac{\gamma-1}{2\gamma}, \tag{A.40}$$

$$\begin{aligned} b = &- A_{x0}^2 - \left[\frac{\beta_0}{2} + \frac{1}{3}\left(\varepsilon_0 + \frac{1}{2}\right)\right]\sec^2\theta_0 + \varepsilon_0 + \frac{1}{3}\left(\varepsilon + \frac{1}{2}\right)\frac{B^2}{B_x^2} \\ &- \varepsilon + \frac{2\gamma-2}{3\gamma}(\varepsilon-1) - \frac{\gamma-1}{3\gamma}(\varepsilon-1)\frac{B_t^2}{B_x^2}, \end{aligned} \tag{A.41}$$

$$\begin{aligned} c = &\frac{\gamma-1}{2\gamma}\sec^2\theta_0 A_{x0}^4 + \left[\frac{\beta_0}{2} - \frac{2\gamma-2}{3\gamma}(\varepsilon_0-1)\right]\sec^2\theta_0 A_{x0}^2 \\ &- \frac{\gamma-1}{2\gamma}\left[(A_{x0}^2-\varepsilon_0)\tan\theta_0 + \varepsilon\frac{B_t}{B_x}\right]^2 \\ &+ \frac{\gamma-1}{\gamma}(\varepsilon-1)\frac{B_t}{B_x}\left[(A_{x0}^2-\varepsilon_0)\tan\theta_0 + \varepsilon\frac{B_t}{B_x}\right] \end{aligned} \tag{A.42}$$

with $\cos\theta_0 \equiv B_x/B_0$.

The generalized Ohm's law is

$$\mathbf{E} + \mathbf{V}\times\mathbf{B} = \eta_r \mathbf{J} + \frac{1}{ne}(\mathbf{J}\times\mathbf{B}), \tag{A.43}$$

where the first and the second terms on the RHS are the magnetic dissipation and

the Hall term respectively. With the final jump condition $[E_t]^0 = 0$, we obtain

$$\frac{A_{x0}}{h_0} d_{i0}(1+h^2)\frac{dB_y}{dx} = (A_x^2-\varepsilon)(B_y-hB_z)+(A_{x0}^2-\varepsilon_0)(hB_{z0}-B_{y0}) \equiv F_{y,\mathrm{AMHD}} \equiv \frac{\partial \Psi_{\mathrm{AMHD}}}{\partial B_y} \tag{A.44}$$

$$\frac{A_{x0}}{h_0} d_{i0}(1+h^2)\frac{dB_z}{dx} = (A_x^2-\varepsilon)(B_z+hB_y)-(A_{x0}^2-\varepsilon_0)(hB_{y0}+B_{z0}) \equiv F_{z,\mathrm{AMHD}} \equiv \frac{\partial \Psi_{\mathrm{AMHD}}}{\partial B_z} \tag{A.45}$$

where $h \equiv B_x/ne\eta_r$ measures the ratio of the dispersion to the resistivity. The pseudo-potential Ψ_{AMHD} is uniquely defined since $\partial F_{z,\mathrm{AMHD}}/\partial B_y = \partial F_{y,\mathrm{AMHD}}/\partial B_z$.

A.4.1: Fig. A.1(a) shows the pseudo-potential of AMHD for the same parameters as Fig. 3.3(a) (which was calculated based on the reduced ADNLSB formulation). If $V_S = 0$ then $A_{x0}^2 = \varepsilon_0$, and thus the potential minimum (where $F_{z,\mathrm{AMHD}} = 0$) occurs at $A_x^2 = \varepsilon$. This implies that in the shock frame (also the upstream intermediate frame), $\lambda_{I,\mathrm{AMHD}} = -V_x + C_I = (-A_x + \sqrt{\varepsilon})B_x/\sqrt{\mu_0\rho} = 0$ at the potential minimum. This is essentially the same point $\mathbf{q}_m$ (where $\lambda_I = 0$) of Fig. 3.3(d) with ADNLSB. Fig. A.1(b) shows a similar reversal with the CGL closure. We note that the CGL closure exhibits an even stronger tendency to reverse the pseudo-potential. In Fig. A.1(c), the pseudo-potential for $\theta_{BN} = 75°$, $\beta_0 = 0.4$ and $c_2 = 0.2$ is shown, these parameters are more similar to those seen in our PIC simulation.

A.4.2: Now we consider the jump conditions to an asymptotic downstream by neglecting the LHS and terms with h of Eqs. (A.44) and (A.45). The relation $B_{t,d}/B_x = \tan\theta_0(A_{x0}^2 - \varepsilon_0)/(A_{x,d}^2 - \varepsilon_d)$ can be derived where we label quantities $Q \rightarrow Q_d$ ("d" for downstream). We can eventually invert A_{x0}^2 as a function of

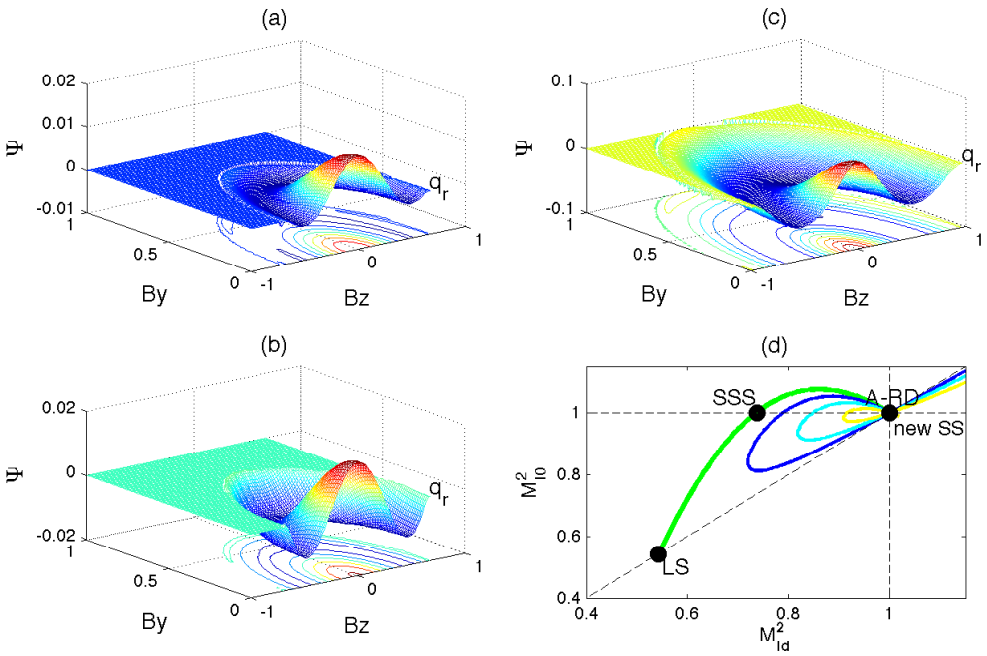

Figure A.1: Results with fully anisotropic MHD. Panel (a) is the pseudo-potential Ψ with our closure, Eq. (3.15). Upstream (point $\mathbf{q}_r$), $V_S = 0$, $\theta_0 = 42°$, $\beta_0 = 1$, $\varepsilon_0 = 1$ and $c_2 = 0.5$; Panel (b) is Ψ with the CGL closure. Upstream (point $\mathbf{q}_r$), $V_S = 0$, $\theta_0 = 42°$, $\beta_0 = 1$ and $\varepsilon_0 = 1.5$; Panel (c) is Ψ for $V_S = 0$, $\theta_0 = 75°$, $\beta_0 = 0.4$, $\varepsilon_0 = 1$, and $c_2 = 0.2$ with our closure; Panel (d) is the shock curve with upstream parameters $\theta_0 = 42°$, $\beta_0 = 1$ and $\varepsilon_0 = 1$. In the green curve ($\varepsilon_d = \varepsilon_0$ case), the portion from A-RD (anisotropic-RD) to SSS is the IS branch, from SSS to LS (linear slow mode) is the SS branch. Different curves represent cases with different ε_d of values 1, 0.95, 0.9, 0.85 (from outer curve to inner curve). Other than the A-RD, a new SS exists at (1,1) when $\varepsilon_d < \varepsilon_0$. Both the IS and SS branches shrink toward the point (1,1) as ε_d decreases.

$A^2_{x,d}$ from Eq. (A.39). The result is plotted in Fig. A.1(d) which shows possible shock solutions as functions of the downstream intermediate Mach number $M^2_{I,d} \equiv V^2_{x,d}/C^2_{I,d} = A^2_{x,d}/\varepsilon_d$ [50]. In the green curve ($\varepsilon_d = \varepsilon_0$ case), the portion from A-RD (anisotropic-RD) to SSS is the IS branch, from SSS to LS (linear slow mode) is the SS branch. When $\varepsilon_d < \varepsilon_0$, a new slow-shock transition from $A^2_{x0} = \varepsilon_0 > 0.25$ to $A^2_{x,d} = \varepsilon_d$ is noted at the point (1,1). This new SS constitutes the slow shock portion of a compound SS/RD wave. For a given ε_0, the smallest possible $\varepsilon_{d,\min}$ shrinks the SS and IS branches to the point (1,1). It can be shown that $\varepsilon_{d,\min} > 0.25$ is always true for $\varepsilon_0 > 0.25$. Therefore the existence of the new slow shock requires $\varepsilon_d > 0.25$. In other words, $\varepsilon_0 > \varepsilon_m (= \varepsilon_d) > 0.25$ is always true for a SS/RD compound wave in full anisotropic MHD.

A.4.3: From Fig. A.1(d) and further investigations, it can be shown that the anisotropic-RD(A-RD) at (1,1) has the same jump as that of the new SS at (1,1) plus a RD that does not change ε and thermal states. Therefore an A-RD and the corresponding compound SS/RD wave have the same jump relations.

A.5 The Equal-Area Rule and Intermediate Shocks

The equal-area rule applies to conserved quantities in hyperbolic equations, which in our case is b_z. From Eq. (3.6) and the general form of Eq. (3.20), we find a simple relation between the pseudo-force and the flux function,

$$F_z|_{b_y=0} = -\alpha b_z(b_z^2 - b_{z0}^2) - \Omega b_z \delta\varepsilon(b_z, b_y) + V_S(b_z - b_{z0}) = -f_1|_{b_y=0} + V_S(b_z - b_{z0}) \quad \text{(A.46)}$$

From Eq. (3.6) and Eq. (3.8), a simple relation between the slow characteristic

and the flux function is

$$\lambda_{SL}|_{b_y=0} = \frac{\partial f_1}{\partial b_z}\Big|_{b_y=0}, \tag{A.47}$$

It is then easy to show that,

$$\int_{b_{z0}}^{b_z} (\lambda_{SL}|_{b_y=0} - V_S) db_z = -F_z|_{b_y=0} \tag{A.48}$$

This indicates that a stationary point b_z, where $F_z = 0$, will be located where the integral on the LHS is zero. This is called the equal-area rule. From this relation, with a given b_{z0} and b_z, we can determine the shock speed V_S that causes the integral to vanish. Or for a given b_{z0} and V_S, we can determine the possible downstream state b_z. We apply it to the following examples to demonstrate the formation of intermediate shocks (which have a super-intermediate to sub-intermediate transition) in isotropic MHD.

When the upstream $\mathbf{q}_r = (b_{z0}, 0)$ is given and fixed, we can vary $\mathbf{q}_l = (b_z, 0)$ to see the effect on possible shock solutions. In Fig. A.2(a), when $\mathbf{q}_l$ is chosen above $b_z = 0$, a slow shock solution is found by determining a proper horizontal line ($\mathbf{q}_r - \mathbf{q}_l$; note that the vertical position measures the shock speed V_S), which makes the red area below the line $\mathbf{q}_r - \mathbf{q}_l$ equal the red area above. The shock speed is slower than the upstream intermediate speed (black horizontal line across 0), the upstream (point $\mathbf{q}_r$) is super-slow and sub-intermediate ($V_S > \lambda_{SL}|_{\mathbf{q}_r}$, $V_S < \lambda_I|_{\mathbf{q}_r}$. Since λ is equivalent to $C - u$ where C is the phase speed and u is the bulk flow speed measured in upstream intermediate frame, $V_S \gtrless \lambda$ implies that the Mach number measured in shock frame $M \equiv (V_S + u)/C \gtrless 1$) and the downstream (point $\mathbf{q}_l$) is sub-slow ($V_S < \lambda_{SL}|_{\mathbf{q}_l}$). Traditionally in isotropic MHD, the super-fast state is

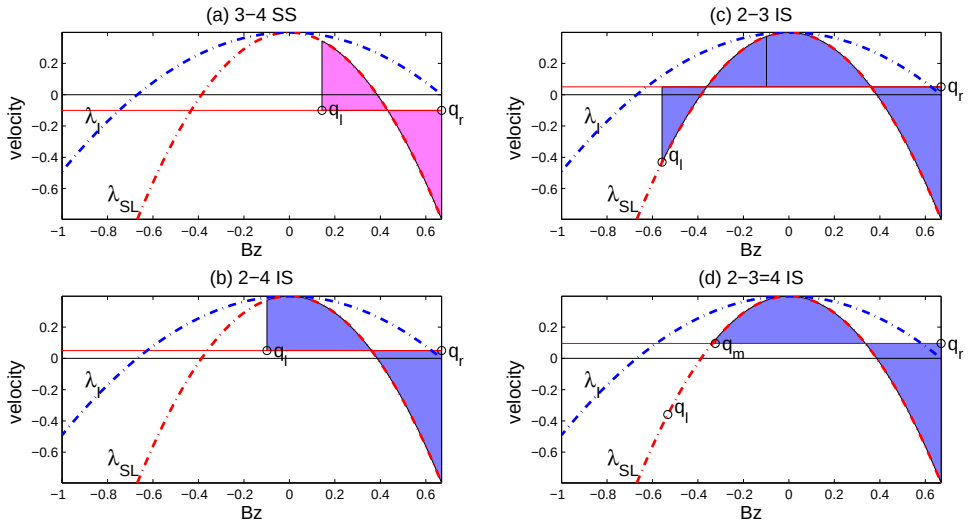

Figure A.2: Application of equal-area rules with cases in ideal (isotropic) MHD. The λ_I and λ_{SL} along b_z are measured in the upstream intermediate frame with upstream (point $\mathbf{q}_r$) parameters, $\theta_0 = 42°, \beta_0 = 1, \varepsilon_0 = 1$. The vertical axis measures speed (normalized to C_{An}). Once the $\mathbf{q}_l$ is chosen, the shock speed V_S (measured by the red horizontal line) can be determined by equating area (between the λ_{SL} and the red line) above the red line to area below the red line. This rule results in shock speeds (a) $V_S = -0.1$; (b) $V_S = 0.05$; (c) $V_S = 0.05$; (d) $V_S = 0.0958$.

termed number 1, sub-fast and super-intermediate is 2, sub-intermediate and super-slow is 3, and sub-slow is 4. Therefore a slow shock is also called a 3-4 SS (as mentioned in Sec. 1.4.1).

In Fig. A.2 (b), if $\mathbf{q}_l$ is chosen below the point $b_z = 0$, a 2-4 intermediate shock ($\mathbf{q}_r - \mathbf{q}_l$) is formed, with upstream being super-intermediate and downstream being sub-intermediate and sub-slow. In Fig. A.2(c), with the same shock speed, a 2-3 IS transitions to a $\mathbf{q}_l$ with a more negative value is also possible. Note that the jump cross a compound 2-3 IS/ 3-4 SS (from this $\mathbf{q}_l$ to the $\mathbf{q}_l$ in (b)) equals to that of the 2-4 IS in (b). In Fig. A.2(d), with the same $\mathbf{q}_l$ of Fig. A.2(c), a 2-3=4 IS ($\mathbf{q}_r - \mathbf{q}_m$) with the maximum IS speed could be formed and attached by a slow rarefaction ($\mathbf{q}_m - \mathbf{q}_l$). This is a compound IS/SR wave, with $b_z|_{\mathbf{q}_m} = -b_{z0}/2$ which can also be determined by $\lambda_{SL}(b_z|_{\mathbf{q}_m}) = [f_1(b_{z0}) - f_1(b_z|_{\mathbf{q}_m})]/(b_{z0} - b_z|_{\mathbf{q}_m})$, as shown by Brio and Wu [12]. Similar arguments can be made in a system with fast and intermediate modes.

Therefore, an intermediate shock is not directly associated with an intermediate mode. It is steepened by magneto-sonic waves (slow or fast modes), not by intermediate mode itself. This was first justified by Wu's (1987) coplanar simulations [119] (*i.e.,* no out-of-plane magnetic field is allowed), where the intermediate shock forms even though the intermediate mode is not included (since the out-of-plane δB_y is necessary for nontrivial solutions of the intermediate mode, as shown in Appendix A.2). The coupling of intermediate and magneto-sonic waves and the admissibility of intermediate shocks in the ideal MHD system was discussed by Kennel *et al.* [52].

Bibliography

[1] B. Abraham-Shrauner. Propagation of hydromagnetic waves through an anisotropic plasma. *J. Plasma. Phys.*, 1:361–378, 1967.

[2] V. Angelopoulos, J. P. McFadden, D. Larson, and et al. Tail reconnection triggering substorm onset. *Science*, 321:931–935, 2008.

[3] M. Aschwanden. *Physics of the Solar Corona*. Springer, 2005.

[4] S.D. Bale, J.C. Kasper, G. G. Howes, E. Quataert, C. Salem, and D. Sundkvist. Magnetic fluctuation power near proton temperature anisotropy instability thresholds in the solar wind. *Phys. Rev. Lett.*, 103:211101, 2009.

[5] A. Barnes and J. V. Hollweg. Large-amplitude hydromagnetic waves. *J. Geophys. Res.*, 79(16):2302–2318, 1974.

[6] K. Beckwith, J. F. Hawley, and J. H. Krolik. The influence of magnetic field geometry on the evolution of black hole accretion flows: similar disks, drastically different jets. *Astrophys. J.*, 678:1180–1199, 2008.

[7] A. R. Bell. The acceleration of cosmic rays in shock fronts-i. *Mon. Not. R. astr. Soc.*, 182:147–156, 1978.

[8] J. Birn, J. F. Drake, M. A. Shay, B. N. Rogers, R. E. Dention, M. Hesse, M. Kuznetsova, Z. W. Ma, A. Bhattacharjee, A. Otto, and P. L. Pritchett. Geospace Environmental Modeling (GEM) magnetic reconnection challenge. *J. Geophys. Res.*, 106(A3):3715–3719, 2001.

[9] D. Biskamp. Magnetic reconnection via current sheets. *Phys. Fluids*, 29:1520, 1986.

[10] R. D. Blandford and D. G. Payne. Hydromagnetic flows from accretion discs and the production of radio jets. *Mon. Not. R. Astron. Soc.*, 199:883–903, 1982.

[11] R. D. Blandford and R. L. Znajek. Electromagnetic extraction of energy from kerr black holes. *Mon. Not. R. Astron. Soc.*, 179:443–456, 1977.

[12] M. Brio and C. C. Wu. An upwind differencing scheme for the equations of magnetohydrodynamics. *J. Comp. Physics*, 75:400–422, 1988.

[13] P. A. Cassak, M. A. Shay, and J. F. Drake. Catastrophe model for fast magnetic reconnection onset. *Phys. Rev. Lett.*, 95:235002, 2005.

[14] J. K. Chao. Interplanetary collisionless shock waves. *Rep. CSR TR-70-s, Mass. Inst. of Technology. Cent. for Space Res., Cambridge, Mass.*, 1970.

[15] H. Che, J. F. Drake, M. Swisdak, and P. H. Yoon. Electron holes and heating in the reconnection dissipation region. *Geophys. Res. Lett.*, 37:L11105, 2010.

[16] C. F. Chew, M. L. Goldberger, and F. E. Low. The boltzmann equation and the one-fluid hydromagnetic equations in the absence of particle collisions. *Proc. Roy. Soc. London Ser. A*, 236(1204):112–118, 1956.

[17] F. V. Coroniti. Laminar wave-train structure of collisionless magnetic slow shocks. *Nucl. Fusion*, 11:261–283, 1971.

[18] F. V. Coroniti. Magnetically striped relativistic magnetohydrodynamic winds: The crab nebula revisited. *Astrophys. J.*, 349:538–545, 1990.

[19] M. Cremer and M. Scholer. Collisionless slow shocks in magnetotail reconnectionr. *Geophys. Res. Lett.*, 26(17):2709–2712, 1999.

[20] M. Cremer and M. Scholer. Structure of the reconnection layer and the associated slow shocks: Two-dimensional simulations of a riemann problem. *J. Geophys. Res.*, 105(A12):27621–27632, 2000.

[21] W. Daughton and S. P. Gary. Electromagnetic proton/proton instabilities in the solar wind. *J. Geophys. Res.*, 103(A9):20613–20620, 1998.

[22] W. Daughton, D. Winske, L. Yin, and S. P. Gary. Role of electron physics in slow mode shocks. *J. Geophys. Res.*, 106(A11):25031–25039, 2001.

[23] Ronald C. Davidson and Heinrich J. Volk. Macroscopic quasilinear theory of the garden-hose instability. *Physics of Fluids*, 11(10):2259, 1968.

[24] R. B. Decker. Computer modeling of test particle acceleration at oblique shocks. *Space Science Reviews*, 48:195–262, 1988.

[25] J. B. Dove, J. Wilms, and M. C. Begelman. Self-consistent thermal accretion disk corona models for compact objects: I. properties of the corona and the spectrum of escaping radiation. *Astrophys. J.*, 999:L1–L4, 2000.

[26] J. F. Drake, M. Opher, M. Swisdak, and J. N. Chamoun. A magnetic reconnection mechanism for the generation of cosmic rays. *Astrophys. J.*, 709:963–974, 2009.

[27] J. F. Drake, M. Swisdak, H. Che, and M. A. Shay. Electron acceleration from contracting magnetic islands during reconnection. *Nature*, 442:553–556, 2006.

[28] J. F. Drake, M. Swisdak, T. D Phan, P. A. Cassak, M. A. Shay, S. T. Lepri, R. P. Lin, E. Quataert, and T. H. Zurbuchen. Ion heating resulting from pickup in magnetic reconnection exhausts. *J. Geophys. Res.*, 114(A):05111–05124, 2009.

[29] J. F. Drake, M. Swisdak, M. A. Shay, B. N. Rogers, A. Zeiler, and C. Cattell. Formation of electron holes and particle energization during magnetic reconnection. *Science*, 299:873, 2003.

[30] J. W. Dungey. Conditions for the occurrence of electrical discharges in astrophysical systems. *Phil. Mag.*, 44:725, 1953.

[31] J. W. Dungey. *Cosmic Electrodynamics*. Cambridge University Press, 1958.

[32] W. C. Feldman, S. J. Schwartz, S. J. Bame, D. N. Baker, J. T. Gosling, Jr. E. W. Hones, D. J. McComas, J. A. Slavin, E. J. Smith, and R. D. Zwickl. Evidence for slow-mode shocks in the deep geomagnetic tail. *Geophys. Res. Lett.*, 11(6):599–602, 1984.

[33] W. C. Feldman, R. L. Tokar, J. Birn, Jr. E. W. Hones, S. J. Bame, and C. T. Russell. Structure of a slow mode shock observed in the plasma sheet boundary layer. *J. Geophys. Res.*, 92(A1):83–94, 1987.

[34] L. A. Fisk, G. Gloeckler, and T. H. Zurbuchen. Acceleration of low-energy ions at the termination shock of the solar wind. *Astrophys. J.*, 644:631–637, 2006.

[35] S. Von Geoler, W. Stodiek, and N. R. Sautoff. Studies of internal disruptions and $m = 1$ oscillations in tokmak discharges with soft-x-ray techniques. *Phys. Rev. Lett.*, 33:1201, 1974.

[36] J. T. Gosling, R. M. Skoug, D. J. McComas, and C. W. Smith. Direct evidence for magnetic reconnection in the solar wind near 1 au. *J. Geophys. Res.*, 110:A01107, 2005.

[37] D. A. Gurnett and A. Bhattacharjee. *Introduction to Plasma Physics: With Space and Laboratory*. Cambridge University Press, 2005.

[38] L. -N. Hau. A note on the energy laws in gyrotropic plasmas. *Phys. Plasmas*, 9(6):2455–2457, 2002.

[39] L. -N. Hau and B. U. Ö. Sonnerup. On the structure of resistive MHD intermediate shocks. *J. Geophys. Res.*, 94(A6):6539–6551, 1989.

[40] L. -N. Hau and B. U. Ö. Sonnerup. The structure of resistive-dispersive intermediate shocks. *J. Geophys. Res.*, 95(A11):18791–18808, 1990.

[41] L. -N. Hau and B. U. Ö. Sonnerup. On slow-mode waves in an anisotropic plasma. *Geophys. Res. Lett.*, 20(17):1763–1766, 1993.

[42] M. Hoshino, T. Mukai, I Shinohara, Y. Saito, and S. Kokubun. Slow shock downstream structure in the magnetotail. *J. Geophys. Res.*, 105(A1):337–347, 2000.

[43] M. Hoshino, T. Mukai, and T. Yamamoto. Ion dynamics in magnetic reconnection: Comparison between numerical simulation and geotail observations. *J. Geophys. Res.*, 103(A3):4509–4530, 1998.

[44] J. D. Huba, N. T. Gladd, and K. Papadopoulos. The lower-hybrid-drift instability as a source of anomalous resistivity for magnetic field reconnection. *Geophys. Res. Lett.*, 4:125, 1977.

[45] P. D. Hudson. Discontinuities in an anisotropic plasma and their identification in solar wind. *Planetary and Space Science*, 18:1611–1622, 1970.

[46] P. D. Hudson. Rotational discontinuities in an anisotropic plasma. *Planetary and Space Science*, 19:1693–1699, 1971.

[47] P. D. Hudson. Shocks in an anisotropic plasma. *J. Plasma Physics*, 17:419–432, 1977.

[48] A. Jeffrey and T. Taniuti. *Non-linear wave propagation*, chapter 4, pages 167–194. Academic Press Inc., 1964.

[49] B. B. Kadomtsev. Disruptive instability in tokamaks. *Sov. J. Plasma Phys.*, 1:389–391, 1975.

[50] H. Karimabadi, D. Krauss-Varban, and N. Omidi. Temperature anisotropy effects and the generation of anomalous slow shocks. *Geophys. Res. Lett.*, 22(20):2689–2692, 1995.

[51] C. F. Kennel. Shock structure in classical magnetohydrodynamics. *J. Geophys. Res.*, 93(A8):8545–8557, 1988.

[52] C. F. Kennel, R. D. Blandford, and C. C. Wu. Structure and evolution of small-amplitude intermediate shock waves. *Phys. Fluids B*, 2(2):253–269, 1990.

[53] C. F. Kennel, B. Buti, T. Hada, and R. Pellat. Nonlinear, dispersive,elliptically polarized alfven waves. *Phys. Fluids*, 31(7):1949–1961, 1988.

[54] M. Khanna and R. Rajaram. Evolution of nonlinear alfven waves propagating along the magnetic field in a collisionless plasma. *J. Plasma. Phys.*, 28:459–468, 1982.

[55] M. G. Kivelson and C. T. Russell. *Introduction to Space Physics*. Cambridge University Press, 1995.

[56] D. Krauss-Varban and N. Omidi. Large-scale hybrid simulations of magnetotail during reconnection. *Geophys. Res. Lett.*, 22(23):3271–3274, 1995.

[57] D. Krauss-Varban, N. Omidi, and K. B. Quest. Mode properties of low-frequency waves: Kinetic theory versus Hall-MHD. *J. Geophys. Res.*, 99(A4):5987–6009, 1994.

[58] E. A. Lazarus, F. L. Waelbroeck, T. C. Luce, M. E. Austin, K. H. Burrell, J. R. Ferron, A. W. Hyatt, T. H. Osborne, M. S. Chu, D. P. Brennan, P. Gohil, R. J. Groebner, C. L. Hsieh, R. J. Jayakumar, L. L. Lao, J. Lohr, M. A. Makowski, C. C. Petty, P. A. Politzer, R. Prater, T. L. Rhodes, J. T. Scoville, E. J. Strait, A. D. Turnbull, M. R. Wade, G. Wang, H. Reimerdes, and C. Zhang. A comparison of sawtooth oscillations in bean and oval shaped plasmas. *Plasma Phys. Control. Fusion*, 48:L65–L72, 2006.

[59] L. C. Lee, B. H. Wu, J. K. Chao, C. H. Lin, and Y. Li. Formation of a compound slow shock-rotational discontinuity structure. *J. Geophys. Res.*, 105(A6):13045–13053, 2000.

[60] M. A. Lee. Coupled hydromagnetic wave excitation and ion acceleration upstream of earth's bow shock. *J. Geophys. Res.*, 87(A7):5063–5080, 1982.

[61] Randall J. Leveque. *Finite Volume Methods for Hyperbolic Problems*, chapter 13. Press Syndicate of the U. of Cambridge, 2002.

[62] R. H. Levy, H. E. Petschek, and G. L. Siscoe. Aerodynamic aspects of magnetospheric flow. *AIAA J.*, 2:2065, 1964.

[63] J. Lin, W. Soon, and S. L. Baliunas. Theories of solar eruptions: a review. *New Astron. Rev.*, 47:53–84, 2003.

[64] R. P. Lin, R. A. Schwartz, S. R. Kane, R. M. Pelling, and K. C. Hurley. Solar hard x-ray microflares. *Astrophys. J.*, 283:421–425, 1984.

[65] Y. Lin and L. C. Lee. Structure of reconnection layers in the magnetosphere. *Space Science Reviews*, 65:59–179, 1993.

[66] Y. Lin and D. W. Swift. A two-dimensional hybrid simulation of the magnetotail reconnection layer. *J. Geophys. Res.*, 101(A9):19859–19870, 1996.

[67] Yi-Hsin Liu, J. F. Drake, and M. Swisdak. The effects of strong temperature anisotropy on the kinetic structure of collisionless slow shocks and reconnection exhausts. I: PIC simulations. *In press, POP*, 2011.

[68] Yi-Hsin Liu, J. F. Drake, and M. Swisdak. The effects of strong temperature anisotropy on the kinetic structure of collisionless slow shocks and reconnection exhausts. II: Theory. *submitted to POP*, 2011.

[69] D. W. Longcope and S. J. Bradshaw. Slow shocks and conduction fronts from petscheck reconnection of skewed magnetic fields: Two-fluid effects. *Astrophys. J.*, 718:1491–1508, 2010.

[70] D. W. Longcope, S. E. Guidoni, and M. G. Linton. Gas-dynamic shock heating of post-flare loops due to retraction following localized, impulsive reconnection. *Astrophys. J.*, 690:L18–L22, 2009.

[71] R. F. Lottermoser, M. Scholer, and A. P. Matthews. Ion kinetic effects in magnetic reconnection: Hybrid simulations. *J. Geophys. Res.*, 103(A3):4547–4559, 1998.

[72] E. A. Lucek, T. S. Horbury, M. W. Dunlop, P. J. Cargill, S. I. Schwartz, A. Balogh, P. Brown, C. Carr, K. H. Fornacon, and E. Georgescu. Cluster magnetic field observations at a quasi-parallel bow shock. *Ann. Geophysicae*, 20:1699–1710, 2002.

[73] Y. Lyubarsky and J. G. Kirk. Reconnection in a striped pulsar wind. *Astrophys. J.*, 547:437–448, 2001.

[74] M. E. Mandt, R. E. Denton, and J. F. Drake. Transition to whistler mediated reconnection. *Geophys. Res. Lett.*, 21(1):73–76, 1994.

[75] J. C. McKinney and R. D. Blandford. Stability of relativistic jets from rotating, accreting black holes via fully three-dimensional magnetohydrodynamic simulations. *Mon. Not. R. Astron. Soc.*, 000:1–6, 2009.

[76] J. C. McKinney and D. A. Uzdensky. A reconnection switch to trigger gamma-ray burst jet dissipation. *Mon. Not. R. Astron. Soc.*, 000:1–43, 2010.

[77] E. Mjolhus. On the modulational instability of hydromagnetic waves parallel to the magnetic field. *J. Plasma. Phys.*, 16:321–334, 1976.

[78] M. S. Nakamura, M. Fujimoto, and K. Maezawa. Ion dynamics and resultant velocity space distributions in the course of magnetotail reconnection. *J. Geophys. Res.*, 103(A3):4531–4546, 1998.

[79] M. Øieroset, T. D. Phan, R. P. Lin, and B. U. Ö. Sonnerup. Waleń and variance analyses of high-speed flows observed by wind in the midtail plasma sheet: Evidence for reconnection. *J. Geophys. Res.*, 105(A11):25247–25263, 2000.

[80] M. Omidi and D. Winske. Steepening of kinetic magnetosonic waves into shocklets: Simulations and consequences for planetary shocks and comets. *J. Geophys. Res.*, 95(A3):2281–2300, 1990.

[81] N. Omidi and D. Winske. Kinetic structure of slow shocks: effects of the electromagnetic ion/ion cyclotron instability. *J. Geophys. Res.*, 97(A10):14801–14821, 1992.

[82] M. Opher, J. F. Drake, M. Swisdak, K. M. Schoeffler, J. D. Richardson, R. B. Decker, and G. Toh. Is the magnetic field in the heliosheath laminar or a turbulent bath of bubbles. *Astrophys. J.*, 734:71, 2011.

[83] E. N. Parker. Sweet's mechanism for merging magnetic fields in conducting fluids. *J. Geophys. Res.*, 62(4):509–520, 1957.

[84] E. N. Parker. Dynamics of the interplanetary gas and magnetic fields. *Astrophys. J.*, 128:664, 1958.

[85] E. N. Parker. Magnetic neutral sheets in evolving fields. ii. formation of the solar corona. *Astrophys. J.*, 264:642–647, 1983.

[86] E. N. Parker. Nanoflares and the solar x-ray corona. *Astrophys. J.*, 330:474–479, 1988.

[87] J. Pétri and Y. Lyubarsky. Magnetic reconnection at the termination shock in a striped pulsar wind. *AIP Conf. Proc.*, 983:207–209, 2008.

[88] Harry E. Petschek. Magnetic field annihilation. In *Proc. AAS-NASA Symp. Phys. Solar Flares*, volume 50 of *NASA-SP*, pages 425–439, 1964.

[89] T. D. Phan, J. T. Gosling, M. S. Davis, R. M. Skoug, M. Øieroset, R. P. Lin, R. P. Lepping, D. J. McComas, C. W. Smith, H. Rème, and A. Balogh. A magnetic reconnection X-line extending more than 390 Earth radii in the solar wind. *Nature*, 439:175–178, 2006.

[90] E. R. Priest and T. R. Forbes. *Magnetic Reconnection*. Cambridge University Press, 2000.

[91] E. R. Priest and T. R. Forbes. The magnetic nature of solar flares. *Astron. Astrophs. Rev.*, 10:313–377, 2002.

[92] B. N. Rogers, R. E. Denton, J. F. Drake, and M. A. Shay. Role of dispersive waves in collisionless magnetic reconnection. *Phys. Rev. Lett.*, 87(19):195004, 2001.

[93] R. Z. Sagdeev. Cooperative phenomena and shock waves in collisionless plasmas. *Reviews of Plasma Physics*, 4:23, 1966.

[94] T. Sato and T. Hayashi. Externally driven magnetic reconnection and a powerful magnetic converter. *Phys. Fluids*, 22:1189, 1979.

[95] G. Schmidt. *Physics of high temperature plasmas- an introduction*, chapter 7, pages 248–250. Academic Press Inc., 1966.

[96] M. Scholer. Undriven magnetic reconnection in an isolated current sheet. *J. Geophys. Res.*, 94(A7):8805–8812, 1989.

[97] M. Scholer. Upstream waves, shocklets, short large-amplitude magnetic structures and the cyclic behavior of oblique quasi-parallel collisionless shocks. *J. Geophys. Res.*, 98(A1):47–57, 1993.

[98] M. Scholer and R. F. Lottermoser. On the kinetic structure of the magnetotail reconnection layer. *Geophys. Res. Lett.*, 25(17):3281–3284, 1998.

[99] J. Seon, L. A. Frank, W. R. Paterson, J. D. Scudder, F. V. Coroniti, S. Kokubun, and T. Yamamoto. Observations of a slow-mode shock at the lobe-plasma sheet boundary in earth's distant magnetotail. *Geophys. Res. Lett.*, 22(21):2981–2984, 1995.

[100] J. Seon, L. A. Frank, W. R. Paterson, J. D. Scudder, F. V. Coroniti, S. Kokubun, and T. Yamamoto. Observations of slow-mode shocks in earth's distant magnetotail with the geotail spacecraft. *J. Geophys. Res.*, 101(A12):27383–27398, 1996.

[101] M. A. Shay, J. F. Drake, B. N. Rogers, and R. E. Denton. The scaling of collisionless, magnetic reconnection for large systems. *Geophys. Res. Lett.*, 26:2163–2166, 1999.

[102] M. A. Shay, J. F. Drake, and M. Swisdak. Two-scale structure of the electron dissipation region during collisionless magnetic reconnection. *Phys. Rev. Lett.*, 99:155002, 2007.

[103] E. J. Smith, J. A. Slavin, B. T. Tsurutani, W. C. Feldman, and S. J. Bame. Slow mode shocks in the earth's magnetotial: Isee-3. *Geophys. Res. Lett.*, 11(10):1054–1057, 1984.

[104] B. U. Ö. Sonnerup, G. Paschmann, I. Papamastorakis, N. Sckopke, G. Haerendel, S. J. Bame, J. R. Asbridge, J. T. Gosling, and C. T. Russell. Evidence for magnetic reconnection at the earth's magnetopause. *J. Geophys. Res.*, 86(A12):10049–10067, 1981.

[105] S. R. Spangler and B. B. Plapp. Characteristics of obliquely propagating, nonlinear alfven waves. *Phys. Fluids B*, 4(10):3356–3370, 1992.

[106] P. A. Sweet. The neutral point theory of solar flares. In *IAU Symp. in Electromagnetic Phenomena in Cosmical Physics, ed. B. Lehnet (New York: Cambridge Univ. Press)*, page 123, 1958.

[107] D. W. Swift. On the structure of the magnetic slow switch-off shock. *J. Geophys. Res.*, 88(A7):5685–5691, 1983.

[108] R. A. Treumann. Fundamentals of collisionless shocks for astrophysical application, 1. non-relativistic shocks. *Astron. Astrophys. Rev.*, 17:409–535, 2009.

[109] S. Tsuneta. Structure and dynamics of magnetic reconnection in a solar flare. *Astrophys. J.*, 456:840–849, 1996.

[110] M. Ugai and T. Tsuda. Magnetic field line reconnection by localized enhancement of resistivity, 1, evolution in a compressible MHD fluid. *J. Plasma Phys.*, 17:337, 1977.

[111] D. A. Uzdensity and J. Goodman. Statistical description of magnetized corona above turbulent accretion disk. *Astrophys. J.*, 682:608–629, 2008.

[112] D. W. Walthour, J. T. Gosling, B. U. Ö. Sonnerup, and C. T. Russell. Observation of anomalous slow-mode shock and reconnection layer in the dayside magnetopause. *J. Geophys. Res.*, 99(A12):23705–23722, 1994.

[113] Y. C. Whang. Role of electron physics in slow mode shocks. *Nonlinear Proc. in Geophys.*, 11:259–266, 2004.

[114] Y. C. Whang, D. Fairfield, E. J. Smith, R. P. Lepping, S. Kokubun, and Y. Saito. Observations of double discontinuities in the magnetotail. *Geophys. Res. Lett.*, 24(24):3153–3156, 1997.

[115] Y. C. Whang, J. Zhou, R. P. Lepping, and K. W. Ogilvie. Interplanetary slow shock observed from wind. *Geophys. Res. Lett.*, 23(10):1239–1242, 1996.

[116] D. Winske and N. Omidi. Electromagnetic ion/ion cyclotron instability at slow shocks. *Geophys. Res. Lett.*, 17(12):2297–2300, 1990.

[117] D. Winske and N. Omidi. Electromagnetic ion/ion cyclotron instability: theory and simulations. *J. Geophys. Res.*, 97(A10):14779–14799, 1992.

[118] D. Winske, E. K. Stover, and S. P. Gary. The structure and evolution of slow shocks. *Geophys. Res. Lett.*, 12(5):295–298, 1985.

[119] C. C. Wu. On MHD intermediate shocks. *Geophys. Res. Lett.*, 14(6):668–671, 1987.

[120] C. C. Wu. MKDVB and CKB shock waves. *Space Science Reviews*, 107:403–421, 2003.

[121] C. C. Wu and C. F. Kennel. Evolution of small-amplitude intermediate shocks in a dissipative and dispersive system. *J. Plasma. Phys.*, 47:85–109, 1992.

[122] M. Yamada, F. M. Levinton, N. Pomphrey, R. Budny, J. Manickam, and Y. Nagayama. Investigation of magnetic reconnection during a sawtooth crash in a high-temperature tokmak plasma. *Phys. Plasmas*, 1:3269–3276, 1994.

[123] L. Yin, D. Winske, and W. Daughton. Kinetic Alfvén waves and electron physics. II. Oblique slow shocks. *Phys. Plasmas*, 14, 2007.

[124] L. Yin, D. Winske, W. Daughton, and K. J. Bowers. Kinetic Alfvén waves and electron physics. I. Generation from ion-ion streaming. *Phys. Plasmas*, 14, 2007.

[125] L. Yin, D. Winske, W. Daughton, and F. V. Coroniti. Dissipation in oblique slow shocks. *J. Geophys. Res.*, 110(A09217), 2005.

[126] A. Zeiler, D. Biskamp, J. F. Drake, B. N. Rogers, M. A. Shay, and M. Scholer. Three-dimensional particle simulations of collisionless magnetic reconnection. *J. Geophys. Res.*, 107(A9):1230, 2002.